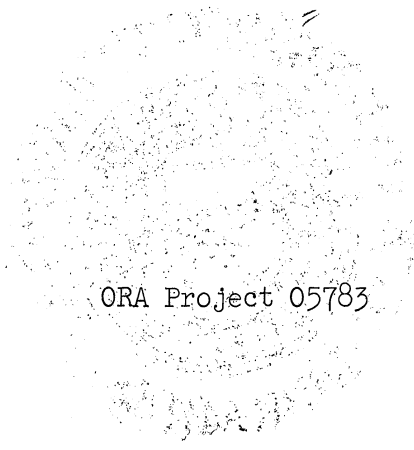


THE UNIVERSITY OF MICHIGAN  
COLLEGE OF ENGINEERING  
Department of Nuclear Engineering

Technical Report

THE EFFECT OF THE PORT VOID IN THE PREDICTION  
OF THERMAL NEUTRON BEAM PORT CURRENT

Sanford C. Cohen



ORA Project 05783

under contract with:

NATIONAL SCIENCE FOUNDATION  
GRANT NO. GP-1032  
WASHINGTON, D.C.

administered through:

OFFICE OF RESEARCH ADMINISTRATION

ANN ARBOR

January 1964

Engle  
UMR  
1295

This report was also a dissertation submitted in partial fulfillment of the requirements for the degree of Doctor of Philosophy in The University of Michigan, 1963.

## ACKNOWLEDGMENTS

I would like to express my appreciation for the numerous helpful discussions with the members of the doctoral committee during the course of the research. In particular, the encouragement and suggestions of Professors John S. King and Paul F. Zweifel are gratefully acknowledged.

The complete cooperation of Mr. J. B. Bullock and the staff of the Ford Nuclear Reactor is appreciated. I am grateful to Mr. Hilding Olson and the staff of the Phoenix Memorial Laboratory for their cooperation. Utilization of The University of Michigan Computing Center and the services of the staff are acknowledged.

A U. S. Atomic Energy Commission special fellowship in nuclear science and engineering provided financial support during most of my years of graduate work. A Phoenix Memorial Project fellowship made possible by the Ford Motor Company helped me to continue my work. For these financial grants I am most grateful.

Finally, the support provided under NSF Grant GP-1032 for the preparation of this manuscript is acknowledged.

## TABLE OF CONTENTS

	Page
LIST OF TABLES	v
LIST OF FIGURES	vi
NOMENCLATURE	x
ABSTRACT	xiii
I. INTRODUCTION	1
A. Statement of the Problem and Motivation for the Study	1
B. Related Published Studies	2
C. Outline of This Study	3
II. ANALYSIS	6
A. Orientation	6
B. Infinite Half-Space Limit	8
C. Diffusion Theory Boundary Condition	13
D. Angular Flux Distribution	16
E. Derivation of $j_B^+$	17
F. Derivation of $j_A^-$	19
G. Scalar Flux Distribution Along the Lateral Surfaces	22
III. EXPERIMENT	28
A. The Ford Nuclear Reactor	28
B. Insertion and Positioning of Ducts	28
C. Normalization	33
D. Detectors	34
E. Counting Equipment	37
F. Unperturbed Flux Distributions for the Water Reflector	38
G. Preliminary Duct Experiments	46
H. Duct Experiments in Water as a Function of Duct Diameter	50
I. Thermal Spectrum	55
J. Measurements in Complete Graphite Reflector	59



TABLE OF CONTENTS (Concluded)

	Page
IV. DISCUSSION	68
A. Unperturbed Thermal Flux Distributions	68
B. 1-1/2-in. Duct Experiments	69
C. Thermal Flux Attenuation Within the Empty Ducts	70
D. Radial Flux Distributions at the Duct Mouth	71
E. Fast Flux Perturbation	72
F. Thermal Spectrum	75
G. Scalar Flux at the Duct Mouth	76
H. Scalar Flux Distribution Along the Duct Walls	79
I. Reactivity Predictions	86
V. CONCLUSIONS	88
APPENDIX	
A. A SURVEY FOR THE ENHANCEMENT OF THERMAL NEUTRON LEAKAGE FLUX	90
1. Introduction	90
2. Three-Dimensional Simulation	91
3. Streaming Flux	94
4. Configurational Effects	95
5. The Effect of Reflector Materials	109
6. Final Remarks	132
7. Subroutine STREAM	135
B. DESCRIPTION OF THE CODES	140
C. COMPOSITIONS AND GROUP CONSTANTS	144
D. COMPARISON OF CURRENT BOUNDARY CONDITION AND PSEUDO BOUNDARY CONDITION AT VACUUM INTERFACE	150
E. DUCT MOUTH CONTRIBUTION TO THE RADIAL CURRENT AT THE WALL	154
F. NORMALIZATION FOR TIME VARYING FLUX	158
G. COMPUTER PROGRAM FOR EVALUATION OF $\frac{\partial \phi / \partial r}{\phi} \Big _{R/z}$	160
REFERENCES	163

## LIST OF TABLES

Table	Page
III.1 Duct Specifications	32
III.2 Normalization Data	35
III.3 Foil Characteristics	36
III.4 Prediction of Activation at Exit of 1-1/2-In. Duct in Water	49
III.5 Neutron Temperature Measurement	58
IV.1 First Estimate of the Radial Component of the Gradients for Boundary Condition in Two-Dimen- sional Calculation	85
IV.2 Duct Reactivity-Measured and Predicted	87
A.I Transverse Bucklings	93
A.II Critical Volume, Area, and Relative Leakage for Bare Reactors of Three Geometries	97
A.III Relative Leakage from a Face for Bare Parallel- epipeds of Various Shapes	100
A.IV Cold-Clean H <sub>2</sub> O Reflected Parallelepiped Cores of Various Shapes	106
A.V Infinite Reflector-Cylindrical Geometry; Various Reflector Materials	116
A.VI Two-Dimensional Calculations; Fixed Sized Core; Inserts of Various Materials	120
A.VII Three and Six Inch Reflectors of Various Materials	129
C.I Compositions	147
C.II Thermal Group Constants	148
C.III Fast Group Constants	149

## LIST OF FIGURES

Figure	Page
2.1 Void configuration.	6
2.2 Infinite half-space geometry.	9
2.3 Normalized angular flux for $c = 1$ ; exact and P-1 approximation.	12
2.4 Linear extrapolation at vacuum interface.	15
2.5 Vector diagram at vacuum interface.	16
2.6 Configuration for calculation of $j_A^-$ .	19
2.7 Current balance geometry.	23
2.8 Current balance geometry including front interface.	26
3.1 Ford Nuclear Reactor core configuration.	29
3.2 Streaming duct, foil holder, and duct support with normalizer.	30
3.3 Photograph of 1-1/2-in. duct encased in 4-in. graphite insert.	31
3.4 Decay of a gold foil counted in the well counter.	39
3.5 Thermal and epicadmium flux out to four feet in water reflector and along axis of 1-1/2-in. duct.	40
3.6 Thermal and epicadmium flux in the core and the water reflector.	42
3.7 East-west traverse of thermal flux in the fuel element bordering on the east of the control rod element.	43
3.8 Unperturbed thermal and epicadmium flux in water reflector.	44
3.9 Reaction rate at exit of 1-1/2-in. duct in water.	47

LIST OF FIGURES (Continued)

Figure		Page
3.10	Thermal reaction rate in 4-in. graphite insert and at the exit of 1-1/2-in. duct encased in 4-in. graphite insert.	48
3.11	Perturbed radial flux distributions at duct mouths.	51
3.12	Perturbed axial flux distributions at duct mouths.	52
3.13	Collimator design.	53
3.14	$j_{B_{th}}^+$ at collimator exit.	54
3.15	Radial variation of flux at 5-in. duct exit.	56
3.16	Thermal flux attenuation within 1-1/2- and 5-in. ducts.	57
3.17	Ratio of reaction rate of $Lu^{176}$ to reaction rate of $1/v$ absorber.	60
3.18	Graphite insert.	61
3.19	Unperturbed thermal and episcadium flux in graphite insert.	64
3.20	Radial flux distribution in graphite insert.	65
3.21	Perturbed thermal flux at center of duct mouths in graphite.	66
3.22	Axial distribution of thermal flux at mouth of 5-in. duct in graphite.	67
4.1	Angular distribution of fast neutrons.	73
4.2	Effect on predicted thermal flux of fast flux depression.	74
4.3	Predicted $j_{B_{th}}^+$ for graphite.	78
4.4	Radial thermal flux behavior at four positions along 5-in. duct wall.	80
4.5	Axial thermal flux distribution along walls of 5-in. duct.	82

LIST OF FIGURES (Continued)

Figure		Page
4.6	Cylindrical geometry approximation to core-duct configuration.	84
A.1	Core geometries for H <sub>2</sub> O reflected configuration studies (cold-clean fuel).	101
A.2	Computed flux distributions; H <sub>2</sub> O reflected core; 3 elements transverse.	102
A.3	Computed flux distributions; H <sub>2</sub> O reflected core; 4 elements transverse.	103
A.4	Computed flux distributions; H <sub>2</sub> O reflected core; 5 elements transverse.	104
A.5	Computed flux distributions; H <sub>2</sub> O reflected core; 7 elements transverse.	105
A.6	Computed flux distributions; comparison of depleted fuel in center and on circumference of core.	108
A.7	Computed flux distributions; infinite H <sub>2</sub> O reflector; cylindrical geometry.	110
A.8	Computed flux distributions; infinite graphite reflector; cylindrical geometry.	111
A.9	Computed flux distributions; infinite BeO reflector; cylindrical geometry.	112
A.10	Computed flux distributions; infinite D <sub>2</sub> O reflector; cylindrical geometry.	113
A.11	Computed flux distributions; 7.5 cm graphite-remainder H <sub>2</sub> O; cylindrical geometry.	114
A.12	Computed flux distributions; 2.5 cm H <sub>2</sub> O-remainder graphite; cylindrical geometry.	115
A.13	Core geometries for material insert studies.	118
A.14	Core geometry for 6 in. BeO reflector.	119

## LIST OF FIGURES (Concluded)

Figure		Page
A.15	Two-dimensional computed flux distributions; H <sub>2</sub> O reflected.	121
A.16	Two-dimensional computed flux distributions; graphite insert.	122
A.17	Two-dimensional computed flux distributions; BeO insert.	123
A.18	Two-dimensional computed flux distributions; D <sub>2</sub> O insert.	124
A.19	Two-dimensional computed flux distributions; 6-in. BeO reflector.	125
A.20	Core geometries for 3- and 6-in. reflectors of various materials.	127
A.21	Core geometries for H <sub>2</sub> O reflected configuration studies (equilibrium Xe-8.4 percent burnup fuel).	128
A.22	$(S^4 - S^3)_{\max}$ for 3- and 6-in. reflection.	130
A.23	$(S^4 - S^1)_{\max}$ for 3- and 6-in. reflection.	131
A.24	Measured and computed flux distributions along axis of cylindrical D <sub>2</sub> O insert.	133
C.1	Wigner-Wilkins and Maxwellian thermal spectra for cold-clean FNR core at 300°K.	146
E.1	Duct configuration for calculation of mouth contribution to wall radial current.	155

## NOMENCLATURE

c	Number of neutrons produced per collision
d	Linear extrapolation distance
h	Duct length
j	Neutron current
k	Multiplication constant
$l$	Neutron mean free path
r	Radial position
$\bar{r}$	Position vector
s	Neutron source
t	Time
v	Neutron velocity
z	Axial position
$z_0$	Extrapolated endpoint
$B^2$	Buckling
D	Neutron diffusion coefficient
E	Neutron energy
L	Neutron diffusion length
R	Duct radius
S	Surface area
T	Neutron temperature
$\mathcal{I}$	Neutron streaming flux
$\alpha$	Largest eigenvalue of diffusion equation

## NOMENCLATURE (Continued)

$\kappa$	Inverse of diffusion length (1/L)
$\lambda$	Radioactive decay constant
$\mu$	Cosine of angle between neutron direction and z axis
$\nu$	Average number of neutrons born per fission
$\xi$	Average logarithmic energy decrement
$\sigma$	Microscopic neutron cross section
$\tau$	Fermi age
$\phi$	Neutron flux
$\chi^i$	Fraction of neutrons born in energy group i
$\Sigma$	Macroscopic neutron cross section
$\bar{\Omega}$	Unit vector denoting direction of travel

### Subscripts

a	Absorption
act	Activation
as	Asymptotic
eff	Effective
epi	Epithermal
f	Fission
g	Geometric
m	Material
o	Scalar
s	Scattering
t	Total



## NOMENCLATURE (Concluded)

th	Thermal
tr	Transport
R	Removal
T	Transverse
TC	Thermal cutoff

### Superscripts

f	Fast
q	Source
th	Thermal
M	Milne
N	Normalized

## ABSTRACT

A method is presented for the prediction of the exit thermal neutron current from a reactor beam port. The results of duct experiments at the Ford Nuclear Reactor afford confidence in the validity of the analytical technique. The motivation for the study is provided by a prevalent desire to enhance thermal neutron beam intensity for spectrometer investigations.

The analysis employs elementary P-1 theory, which is inspired by an examination of the infinite half-space limit. A return current boundary condition at the source plane of the port is developed by summing current contributions from the lateral surfaces. An idealization of the scalar flux distribution along the lateral surfaces of the port permits a diffusion theory solution for the source plane angular flux as a function of the port radius and the unperturbed flux distribution in the medium.

Activation measurements of the scalar flux distributions at the source planes of 1-1/2-, 3-, and 5-in. diameter aluminum ducts were performed in light water and graphite. Measurements of the exit current from the ducts provided with an internal collimator to eliminate wall leakage contributions were carried out in light water. The largest duct perturbation was observed for the 5-in. duct in water. In this case the source plane scalar flux was depressed by 50 percent from the unperturbed flux, and the angular flux in the direction of the duct exit was 61 percent of the unperturbed value. Comparison of the data with analytical results indicates that the exit current is predicted very well. The source plane scalar flux is predicted with somewhat less accuracy.

A background survey for the enhancement of the thermal neutron beam intensity at the Ford Nuclear Reactor is presented in an appendix. Variations in reflector materials and core-reflector configurations were investigated. The results suggest the employment of a D<sub>2</sub>O-reflected core in a slab configuration.

## I. INTRODUCTION

### A. Statement of the Problem and Motivation for the Study

This dissertation develops a method for predicting the exit thermal neutron current from a reactor beam port. The necessary removal of a portion of the diffusing medium to accommodate a beam port exerts a significant influence on the behavior of the thermal neutrons in the vicinity of the port. Inasmuch as these neutrons comprise a source for the beam, the beam port perturbs the intensity and spectrum of the exit beam. Experimental results are presented which test the analytical method under realistic reactor conditions.

The motivation for this study arises from a demand for beam intensity enhancement. An estimate of the influence of the beam port on the exit current intensity is necessary for any thorough enhancement study, although the problem has a great deal of intrinsic interest as well. The increasing importance of neutron spectrometer experiments has revealed the need for the examination of problems associated with neutron beam extraction.<sup>1</sup>

Roughly, the neutron flux,  $\phi(h)$ , at the exit of a beam port of length  $h$  and cross sectional area  $A$  is given by:

$$\phi(h) = \frac{\phi(0) A}{4\pi h^2} \quad , \quad (1.1)$$

where  $\phi(0)$  is the neutron flux at the source plane of the port. The

cross-sectional area of the beam is generally limited by the resolution requirements of the experiment. Thus the intense neutron densities available in the reactor may be attenuated by orders of magnitude at the beam port exit.

#### B. Related Published Studies

Studies for the enhancement of thermal neutron beam intensity have emphasized the reduction of fast neutron and gamma ray background. The split core concept,<sup>2</sup> resulting in the design of the National Bureau of Standards Reactor,<sup>3</sup> involves the removal of fuel from the midplane region of a D<sub>2</sub>O moderated and reflected core. The tangential beam port concept, applied to the Brookhaven High Flux Beam Reactor<sup>4</sup> (HFBR), involves placement of the beam ports tangential to the core. Furthermore, the D<sub>2</sub>O moderated and reflected HFBR is undermoderated so as to produce exceptionally high thermal flux peaking in the reflector.

The effects of duct introduction into a reactor system have been examined primarily from the standpoint of the influence on the multiplication constant of the reactor. Behrens<sup>5</sup> revised the magnitude of  $L^2$ , the diffusion area of a medium containing gas-coolant passages, to account for the additional streaming leakage. Reynolds et al.<sup>6</sup> investigated the reactivity effects of large voids in the reflector of the Pool Critical Assembly at Oak Ridge National Laboratory. In a theoretical examination of the effect on reactivity of a reflector duct Baraff et al.<sup>7</sup>

treated the problem by ordinary perturbation theory. These studies do not yield information concerning the perturbed scalar flux in the vicinity of the void or the current within the void.

Shielding considerations have prompted the examination of the transport of neutrons down long ducts.<sup>8</sup> The influence of the duct walls on the attenuation of neutrons by ducts was studied by Simon and Clifford<sup>9</sup> and they concluded that the direct streaming contribution predominates for  $h/R \gg 1$ . Piercey<sup>10</sup> attempted to separate the contributions to the streaming flux at various distances along the duct axis in measurements at the LIDO reactor. In none of these investigations, however, was consideration given to the duct influence on the streaming source.

### C. Outline of This Study

In Chapter II a simple analytical method is developed to predict the thermal neutron current at the exit of an evacuated duct from a knowledge of the unperturbed scalar flux distribution in the medium. We consider a long radial\* duct introduced into the reactor reflector, presenting a small reactivity perturbation to the multiplying system. The infinite half-space problem is reviewed from the standpoint of the anisotropic limit of the finite void. This permits comparison between exact solutions and the P-1 approximation, and motivates a P-1 approach to the present problem. A pseudo boundary condition on the scalar flux

---

\*A radial duct refers to a duct whose axis lies along a radius of the reactor core.

is developed from the consideration of a finite return current to the duct mouth. Utilization of this boundary condition permits a diffusion theory solution for the perturbed scalar flux distribution at the duct mouth. The diffusion theory solution is used in conjunction with the P-1 angular distribution to predict the exit current. The return current to the mouth is evaluated by summing contributions from the lateral surfaces of the duct. Finally, some consideration is given to the scalar flux distribution along the lateral surfaces of the duct; although the realistic problem is not solved, a reasonable boundary condition is derived from idealizations of the physical situation.

A number of activation experiments were conducted outside of the core of the Ford Nuclear Reactor. These are described in Chapter III. Initial comments concern the reactor, the positioning of ducts, the normalization procedure, and the foil detection techniques. Measurements of the unperturbed scalar flux distributions in the water reflector and reactor core are presented. Preliminary 1-1/2-in. duct experiments in water and a small graphite insert are described. The scalar flux data at the mouth and the collimated exit current for 1-1/2-, 3-, and 5-in. ducts in water are displayed. Data are presented for the attenuation of the thermal flux within the 1-1/2- and 5-in.-ducts. A measurement of the neutron temperature perturbation at the mouth of the 5-in. duct is described. The final section describes the scalar flux measurements at the mouth of the ducts in the graphite reflector. All unperturbed scalar flux measurements are compared with group-diffusion calculations. Scalar

flux data at the duct mouths and exit currents are compared with predictions based upon the analysis presented in Chapter II.

The discussion in Chapter IV considers the assumptions inherent in the analysis. The limitations of diffusion theory for the prediction of the unperturbed scalar flux in the reflector are pointed out, and the seriousness of these limitations from the point of view of the present analysis is considered. An attempt to predict the realistic scalar flux distributions along the duct walls is discussed. Duct reactivity evaluations obtained from two-dimensional group-diffusion calculations based upon initial estimates of the wall gradients are compared with experiment. In addition, items from previous chapters which require further consideration or clarification are discussed in Chapter IV.

A survey directed toward enhancement of the thermal neutron beam intensity at the Ford Nuclear Reactor is presented in Appendix A. The investigation considers variations in reflector materials and core-reflector configurations for radial beam ports. The results are relegated to an appendix because the work was in the nature of a background study preliminary to the main body of this dissertation. In this survey, consequently, the beam port influence on the exit current is neglected. This can be considered a conservative omission from the standpoint of the reflector materials study, since the longer diffusion lengths possessed by the most desirable reflectors give rise to lower beam port current depressions. The method described in Chapter II, however, can be used as a calculational refinement for the configurations of particular interest and a specified beam port diameter.

## II. ANALYSIS

### A. Orientation

The configuration of interest is a long cylindrical void inserted into a diffusing medium. This is sketched in Figure 2.1. Neutrons

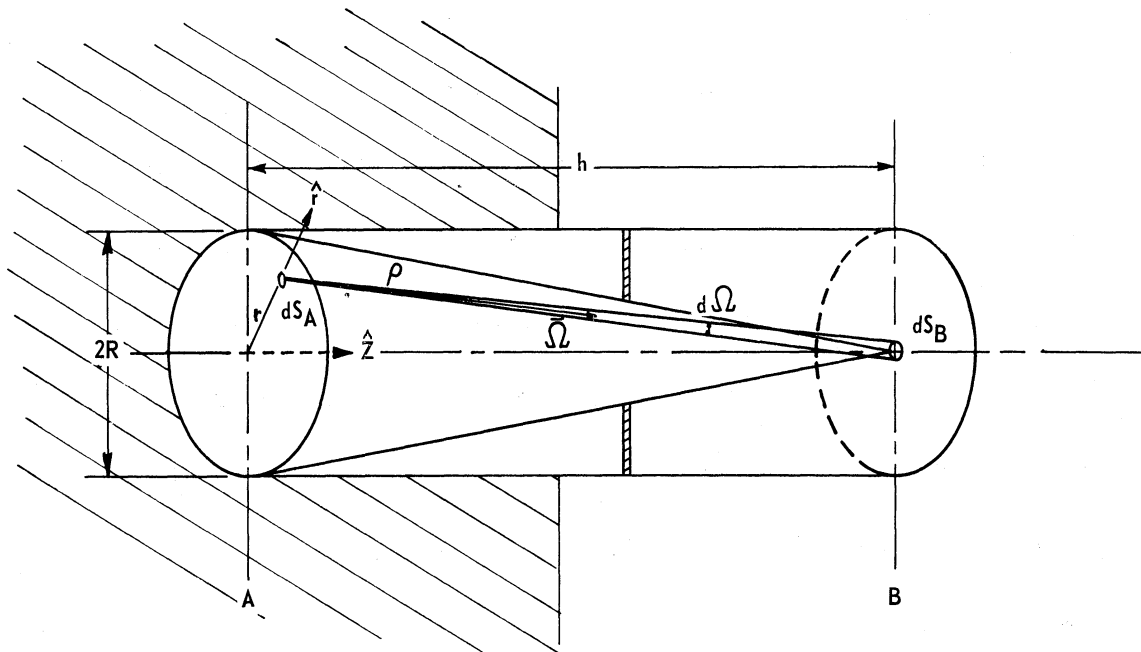


Figure 2.1. Void configuration.

streaming from all points on the interface between the diffusing medium and the void form a beam at B far from interface A.\* Assume that the beam is collimated, so that a detector placed on the axis at B optically views only the front interface at A. We are interested in the number of neutrons

---

\*Henceforth interface A will often be referred to as the mouth of the duct and B as the duct exit.



per unit time passing through a unit area normal to the axis at B. This quantity will be called  $j_B^+(E)$ , the partial current at B.  $j_B^+(E)$  is equivalent to the integral over the surface,  $S_A$ , of the angular current with energy,  $E$ , leaving  $\hat{z} \cdot \bar{\Omega} dS_A$  directed into solid angle  $d\Omega$  about  $\bar{\Omega}$  intercepting  $dS_B$ :

$$j_B^+(E) = \int_{S_A} dS_A \hat{z} \cdot \bar{\Omega} \phi_A(\bar{r}, \bar{\Omega}, E) \frac{d\Omega}{dS_B} . \quad (2.1)$$

Then for any fragment of the energy spectrum:

$$j_B^+(E_0 \rightarrow E_1) = \int_{E_0}^{E_1} dE \int_{S_A} dS_A \hat{z} \cdot \bar{\Omega} \phi_A(\bar{r}, \bar{\Omega}, E) \frac{d\Omega}{dS_B} , \quad (2.2)$$

or the thermal current can be expressed as:

$$j_{Bth}^+ = \int_0^{E_{TC}} dE \int_{S_A} dS_A \hat{z} \cdot \bar{\Omega} \phi_A(\bar{r}, \bar{\Omega}, E) \frac{d\Omega}{dS_B} = \int_{S_A} dS_A \hat{z} \cdot \bar{\Omega} \phi_A^{th}(\bar{r}, \bar{\Omega}) \frac{d\Omega}{dS_B} .$$

The problem then reduces to that of solving for the angular current at interface A. The formulation is initiated by writing the steady state Boltzmann equation for the angular flux,  $\phi(\bar{r}, \bar{\Omega}, E)$ , in space, angle, and energy:

$$\begin{aligned} \bar{\Omega} \cdot \bar{\nabla} \phi(\bar{r}, \bar{\Omega}, E) + \Sigma(\bar{r}, E) \phi(\bar{r}, \bar{\Omega}, E) &= s(\bar{r}, \bar{\Omega}, E) \\ + \int d\Omega' \int dE' \phi(\bar{r}, \bar{\Omega}', E') \Sigma_S(\bar{r}, \bar{\Omega}' \rightarrow \bar{\Omega}, E' \rightarrow E) & . \quad (2.4) \end{aligned}$$

The conventional symbols used in reactor physics are employed, and are defined in the Nomenclature. Hypothetically a solution for the geometry under consideration can be obtained after the source and scattering kernel are specified.

In light of the complexity of the geometry, the pursuit of an exact solution for  $\phi(\bar{r}, \bar{\Omega}, E)$  is nearly futile. A numerical approach, utilizing a high speed digital computer is feasible, but besides lacking in generality, would be prohibitively time-consuming. Rather, we seek a technique which yields the angular flux to a sufficiently high degree of approximation to provide realistic predictions for  $j_{B_{th}}^+$ , and which is simple enough to be useful for practical computations. To this end, P-1 theory is examined.

### B. Infinite Half-Space Limit

In order to assess the validity of a P-1, or diffusion theory, approach consider the case which brings about the highest degree of anisotropy at interface A, that of a full vacuum boundary. Allowing R, the void radius, to go to infinity and considering monoenergetic neutron diffusion in an infinite half-space of fixed composition, exact solutions can be obtained for the steady state transport equation (assuming isotropic scattering):

$$\mu \frac{\partial \phi}{\partial z} + \frac{1}{l} \phi(z, \mu) = s(z, \mu) + \frac{c}{2l} \int_{-1}^1 d\mu' \phi(z, \mu'), \quad (2.5)$$

and comparisons may be drawn with P-1 theory results. Two cases are particularly well known. These are the classical Milne problem,  $s = 0$ , and the case of constant production,  $s = \text{constant}$ .

We shall examine the angular flux in the case of constant production for a unit isotropic source per unit volume. The coordinate frame is sketched in Figure 2.2. Davison<sup>11</sup> expresses the angular flux at the

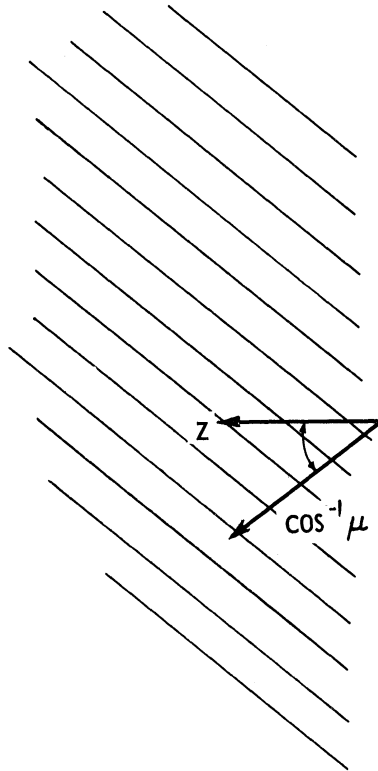


Figure 2.2. Infinite half-space geometry.

boundary in the constant production problem in terms of the Milne solution:

$$\phi^Q(o, \mu) = \frac{L + l\mu}{c |j^M(o)|} \phi^M(o, \mu), \text{ for } \mu < 0 \quad . \quad (2.6)$$

For  $c = 1$  :\*

$$|j^M(0)| = \frac{1}{\sqrt{3}} \phi_0(0) , \quad (2.7)$$

and thus:

$$[\phi^q(0, \mu)]_{c=1} = \frac{\sqrt{3}}{c} (L + l\mu) \left[ \phi^M(0, \mu) \right]^N , \text{ for } \mu < 0. \quad (2.8)$$

where  $[\phi^M(0, \mu)]^N$  is the tabulated<sup>12</sup> Milne angular distribution normalized to unit scalar flux at the boundary.

The P-1 equations for isotropic scattering and a constant isotropic source are:

$$\frac{d}{dz} \phi_1(z) + \Sigma_a \phi_0(z) = s_0 \quad (2.9)$$

$$\frac{1}{3} \frac{d}{dz} \phi_0(z) + \Sigma_t \phi_1(z) = 0 .$$

The angular flux is given by:

$$\phi_{P-1}(z, \mu) = \sum_{n=0}^1 \frac{2n+1}{2} \phi_n(z) P_n(\mu) . \quad (2.10)$$

The solution for the scalar flux is expressed as:

$$\phi_{OP-1}^q(z) = Ce^{-\kappa z} + \frac{s_0}{\Sigma_a} , \quad (2.11)$$

---

\*Our concern with reflector materials indeed directs attention to values of  $c$  close to 1. For light water,  $c = .994$ .

where:

$$\kappa^2 \equiv \frac{3\sum_t \sum_a}{L^2} = \frac{1}{L^2} . \quad (2.12)$$

Applying the Marshak boundary condition:

$$\int_0^1 \mu \phi(0, \mu) d\mu = 0 , \quad (2.13)$$

and setting the source equal to unity, one obtains for the P-1 angular distribution at the boundary:

$$\phi_{P-1}^q(0, \mu) = \frac{2}{\kappa} \frac{\phi_{P-1}^N(0, \mu)}{1 + \frac{2}{3} \frac{\kappa}{\sum_t}} . \quad (2.14)$$

$\phi_{P-1}^N(0, \mu)$  is the familiar form of the normalized P-1 angular distribution, and is given by:

$$\phi_{P-1}^N(0, \mu) = \frac{1}{2} - \frac{3}{4} \mu . \quad (2.15)$$

The normalized P-1 and Milne angular distributions are compared in Figure 2.3.

A comparison of the scalar fluxes is obtained by integrating Eqs. (2.8) and (2.14) over all angles, yielding:

$$\left[ \frac{\phi_{cP-1}^q(0)}{\phi_0^q(0)} \right]_{c=1} = 1.155 . \quad (2.16)$$

The quantity of particular interest for the beam port problem is the

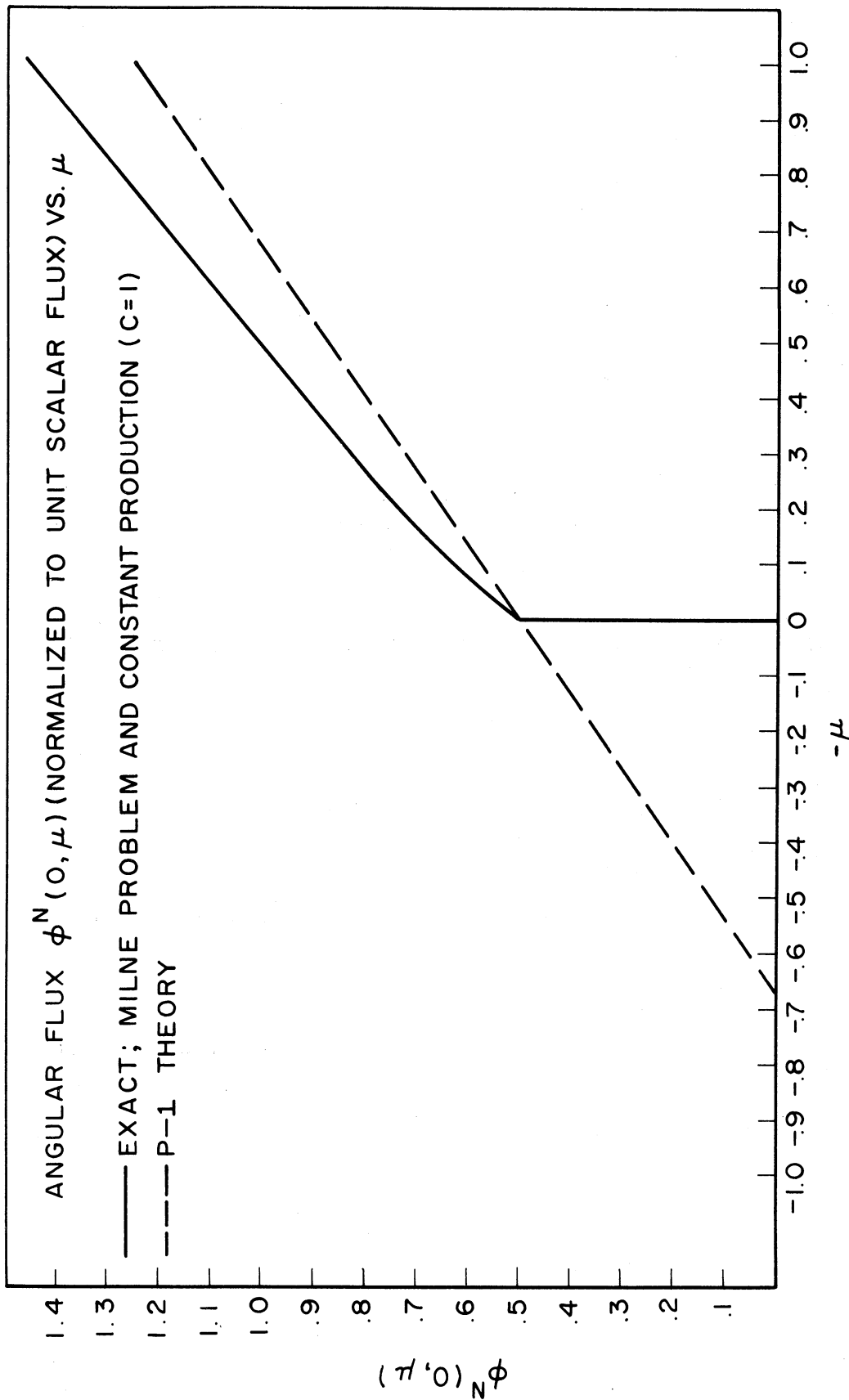


Figure 2.3. Normalized angular flux for  $c = 1$ ; exact and P-1 approximation.

angular flux close to  $\mu = -1$ . Setting  $\mu = -1$  in Eqs. (2.8) and (2.14) we obtain:

$$\left[ \frac{\phi_{P-1}^q(0, \mu)}{\phi^q(0, \mu)} \right]_{\substack{c=1 \\ \mu=-1}} = .993 \quad . \quad (2.17)$$

The same result is obtained for the Milne problem ( $s = 0$ ) if both the P-1 solution and the exact solution are normalized to the exact value of the scalar flux at the boundary. Thus the P-1 approach gives rise to an angular flux for very small angles which differs by less than 1 percent from the exact solution. It should be pointed out that the P-1 solution is free of transport corrections.

### C. Diffusion Theory Boundary Condition

Since a P-1 approach provides an excellent approximation for the angular flux in the limiting case of the infinite half-space, we shall examine the finite void using diffusion theory. The current returning to the mouth of the void originates from neutrons leaving the lateral surfaces. This forms a basis for a boundary condition at A which is physically realistic and consistent with the general formulation of diffusion theory.

In addition to the assumption of low capture in the medium,  $c \approx 1$ , and small angles to the detector,  $(R/h)^2 \ll 1$ , the following two assumptions

are made:

1. The perturbed scalar flux is flat over the entire duct mouth.

This permits us to neglect the radial dependence at the mouth.

2. The fast flux is unperturbed by the void. As a corollary to this the assumption is made that the overall reactor fission source perturbation is negligible.

Specification of the partial current at A coupled with the continuity requirements at the boundary between the multiplying medium and the reflector completely specifies the diffusion theory solution for the scalar flux in the medium. It is convenient, however, to transform the current condition into one on the scalar flux,  $\phi_0$ . Proceeding analogously to the familiar treatment of the limiting full vacuum interface<sup>13</sup> and referring to Figure 2.4:

$$j_A^- = \frac{\phi_0^A}{4} + \frac{k_{tr}}{6} \left. \frac{d\phi_0}{dz} \right|_A \quad (2.18)$$

Assuming a linear decay of the scalar flux past A:

$$\phi_0(z) = z \left. \frac{d\phi_0}{dz} \right|_A + \phi_0^A, \quad (2.19)$$

we solve for the distance,  $d$ , past the interface, at which  $\phi_0(d) = 4 j_A^-$ :

$$4 j_A^- = d \left. \frac{d\phi_0}{dz} \right|_A + \phi_0^A \quad (2.20)$$



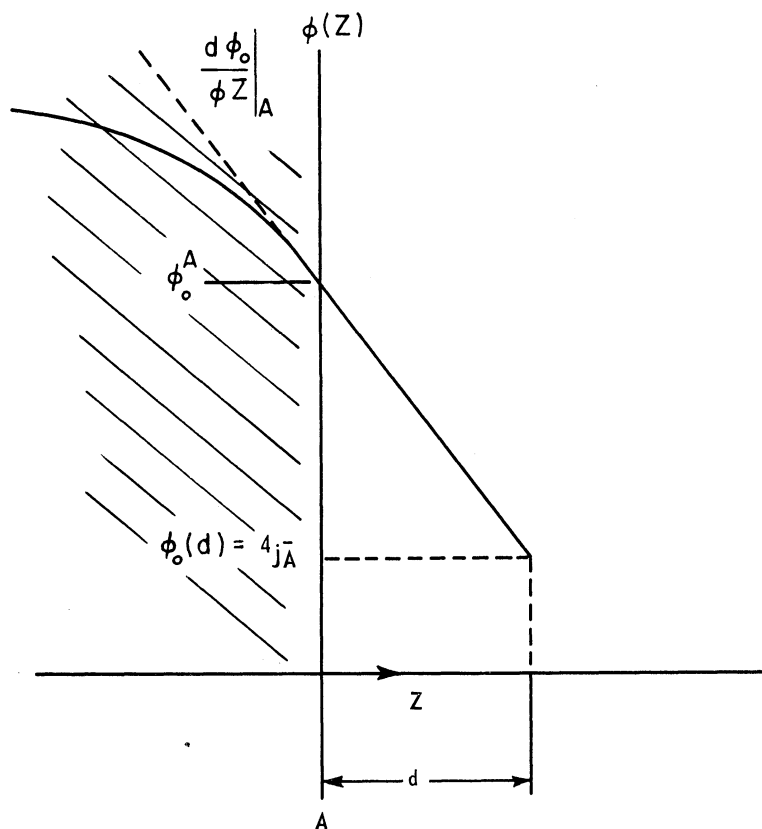


Figure 2.4. Linear extrapolation at vacuum interface.

Combining Eqs. (2.18) and (2.20) we obtain:

$$\phi_0\left(\frac{2}{3} l_{tr}\right) = 4 j_A^- , \quad (2.21)$$

the well-known diffusion theory extrapolation condition, applied here to a vacuum boundary possessing a finite return current.

It is shown in Appendix D that the application of this pseudo boundary condition on the scalar flux rather than the actual one involving the partial current introduces negligible error for  $c \approx 1$ . Furthermore, the employment of a linear extrapolation distance,  $d$ , rather than the extrapolated endpoint,  $z_0$ , is valid for values of  $c$  close to one:<sup>11</sup>

$$\frac{d}{z_0} \approx c^{-1/2} \quad \text{for } c \approx 1 \quad . \quad (2.22)$$

#### D. Angular Flux Distribution

The P-1 approximation to the angular flux is needed to calculate duct currents. It is instructive to derive it directly from the integral form of the transport equation. In the constant cross section approximation the angular flux is given by (Eq.(4-16) of Reference 11):

$$\phi(\bar{r}, \bar{\Omega}) = \int_0^\infty \left[ \left( \frac{c}{4\pi\ell} \right) \phi_0(\bar{r}-\eta\bar{\Omega}) + s(\bar{r}-\eta\bar{\Omega}) \right] e^{-\eta/\ell} d\eta. \quad (2.23)$$

Figure 2.5 is a vector diagram pertinent to Eq. (2.23). The source term in the equation is defined per unit solid angle.

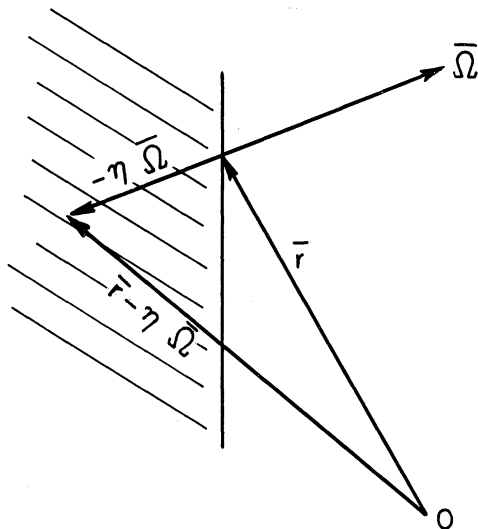


Figure 2.5. Vector diagram at vacuum interface.

Expanding any function,  $f(\bar{r}-\eta\bar{\Omega})$ , about the point  $\bar{r}$  in a Taylor series

gives:

$$f(\bar{r}-\eta\bar{\Omega}) = f(\bar{r}) + (-\eta\bar{\Omega}\cdot\bar{\nabla})f(\bar{r}) + \frac{1}{2!}(-\eta\bar{\Omega}\cdot\bar{\nabla})^2 f(\bar{r}) + \dots \quad (2.24)$$

Accordingly expanding the scalar flux and source in the integral equation, performing the integration over  $\eta$ , and retaining two terms yields:

$$\phi(\bar{r},\bar{\Omega}) \simeq \frac{c}{4\pi}[\phi_0(\bar{r}) - \ell\bar{\Omega}\cdot\bar{\nabla}\phi_0(\bar{r})] + \ell[s(\bar{r}) - \ell\bar{\Omega}\cdot\bar{\nabla}s(\bar{r})] \quad (2.25)$$

#### E. Derivation of $j_B^+$

Using the angular distribution presented in Eq. (2.25) and diffusion theory solutions for the source and scalar flux distributions at the mouth, we are in a position to derive an expression for  $j_B^+$ , the partial current at the exit of a long collimated duct. Restricting ourselves to the geometry illustrated in Figure 2.1, and assuming polar symmetry:

$$\bar{\nabla} = \hat{r} \frac{\partial}{\partial r} + \hat{z} \frac{\partial}{\partial z} \quad , \quad (2.26)$$

$$\bar{\Omega} = \hat{r} \left( -\frac{r}{\rho} \right) + \hat{z} \left( \frac{h}{\rho} \right) \quad , \quad (2.27)$$

and:

$$d\Omega = \frac{dS_B(h)}{\rho^2} \quad . \quad (2.28)$$

The angular flux at A in the direction of a detector on the axis at B is expressed as:

$$\begin{aligned} \phi_A(\bar{r}, \bar{\Omega}) \approx & \frac{c}{4\pi} \left\{ \phi_0(\bar{r}) - l \left[ \frac{h}{\rho} \frac{\partial \phi_0}{\partial z} \Big|_{\bar{r}} - \frac{r}{\rho} \frac{\partial \phi_0}{\partial r} \Big|_{\bar{r}} \right] \right\}_A \\ & + l \left\{ s(\bar{r}) - l \left[ \frac{h}{\rho} \frac{\partial s}{\partial z} \Big|_{\bar{r}} - \frac{r}{\rho} \frac{\partial s}{\partial r} \Big|_{\bar{r}} \right] \right\}_A . \end{aligned} \quad (2.29)$$

Assume that  $\phi_0$ ,  $s$ , and their derivatives are constant over the emitting surface, so that:

$$\phi_A(r, \bar{\Omega}) \approx \frac{c}{4\pi} \left[ \phi_0 - l \frac{h}{\rho} \frac{d\phi_0}{dz} \right]_A + l \left[ s - l \frac{h}{\rho} \frac{ds}{dz} \right]_A . \quad (2.30)$$

Substituting this expression for the angular flux into Eq. (2.3) and integrating over the surface at A results in:

$$\begin{aligned} j_B^+ \approx & \frac{c}{4} \left\{ \left( \frac{R^2}{h^2 + R^2} \right) \phi_0 - \frac{2}{3} l \left[ 1 - \left( 1 + \frac{R^2}{h^2} \right)^{-3/2} \right] \frac{d\phi_0}{dz} \right\}_A \\ & + \pi l \left\{ \left( \frac{R^2}{h^2 + R^2} \right) s - \frac{2}{3} l \left[ 1 - \left( 1 + \frac{R^2}{h^2} \right)^{-3/2} \right] \frac{ds}{dz} \right\}_A . \end{aligned} \quad (2.31)$$

For a long duct,  $R^2/h^2 \ll 1$ , so that the expression reduces to:

$$j_B^+ \approx \frac{R^2}{h^2} \left\{ \frac{c}{4} \left[ \phi_0 - l \frac{d\phi_0}{dz} \right] + \pi l \left[ s - l \frac{ds}{dz} \right] \right\}_A . \quad (2.32)$$

The slowing-down source can be computed from the fast flux obtained in a few-group analysis. Assuming fast flux isotropy:

$$s = \frac{\sum_R \phi_0}{4\pi} \cdot$$

#### F. Derivation of $\bar{j}_A$

Equation (2.21) specifies the diffusion theory boundary condition to be used in obtaining the distribution of the perturbed scalar flux in the vicinity of the duct mouth. It is necessary to sum contributions from all lateral surfaces of the duct in order to derive an expression for  $\bar{j}_A$  in terms of the scalar flux distribution along the walls of the duct. The geometry is illustrated in Figure 2.6.

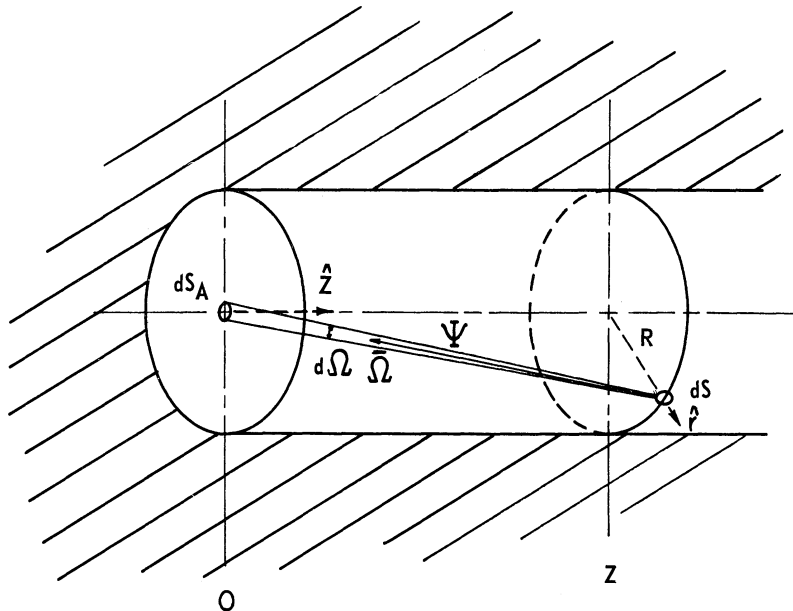


Figure 2.6. Configuration for calculation of  $\bar{j}_A$ .

Equation (2.25) is employed once again for the angular flux along the lateral surfaces of the duct. Assuming that the slowing-down source contribution is negligible, and that  $c \approx 1$ :

$$\phi(z, R, \bar{\Omega}) \cong \frac{1}{4\pi} \left[ \phi_0(z, R) - \ell \bar{\Omega} \cdot \bar{\nabla} \phi_0 \Big|_{\substack{z \\ R}} \right] . \quad (2.34)$$

Since the mouth is treated in one dimension, it will suffice to solve for the return current at the center. Referring to Figure 2.6:

$$\bar{\Omega} = -\hat{r} \frac{R}{\psi} - \hat{z} \frac{z}{\psi} , \quad (2.35)$$

$$d\Omega = \frac{dS_A}{\psi^2} \frac{z}{\psi} , \quad (2.36)$$

$$\psi^2 = R^2 + z^2 , \quad (2.37)$$

and:

$$dS = 2\pi R dz . \quad (2.38)$$

The return current at the mouth is expressed as:

$$j_A^- = \int_S dS (-\hat{r} \cdot \bar{\Omega}) \phi(z, R, \bar{\Omega}) \frac{d\Omega}{dS_A} . \quad (2.39)$$

Substituting the angular flux:

$$\phi(z, R, \bar{\Omega}) \cong \frac{1}{4\pi} \left\{ \phi_0(z, R) + \ell \left[ \frac{R}{\psi} \frac{\partial \phi_0}{\partial r} \Big|_{\substack{R \\ z}} + \frac{z}{\psi} \frac{\partial \phi_0}{\partial z} \Big|_{\substack{R \\ z}} \right] \right\} , \quad (2.40)$$

into Eq. (2.39), and supposing that the void extends to infinity, we obtain for the return current at the mouth:

$$j_A^- = \frac{R^2}{2} \left\{ \int_0^\infty dz \frac{z \phi_0(R, z)}{(R^2+z^2)^2} + l \int_0^\infty dz \frac{z^2 \frac{\partial \phi_0}{\partial z} \Big|_R}{(R^2+z^2)^{5/2}} + l R \int_0^\infty dz \frac{z \frac{\partial \phi_0}{\partial r} \Big|_R}{(R^2+z^2)^{5/2}} \right\}. \quad (2.41)$$

In order to assess the validity of this expression, let us examine the limits as  $R \rightarrow 0$  and  $R \rightarrow \infty$ . It is first convenient to transform variables such that:

$$j_A^- = \frac{1}{2} \left\{ \int_0^\infty dz \frac{z \phi_0(R, Rz)}{(1+z^2)^2} + l \int_0^\infty dz \frac{z^2 \frac{\partial \phi_0}{\partial z} \Big|_R}{(1+z^2)^{5/2}} + l \int_0^\infty dz \frac{z \frac{\partial \phi_0}{\partial r} \Big|_R}{(1+z^2)^{5/2}} \right\}. \quad (2.42)$$

When  $R$  becomes small, the scalar flux and its derivatives are slowly varying with respect to the remainder of the integrand, and can be taken outside the integral sign. The integrations yield:

$$\lim_{R \rightarrow 0} j_A^- = \frac{\phi_0(0,0)}{4} + \frac{l}{6} \frac{1}{z \cdot \nabla} \phi_0 \Big|_0, \quad (2.43)$$

which is the partial current at  $A$  in the absence of the void.

In the limit of large  $R$  the rest of the integrands are slowly varying with respect to  $\phi_0$  and its derivatives, and accordingly:\*

---

\*We assume here that the scalar flux is monotonically decreasing with  $z$ ; the unperturbed flux is of the form:  $\phi(Rz) = \sum_i C_i e^{-a_i Rz}$ .

$$\lim_{R \rightarrow \infty} \bar{j}_A = 0, \quad (2.44)$$

the vacuum interface condition. Equation (2.41), then, has the desired limits.

#### G. Scalar Flux Distribution Along the Lateral Surfaces

The final task, and evidently the most formidable, is the evaluation of the scalar flux distribution along the lateral surfaces of the void. We expect the average perturbation of the angular flux along the duct walls contributing most heavily to the return current to be less than that at mouth. This is because of the considerably more favorable view factors along the walls. For small void diameters it is reasonable to assume that the angular flux along the walls is unperturbed.

A sound approach to the problem, however, consists of a current balance over all surfaces. Such a procedure has been carried out for a void of finite length along the axis of a cylindrical reactor.<sup>14</sup> Considering for the moment a long cylindrical void, the radial component of the gradient at a point  $(R, z_1)$  on the surface is obtained by equating the outgoing (in the positive radial direction) partial current to the contributions from all surfaces of the void. The angular distribution is given by Eq. (2.34). Figure 2.7 illustrates the geometry. Carrying out



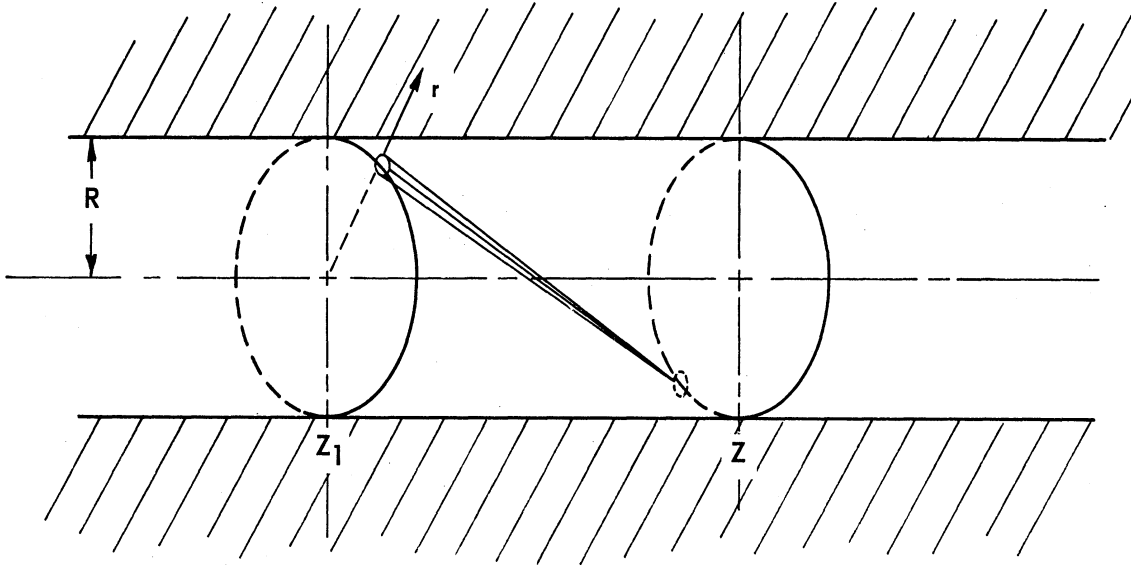


Figure 2.7. Current balance geometry.

the angular integrations and solving for the radial component of the gradient, one obtains:

$$\begin{aligned}
 - \ell \frac{\partial \phi_0 / \partial r \Big|_{z_1}^R}{\phi_0(R, z_1)} &= - \frac{3}{2} + \frac{3}{2\pi R} \left\{ \int dz \frac{\phi_0(R, z)}{\phi_0(R, z_1)} f_1(p) + \ell \int dz \frac{\partial \phi_0 / \partial r \Big|_z^R}{\phi_0(R, z_1)} f_2(p) \right. \\
 &\quad \left. - \ell \int dz \frac{\partial \phi_0 / \partial z \Big|_z^R}{\phi_0(R, z_1)} f_3(p) \right\}, \quad (2.45)
 \end{aligned}$$

where:

$$f_1(p) = \frac{\pi}{4} \left[ 2 - (2+p^2)(1-p^2)^{1/2} \right], \quad (2.46)$$

$$f_2(p) = \frac{1}{3p} \left[ (2(1-p^4) + 3(2-p^2))E(p^2) - (1-p^2)(8+p^2)K(p^2) \right], \quad (2.47)$$

$$f_3(p) = \frac{1}{3} \left[ \pm(1-p^2)^{1/2} \right] \left[ (2+p^2)K(p^2) - 2(1+p^2)E(p^2) \right], \quad (2.48)$$

$$p^2 \equiv \frac{1}{1 + \frac{(z_1 - z)^2}{4R^2}} \quad ; \quad \pm(1-p^2)^{1/2} \equiv \frac{z_1 - z}{\left[ (z_1 - z)^2 + 4R^2 \right]^{1/2}} \quad , (2.49)$$

and K and E are the complete elliptic integrals of the first and second kinds.<sup>15</sup>

The integral equation is not easily soluble. Zimmerman assumed a separable solution, in which case Eq. (2.45) reduces to:

$$l \frac{\partial \phi_0 / \partial r \Big|_{z_1}^R}{\phi_0(R, z_1)} = \frac{1 - \frac{1}{\pi R} \int dz \frac{\phi_0(z)}{\phi_0(z_1)} f_1(p) + \frac{l}{\pi R} \int dz \frac{\partial \phi_0 / \partial z}{\phi_0(z_1)} f_3(p)}{\frac{2}{3} \left\{ 1 + \frac{3}{2\pi R} \int dz \frac{\phi_0(z)}{\phi_0(z_1)} f_2(p) \right\}} \quad . \quad (2.50)$$

The assertion was made that although the separable approach lacks in rigor, it possesses the correct limits (for the void along the axis of a cylindrical reactor).

The trivial case of the infinite cylinder with a constant flux along the walls, although not directly applicable to our problem, is instructive and does permit a separable solution. For this case  $\phi_0(z)/\phi_0(z_1) = 1$ , and  $\partial \phi_0 / \partial z = 0$ , and the integrations are performed from  $-\infty$  to  $\infty$ .

The numerator in Eq. (2.50) vanishes, and we obtain:

$$l \frac{\partial \phi_0 / \partial r \Big|_{z_1}^R}{\phi_0(R, z_1)} = 0 \quad , \quad (2.51)$$

for all  $z_1$ .

In the spirit of the Zimmerman approach, a linear decaying flux of

the form  $\phi_0(z) = a+bz$  also leads to a zero gradient condition for the infinitely long cylinder. This can be shown by examining the point  $z_1 = 0$ . For this case  $\phi_0(z)/\phi_0(z_1) = 1+cz$  and  $\frac{\partial\phi_0/\partial z}{\phi_0(z_1)} = c$ , and the numerator of the right-hand side of Eq. (2.50) becomes:

$$1 - \frac{1}{\pi R} \int_{-\infty}^{\infty} dz(1+cz)f_1(p) + \frac{l}{\pi R} \int_{-\infty}^{\infty} dz c f_3(p) . \quad (2.52)$$

The terms multiplied by the constant are odd functions, and their integrals are zero. The remaining terms are identical to the constant flux case, giving:

$$l \frac{\partial\phi_0/\partial r|_0^R}{\phi(R,0)} = 0 . \quad (2.53)$$

This example, however, is somewhat of a mathematical artifice, in that the result is not the same for  $z_1 \neq 0$ ; and so the assumption of separability is not strictly valid (moreover, the linear expression permits negative fluxes).

The actual void geometry consists of a semi-infinite cylinder bounded by an interface at  $z = 0$  (See Figure 2.8). The current balance at any point  $z_1 > 0$  now contains additional terms from the contribution of the mouth. The isotropic and  $z$  component of the gradient contributions are derived in Appendix E and are of the form:

$$\frac{3}{2} \frac{\phi_0(0)}{\phi_0(z_1)} \left[ \frac{\frac{1}{2} + \frac{z_1^2}{4R^2}}{\left(1 + \frac{z_1^2}{4R^2}\right)^{1/2}} - \frac{z_1}{2R} \right] - \frac{6}{\pi} l z_1^2 \frac{\partial\phi_0/\partial z|_0}{\phi_0(z_1)} \int_0^R r dr I_2(r,R,z_1) . \quad (2.54)$$

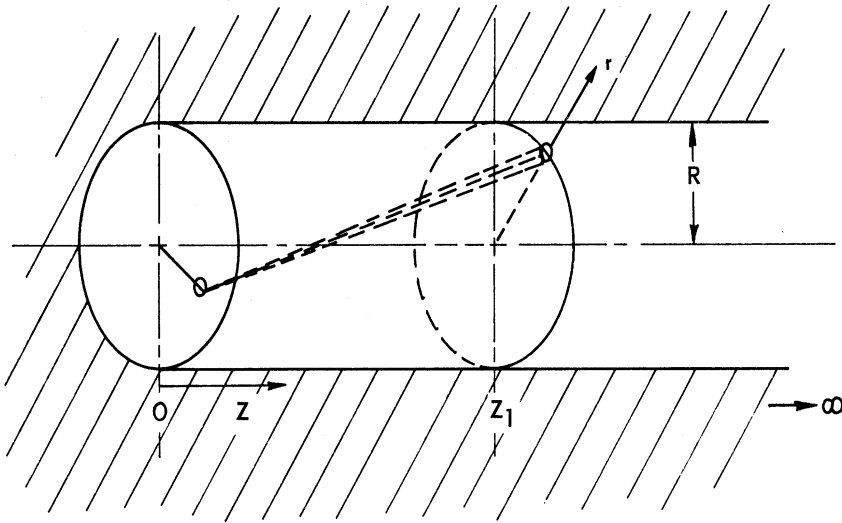


Figure 2.8. Current balance geometry including front interface.

These additional terms must be added to the right-hand side of Eq. (2.45).

Postulating as before a constant flux everywhere along the boundaries such that  $\partial\phi_0/\partial z|_0 = 0$  and  $\frac{\phi_0(0)}{\phi_0(z_1)} = 1$ , and assuming separability, one finds that the contribution from the mouth is equivalent to that from the negative half of the infinite cylinder studied previously. This leads once again to the condition:

$$\left. \frac{\partial\phi_0/\partial r}{\phi_0} \right|_{z_1}^R = 0, \quad \text{for all } z_1 > 0 \quad . \quad (2.55)$$

We have not solved the physically interesting problem, however. In fact the argument for the  $R \rightarrow 0$  limit of Eq. (2.41) demonstrates that a constant flux along the lateral surfaces does not give rise to a duct perturbation at the mouth at all. The realistic unperturbed scalar flux is likely to be a decaying exponential or sum of exponentials, in which

case a  $z$  dependent radial component of the gradient is expected along the duct walls. Positive near the mouth, the radial component of the gradient becomes negative at an axial distance from the mouth such that the streaming contributions exceed the unperturbed flux in the medium.

In light of the complexity of the actual physical situation, the pursuit of an accurate representation of the scalar flux distribution at the duct walls will be avoided. Instead we assume that the zero gradient boundary condition is a reasonable approximation. This is equivalent to direct utilization of the unperturbed scalar flux if the unperturbed flux distribution is radially flat in the vicinity of the duct. The validity of this zero order perturbation treatment will be assessed by its success in predicting the results of experiment.

### III. EXPERIMENT

#### A. The Ford Nuclear Reactor

The experiments were conducted on the south face of the Ford Nuclear Reactor. The FNR is a swimming pool facility similar in design to the Bulk Shielding Reactor at Oak Ridge National Laboratory.<sup>16</sup> The fuel is of the MTR type. Regular elements contain 140 grams of  $U^{235}$  in 18 plate 3 in. x 3 in. subassemblies. Partial elements, which house the poison rods, contain 71 grams of  $U^{235}$  in 9 plate subassemblies. A more complete description of the facility is contained in the literature.<sup>17</sup>

The core configuration adopted for the experiments is illustrated in Figure 3.1. Occasional minor variations in the fuel loading were necessitated by criticality considerations, but changes were confined to the north extremities of the core. The specific elements on the south face were left unchanged during the period of experiments.

#### B. Insertion and Positioning of Ducts

A duct, the duct support, and a foil holder are sketched in Figure 3.2. Variable sized collars mounted on the aluminum plate of the support accommodate the ducts for positioning. The weighted plug bolted to the bottom of the plate fits into a south matrix hole of the grid plate which is furnished with an offset dowel pin to guarantee angular placement.

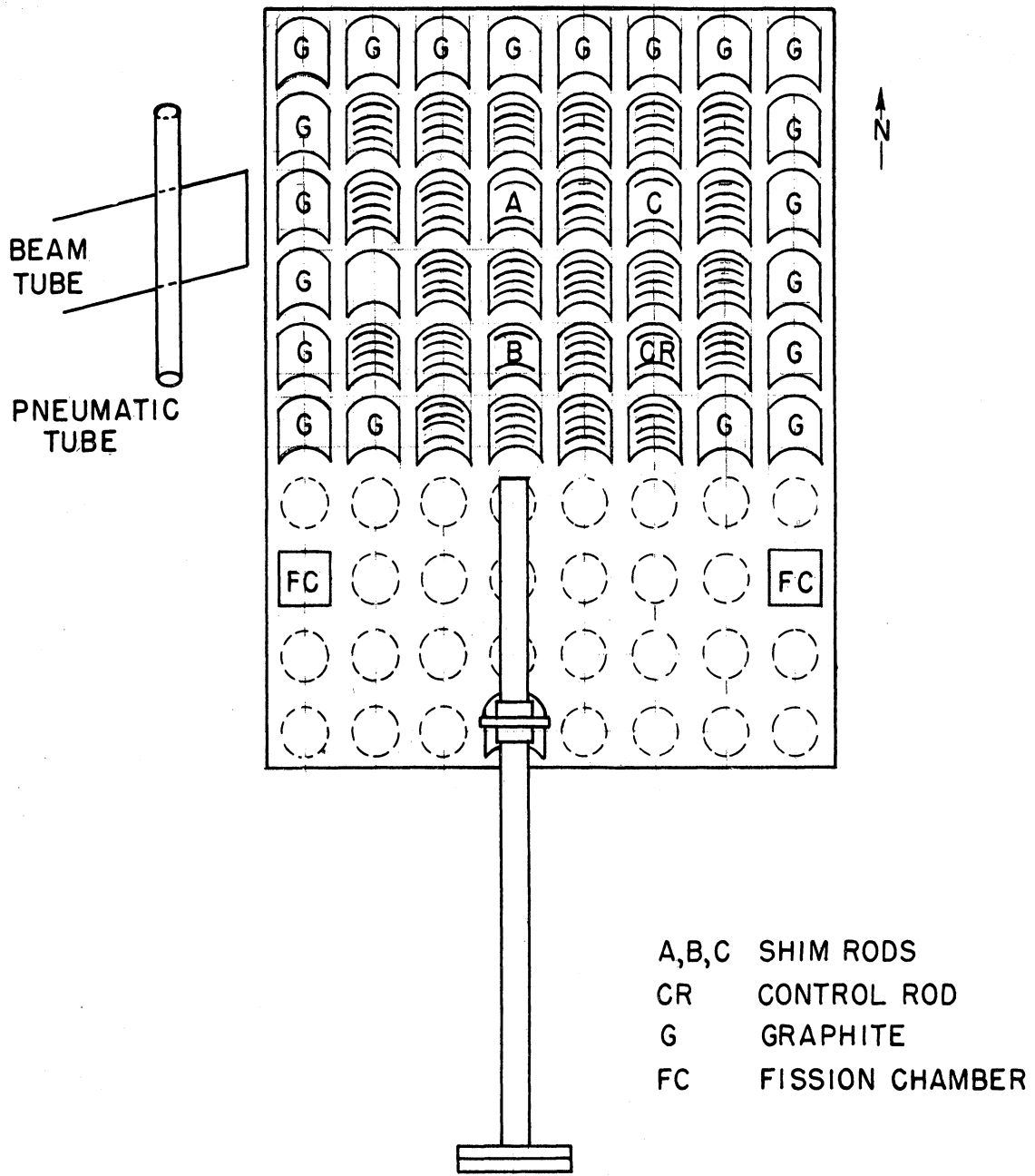


Figure 3.1. Ford Nuclear Reactor core configuration.

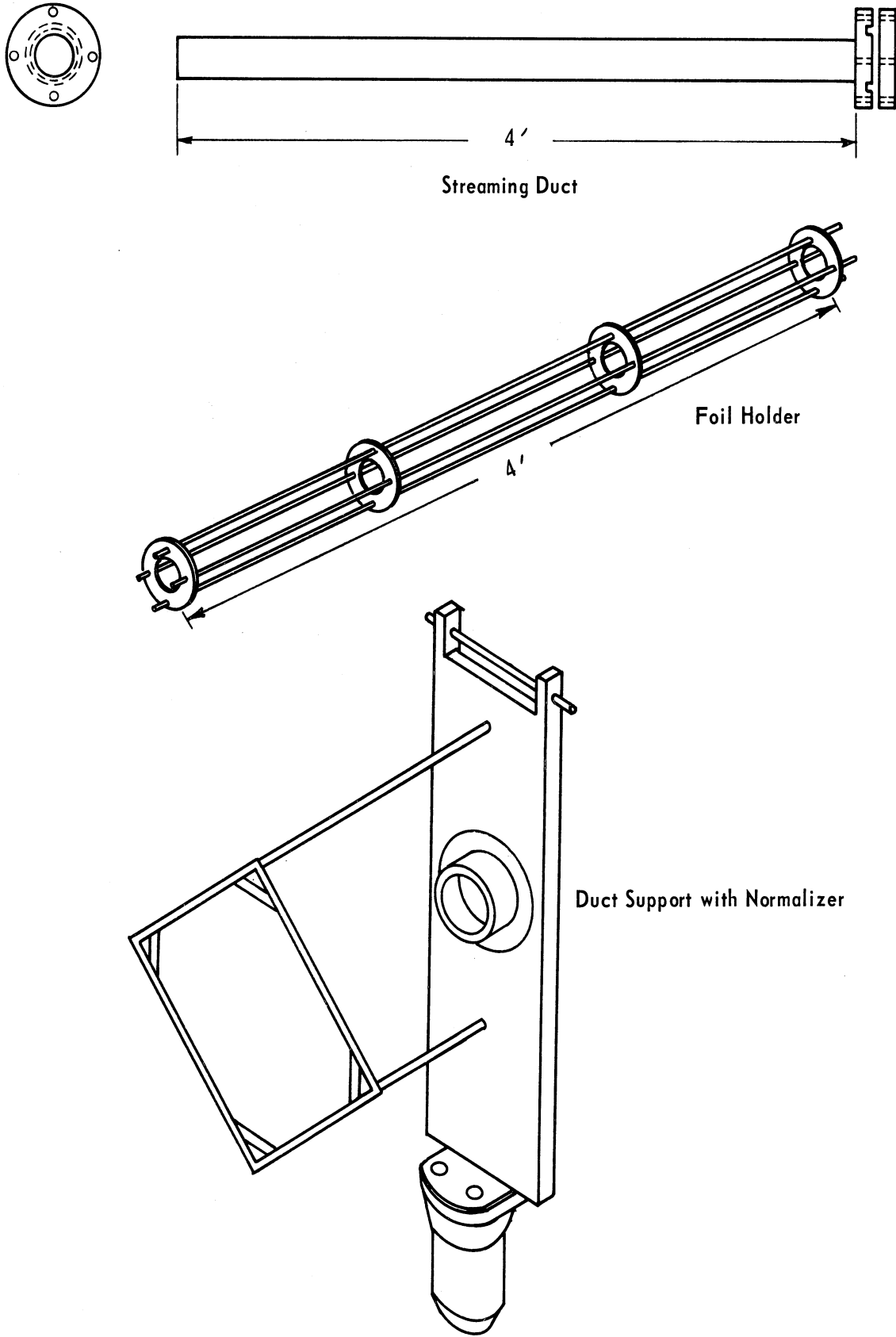


Figure 3.2. Streaming duct, foil holder, and duct support with normalizer.



Figure 3.3 is a photograph of the 1-1/2-in. duct encased within the 4-in. graphite insert positioned adjacent to the core.

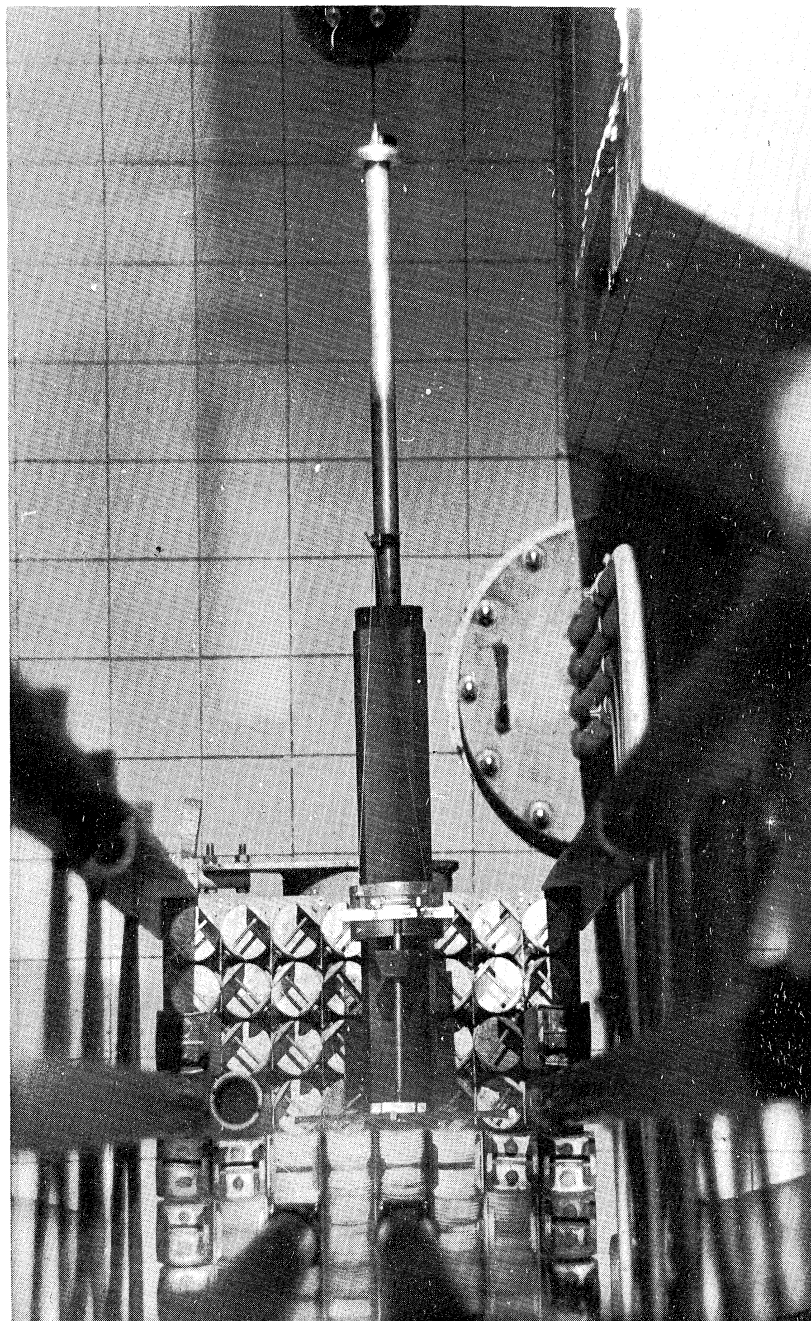


Figure 3.3. Photograph of 1-1/2-in. duct encased in 4-in. graphite insert.

Table III.1 is a list of the dimensions of the three aluminum ducts employed in the water runs. Also tabulated are the reactivity worths of the ducts positioned 4 in. below the centerline of the core in the column pictured in Figure 3.1. The ducts were evacuated to eliminate attenuation of neutrons by air and water vapor.

TABLE III.1

## DUCT SPECIFICATIONS

O.D., in.	Wall Thick- ness, in.	Front Window Thick- ness, in.	Length, ft	Reactivity $\delta k/k$ Axial Distance from Core		
				.76 cm	2.16 cm	6.16 cm
1-1/2	.0625	.020	4	...	.007%	...
3	.083	.040	4	...	.03%	...
5	.187	.062	4	.14%	.10%	<.01%

Runs were made at various low power levels in the range of 500 watts to 70 kilowatts. The duration of each run was chosen so that duct insertion and withdrawal occupied a time interval of less than 1-1/2 percent of the total irradiation. Spacing of runs was limited by the induced activity of the metal, which would have decayed in less than one-half hour had the material been pure aluminum. The presence of alloying con-

stituents in the aluminum extended the cooling time considerably for high power activations.

### C. Normalization

Because the experiments were performed at variable reactor power on different days, it was necessary to employ a precise and reliable procedure to normalize the runs to one another. First attempts at normalization using the pneumatic tubes on the west face of the core proved unsatisfactory. Although the activations in the pneumatic system agreed within  $\pm 2$  percent with a fixed monitor viewing the west face at the exit of a beam port, the proportionality between the flux intensity on the west face and at the duct position was destroyed by rod manipulations, xenon buildup, and core movements.

Normalization was finally accomplished with the aid of the pinwheel frame shown in Figure 3.2. Foils were mounted at the four corners of the diamond which were each  $6\frac{1}{2}$  in. from the duct axis and  $\frac{1}{2}$  in. from the reactor core. That the duct itself exerted no influence on the normalizing foils was verified by comparing the normalization of consecutive 5 in. void and no-void runs with the fission chambers positioned as in Figure 3.1. The influence of poison rods was minimized by holding B shim rod 100 percent withdrawn and the control rod greater than 40 percent withdrawn during an irradiation. Furthermore, the duct axis was positioned 4 in. below the core midplane. That the spectrum was not changing

significantly for the purpose of normalization was confirmed by irradiating two cadmium-covered foils simultaneously with the bare normalizing foils. Typical normalization data are displayed in Table III.2. Comparison of the root-mean-square deviation between the four positions set a normalization error upper limit of approximately  $\pm 3$  percent. Repeated runs were reproducible within these limits.

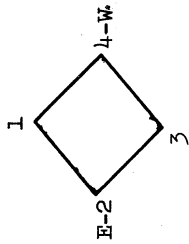
#### D. Detectors

Metallic foil activators were used for all of the measurements. Gold, copper, manganese, and lutetium were each utilized to some extent. Table III.3 is a list of the pertinent foil characteristics.

Gold was used for most of the measurements. It could be obtained chemically pure and possesses a high activation cross section together with a long half-life. In addition, the large 4.9 ev resonance cross section permits epithermal activations at a well-defined energy. Bare and cadmium-covered  $1/16$  in. x  $1/16$  in. x .001 in. foils were employed at the duct mouth with no significant perturbation induced in larger foils irradiated at the exit of the duct. The small foils at the mouth could be counted in a well counter soon after irradiation at the flux levels necessary to activate the foils at the exit. Weighing was accomplished on an electrostatic balance.

Epithermal fluxes were measured by completely surrounding the foils with 20 mils of cadmium. Incomplete cadmium enclosure was shown to lead

TABLE III.2  
NORMALIZATION DATA



Run No.	Date	Duct Size, in.	Control Rod Position, %	Nominal Reactor Power Level*, kw	Mon. 1	Mon. 2	Mon. 3	Mon. 4	Avg.	Rms Deviation
						$\frac{\text{Mon. 2}}{\text{Bare Thermal}}$		$\frac{\text{Mon. 4}}{\text{Bare Thermal}}$		$\left\{ \frac{1}{4} \sum_{i=1}^4 (m_i - \bar{m})^2 \right\}^{1/2}, \%$
32	9/4	1-1/2	40	5	1.0	1.0	1.0	1.0	1.0	---
28	9/4	H <sub>2</sub> O	42	1	.200	.204	.210	.207	.205	2.5
31	9/4	H <sub>2</sub> O	40	0.5	.099	.0995	.099	.099	.99	1.5
39	9/12	1-1/2	58	70	10.75	10.9	11.2	10.6	11.0	1.5
40	9/12	1-1/2	40	70	8.35	8.25	8.32	8.40	8.12	2.0
44	9/14	5	80	35	4.15	3.96	3.90	4.09	4.01	3.5
61	12/4	5	70	10	1.75	1.69	1.82	1.71	1.73	3.5

\*As recorded by the reactor instrumentation.

TABLE III.3

## FOIL CHARACTERISTICS

Detector	Abundance, %	Thickness, in.	Princ. Activity Counted	Ref. 18 $\sigma_{act}(.025 \text{ ev})$ b.	$\int_{epi}$	Ref. 19 $\sigma_{act}(E)$ b.	$\frac{dE}{E}$	Purity
Au	100	.001	.41 Mev $\gamma$	98		1558		Excellent
Mn	100	.002	.845 Mev $\gamma$	13.3		11.8		Poor Cu and Ni Impurities
Cu <sup>63</sup>	69 Nat. Abund.	.005	.51 Mev Annih. $\gamma$ from $\beta^+$	4.3		4.4		Excellent
Lu <sup>176</sup>	2.6 Nat. Abund. in 2.5 Lu-Al Alloy	.010	.208 Mev $\gamma$	360 b. at .14 ev Reson.		---		Excellent

to large errors. Cadmium cutoff energies are derived by Dayton and Pettus.<sup>20</sup> A 20 mil covering of cadmium around any of the foils listed in Table III.3 affords a cutoff energy for an equivalent perfect filter of .448 ev in an isotropic flux and .342 ev in a monodirectional flux. The region between these two energies is estimated to contribute less than 1/2 percent to the total activation in an assumed Maxwellian spectrum fitted with a  $1/E$  tail at .18 ev.

The foils were washed in acetone, weighed, and covered with a thin layer of paper and tape. It was determined that the covering material introduced no perturbation in the foil activation by carrying out several trial irradiations with various thicknesses of paper and tape. Bare and cadmium-covered foils were placed at least one inch apart at the mouth of the ducts. The perturbation induced by the cadmium on the bare foil at the mouth and on the one at the exit of the duct was estimated to be well within the normalization error.<sup>21</sup>

#### E. Counting Equipment

Except for occasional utilization of the multichannel analyzer, counting was done in a well counter equipped with a 3 in. x 3 in. NaI (Tl) scintillation crystal backed with a Dumont No. 6292 photomultiplier tube. A Radiation Instrument Development Laboratory Model 4951 scaler provided the high voltage to the photomultiplier. The discriminator was set well above the noise level and the high voltage was maintained in the center

of the counting plateau at 1275 volts. Reproducible positioning of foils in the well was accomplished with the aid of a test tube device incorporating a centering rod.

Stability of the system over long intervals of time was important. Figure 3.4 illustrates the measured decay of a gold foil over a 7-day period. Subsequent count rates were kept below the maximum in the figure to eliminate dead time corrections and to avoid jamming of the mechanical register. An absolute activity determination on the multichannel analyzer set an efficiency of 52 percent for the .41 Mev gold gamma rays.

#### F. Unperturbed Flux Distributions for the Water Reflector

The first experiment was done to verify that the current at the exit of the evacuated 1-1/2 in. duct was far in excess of the unperturbed flux in the vicinity of the duct exit. If this were the case, activations measured at the duct exit could be attributed solely to streaming contributions from the region close to the mouth of the duct. Thermal\* and episcadmium gold reaction rates were measured in the water bordering the south face of the reactor core out to four feet. The measurements were performed at the midplane of the core one row east of the position displayed in Figure 3.1. The relative reaction rates are plotted in Figure 3.5.

---

\*The thermal reaction rate is taken to mean the difference between bare and cadmium-covered measurements.



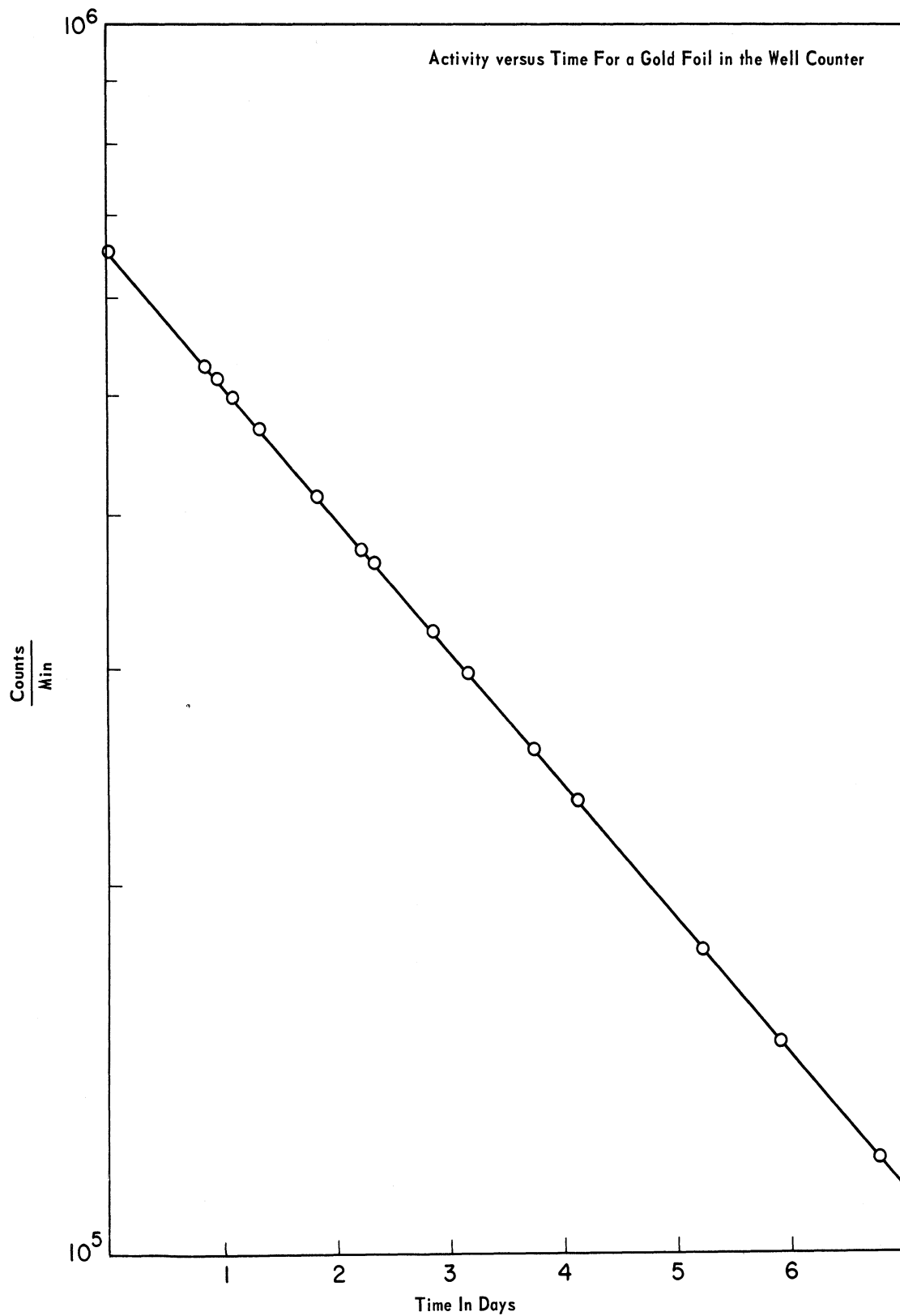


Figure 3.4. Decay of a gold foil counted in the well counter.

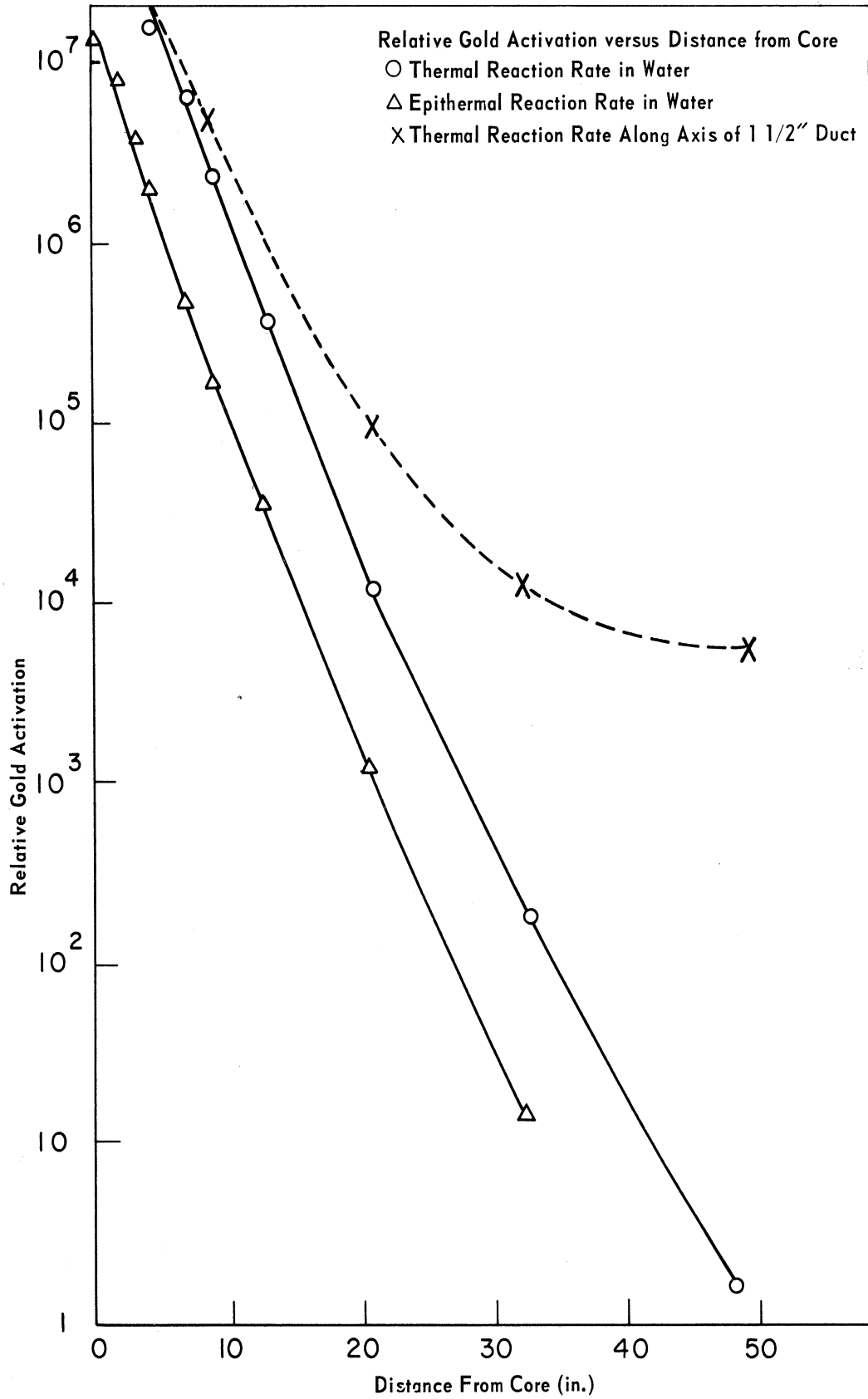


Figure 3.5. Thermal and epithermal flux out to four feet in water reflector and along axis of 1-1/2-in. duct.

Thermal reaction rate data for foils placed within the 1-1/2 in. duct positioned 5/16 in. from the reactor core are shown in the same figure. The bare and cadmium-covered measurements were made separately to prevent severe mutual shielding. The results demonstrate that the streaming current in the duct exceeds the unperturbed flux in the medium by greater than two orders of magnitude 3/4 in. from the duct mouth.

Of peripheral interest is the flux distribution in the core. Foil insertions were made between the plates of the fuel using 10 mil aluminum venetian blind slats for positioning. The disadvantage factor in the fuel plates of the FNR is nearly unity,<sup>22</sup> and for this reason measurements in the channels between plates are representative of the homogenized medium. Since the gold cadmium ratio is low within the core, copper foils were used for this measurement. The data are shown in Figure 3.6. The flags indicate the uncertainty in position and normalization. The results for groups three and four of a four-group, one-dimensional machine calculation are normalized to the data.

The flux peak in the two off-center fuel elements can be explained by the close proximity to the water channels serving the poison rods, which were nearly 100 percent withdrawn during the course of the experiment. Since access to the partial element was limited, the peaking effect in the vicinity of a water channel is demonstrated in Figure 3.7 by an east-west flux distribution in the element bordering the east side of the control rod element (see Figure 3.1).

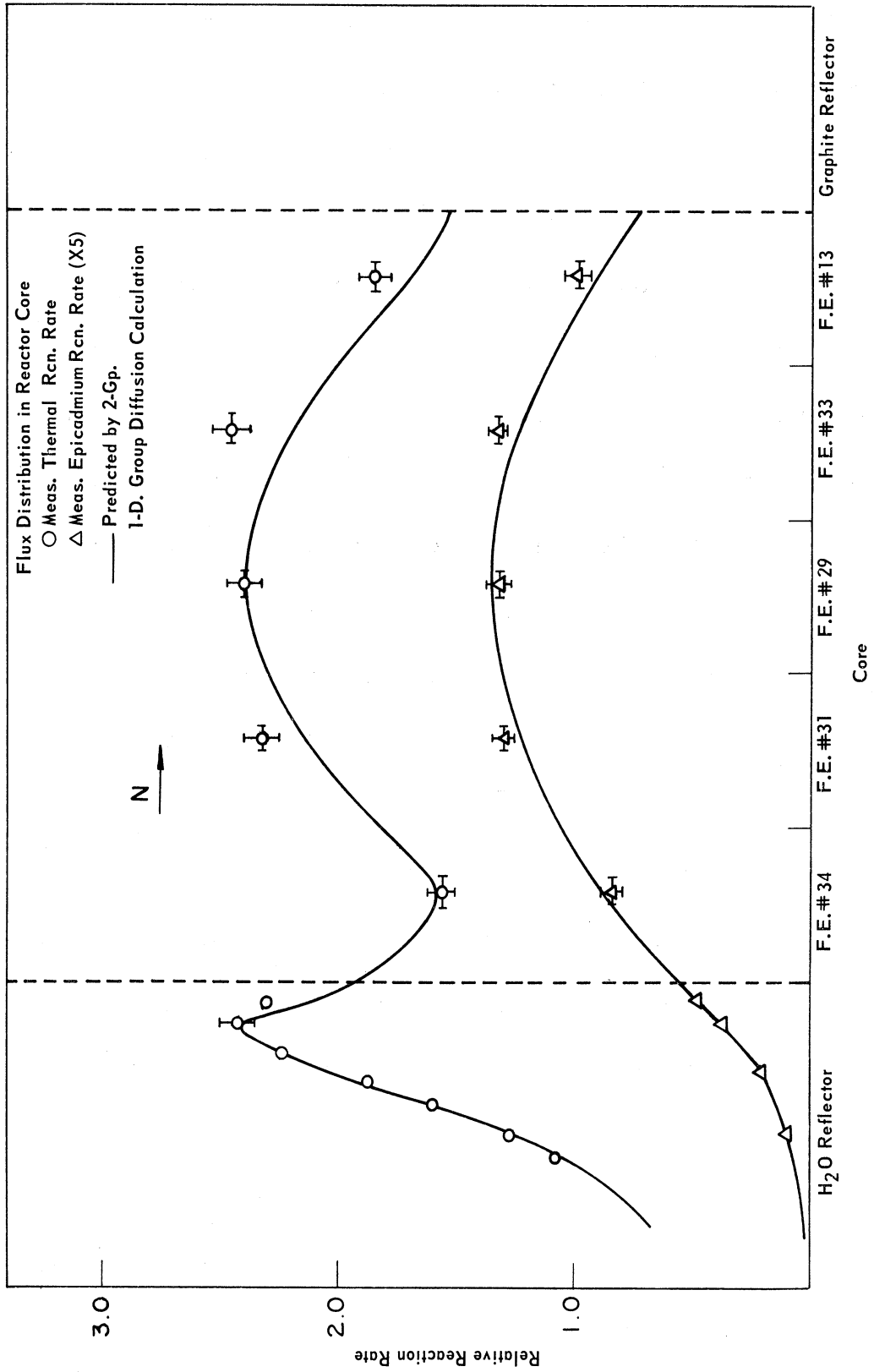


Figure 3.6. Thermal and epithermal flux in the core and the water reflector.

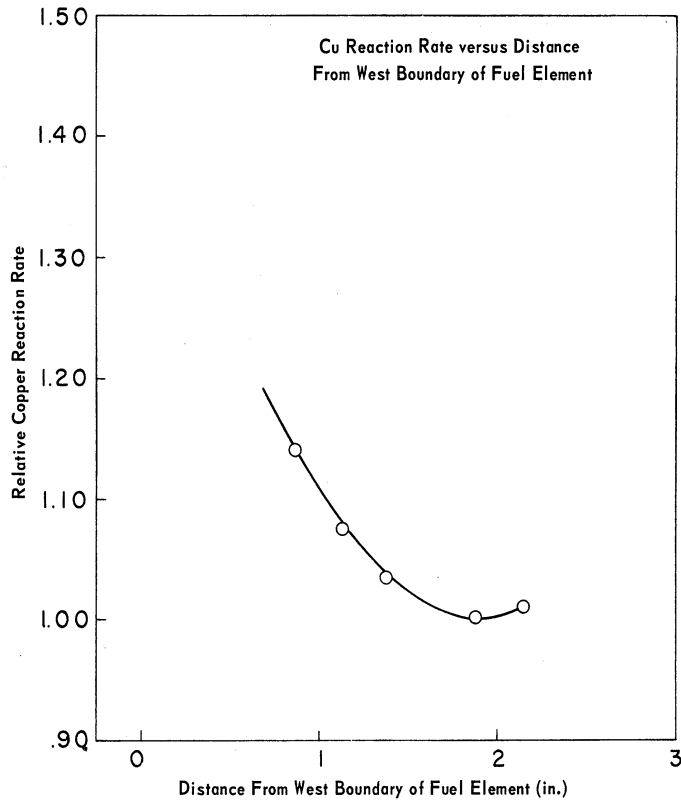


Figure 3.7. East-west traverse of thermal flux in the fuel element bordering on the east of the control rod element.

Most of the streaming measurements in water were performed with the duct axis positioned 4 in. below the core midplane in the column illustrated in Figure 3.1. This position was chosen to minimize the perturbing influence of the control rod. The unperturbed duct axis flux distribution at this position is plotted in Figure 3.8 out to 22 cm from the core. The data are normalized at 2.16 cm to the results of a two-group, two-dimensional group-diffusion code.

The data in Figure 3.8, as well as most of the subsequent results, are plotted on the basis of detector reaction rates. This presents the

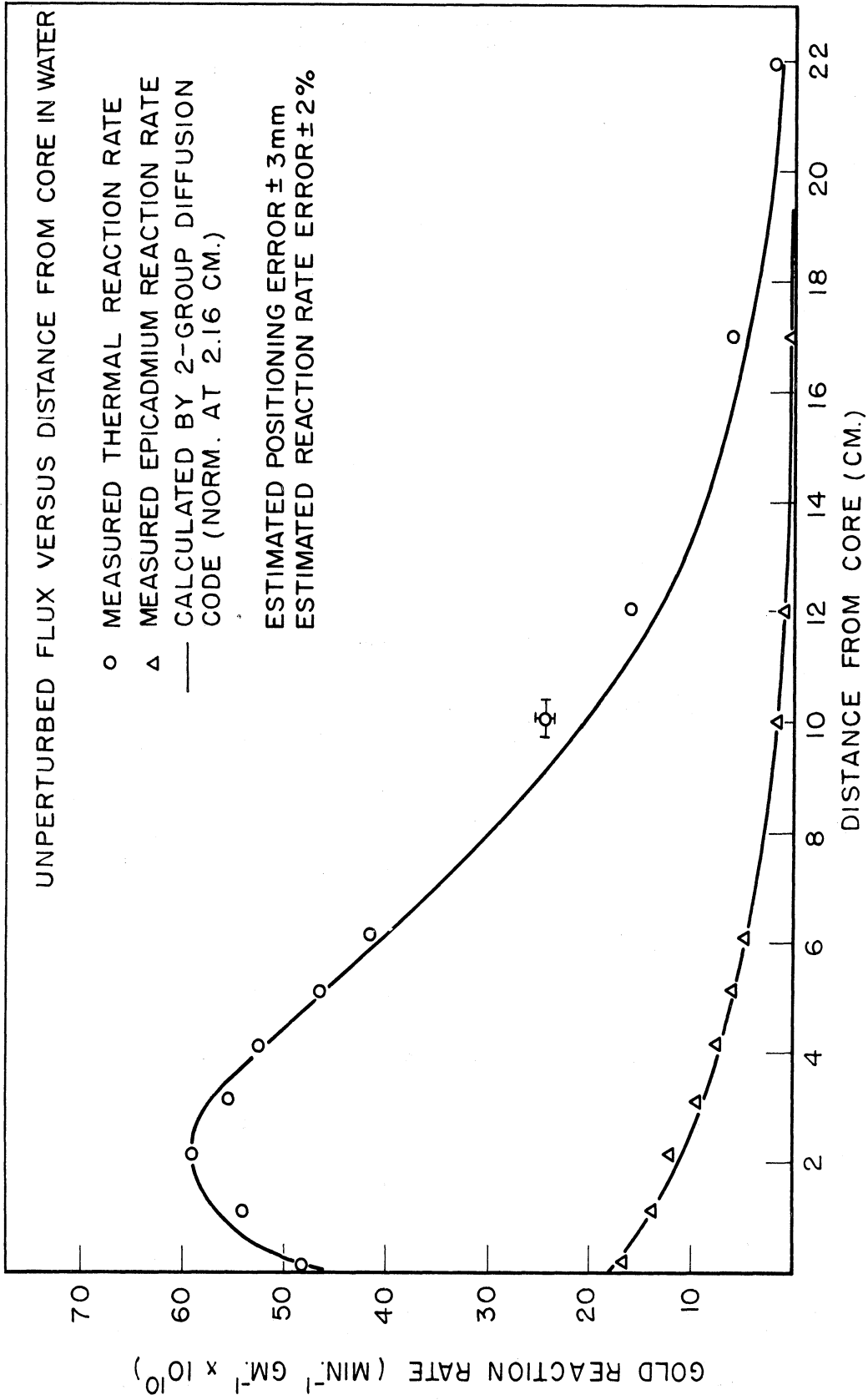


Figure 3.8. Unperturbed thermal and epicadmium flux in water reflector.

data in its raw form, yet it is a convenient form for interpretation in the present study. The normalization technique discussed earlier permits direct comparison of the results of measurements employing identical detectors.

Corrections for flux perturbations induced by the foils must be made before the ratios of epithermal to thermal fluxes can be evaluated. From the results of Dalton and Osborn<sup>23</sup> we estimate a low correction to the thermal flux measured by small 1 mil gold foils in water:

$$\frac{\phi^{th}}{\phi^{th}_{meas.}} = 1.04 \quad . \quad (3.1)$$

The self-shielding induced by the 4.9 ev gold resonance brings about a considerably larger correction to the epithermal reaction rate:<sup>24</sup>

$$\frac{\left\{ \int_{epi} \sigma_a(E) \frac{dE}{E} \right\}}{\left\{ \int_{epi} \sigma_a(E) \frac{dE}{E} \right\}_{meas.}} = 2.2 \quad , \quad (3.2)$$

for 1 mil gold foils.

Applying these corrections, a comparison can be drawn with the resulting ratios of epithermal to thermal flux predicted by the four-group code. Assuming a  $1/E$  epithermal spectrum and adopting the epithermal absorption integral in Table III.3 we get:

$$\frac{\phi^3}{\phi^4} = \frac{\int_{.625 \text{ ev}}^{5.53 \text{ Kev}} \phi(E)dE}{\int_0^{.625 \text{ ev}} \phi(E)dE} = .205, \quad (3.3)$$

at 2.16 cm in the water reflector (Figure 3.8). The four-group code predicts that  $\phi^3/\phi^4 = .195$ , a 5 percent deviation from the measured ratio.

### G. Preliminary Duct Experiments

With the evacuated 1-1/2-in. duct positioned at various distances from the core, bare and epicalcium reaction rates were measured at the duct exit. The data are presented in Figure 3.9. The thermal data are compared to predictions for the angular flux, obtained by using the unperturbed flux distribution in Eq. 2.41 to compute the boundary condition, a group-diffusion calculation to obtain the perturbed flux distribution at the duct mouth, and Eq. 2.30 for the angular flux. It is noteworthy that the peak occurs at a duct position closer to the core than the position of the unperturbed flux peak in the medium.

The same measurement was performed in a 4 in. x 4 in. x 28 in. graphite insert bored with a 1-1/2-in. axial hole to accommodate the duct. The insert was positioned flush against the reactor core as shown in Figure 3.3, and the duct was moved in steps of 1 in. by introducing graphite plugs into the hole in front of the duct. The thermal flux data in the solid insert as well as the streaming data at the duct exit are plotted in Figure 3.10. The dotted lines represent the previous water data for comparison.



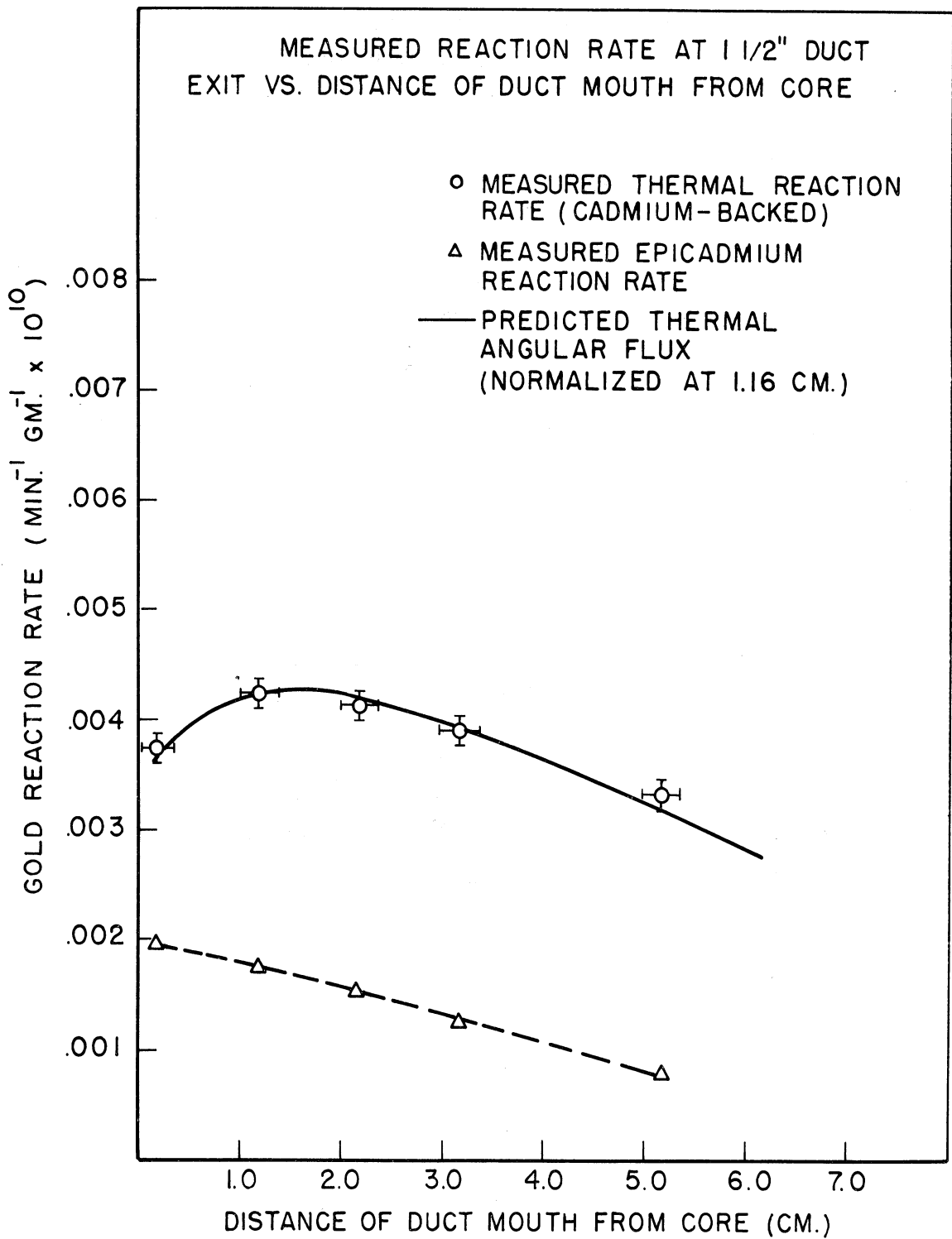


Figure 3.9. Reaction rate at exit of 1-1/2-in. duct in water.

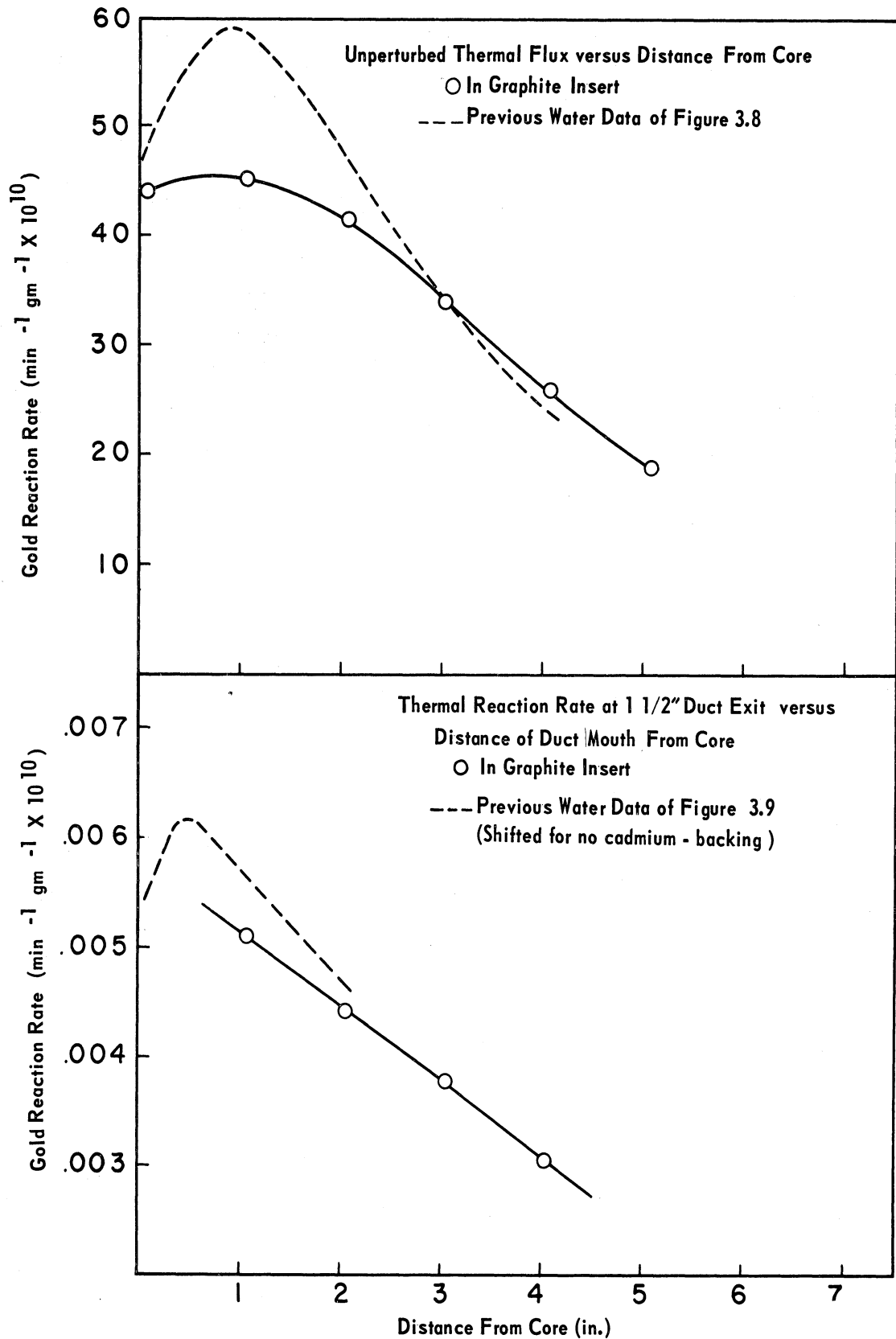


Figure 3.10. Thermal reaction rate in 4-in. graphite insert and at the exit of 1-1/2-in. duct encased in 4-in. graphite insert.

To compare the data with predictions for the actual magnitude of  $j_{Bth}^+$  at the duct exit it was necessary to measure the leakage contributions from the duct walls and also the effect of activation from back-scattering at the exit. Measurements with the duct positioned at 2.16 cm in water resulted in the compilation of Table III.4. A 23 percent back-

TABLE III.4

## PREDICTION OF ACTIVATION AT EXIT OF 1-1/2 INCH DUCT IN WATER

Exit Measurement		
Bare reaction rate	.00691 x 10 <sup>10</sup>	gm <sup>-1</sup> -min <sup>-1</sup>
Cd.-backed reaction rate	.00531 x 10 <sup>10</sup>	"
Cd.-covered reaction rate	.00142 x 10 <sup>10</sup>	"
Thermal monodirectional reaction rate	.00389 x 10 <sup>10</sup>	"
Reaction rate from walls of duct	.00082 x 10 <sup>10</sup>	"
Net thermal monodirectional reaction rate from mouth of duct	.00307 x 10 <sup>10</sup>	"
Net thermal monodirectional reaction rate from mouth of duct $j_{Bth}^+$ (corr. for cntg. 1/4 in. foil)	.00322 x 10 <sup>10</sup>	"
Mouth Prediction		
Direct streaming from .6875 in. of radius of duct	.00286 x 10 <sup>10</sup>	"
Transmission through wall from last .0625 in. of radius	.00035 x 10 <sup>10</sup>	"
Net direct streaming prediction from mouth $j_{Bth}^+$	.00321 x 10 <sup>10</sup>	"

scattering contribution was revealed by backing the bare foils with cadmium. A wall contribution of 21 percent was measured by covering the mouth of the duct with cadmium. A 5 percent correction originated from

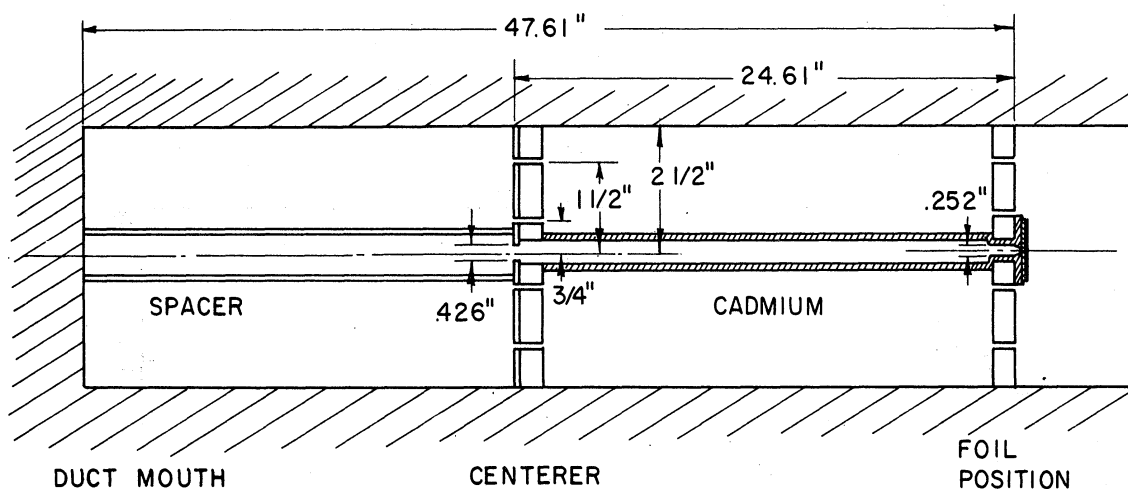


Figure 3.13. Collimator design.

neutron detector at the exit to view .905 sq. in. of the mouth regardless of the duct diameter.

The high epithermal content of the spectrum at the collimator exit necessitated employment of a detector possessing a relatively low resonance integral. Manganese combined this attribute with a high activation rate.\* The bare and cadmium-covered foils were irradiated simultaneously by offsetting the covered foils by  $3/8$  in. from the centerline. A copper impurity in the manganese required that the foils be counted in the single channel well counter within one manganese half-life.

The results of the collimator measurements are plotted in Figure 3.14.

\*The reactivity perturbations induced by the introduction of the larger ducts caused power fluctuations in the reactor system. Since the measuring foils and normalizing foils possessed different decay constants, the transient was not automatically corrected for by the normalizing foils. It was necessary to evaluate the normalization by the analysis presented in Appendix F.

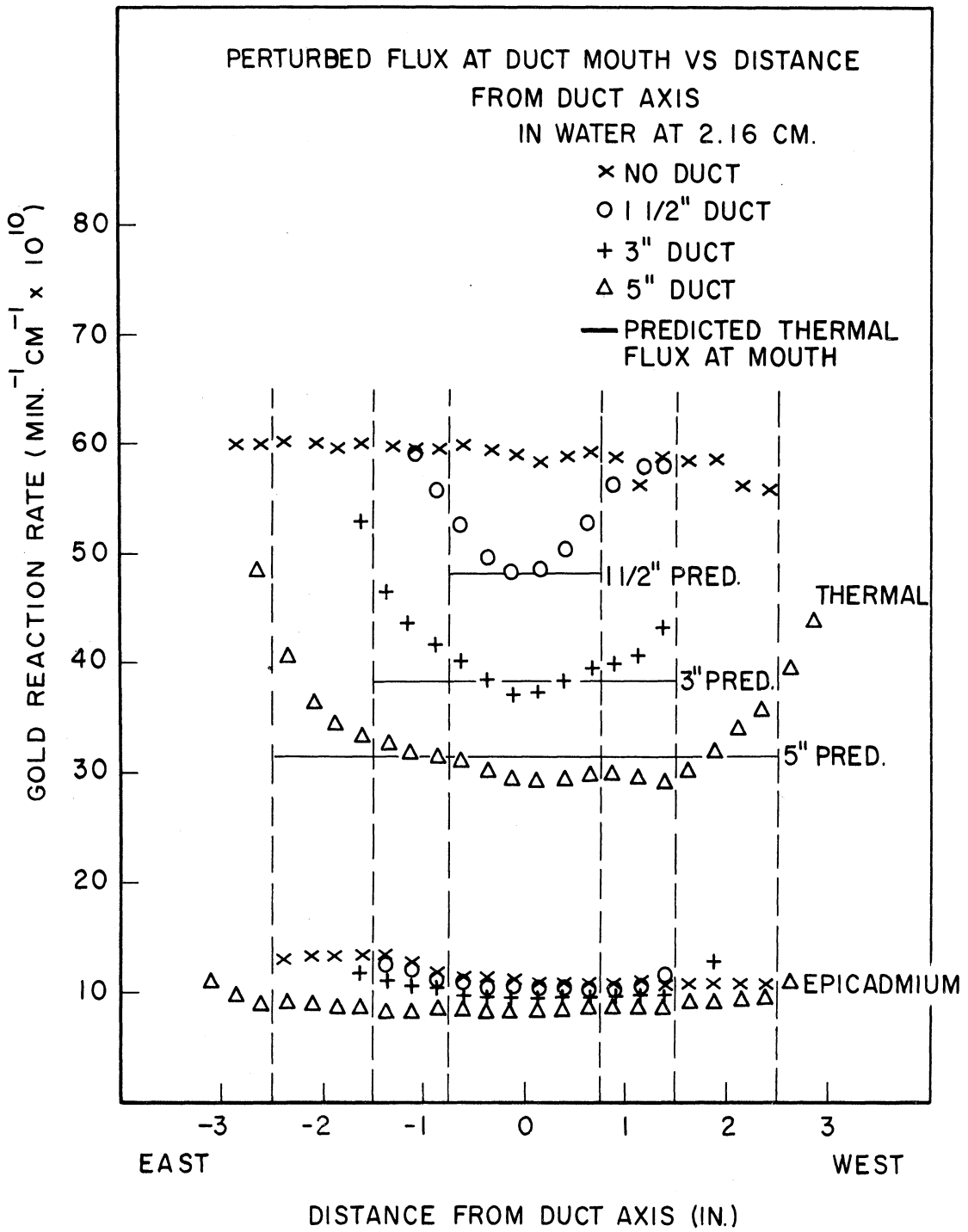


Figure 3.11. Perturbed radial flux distributions at duct mouths.

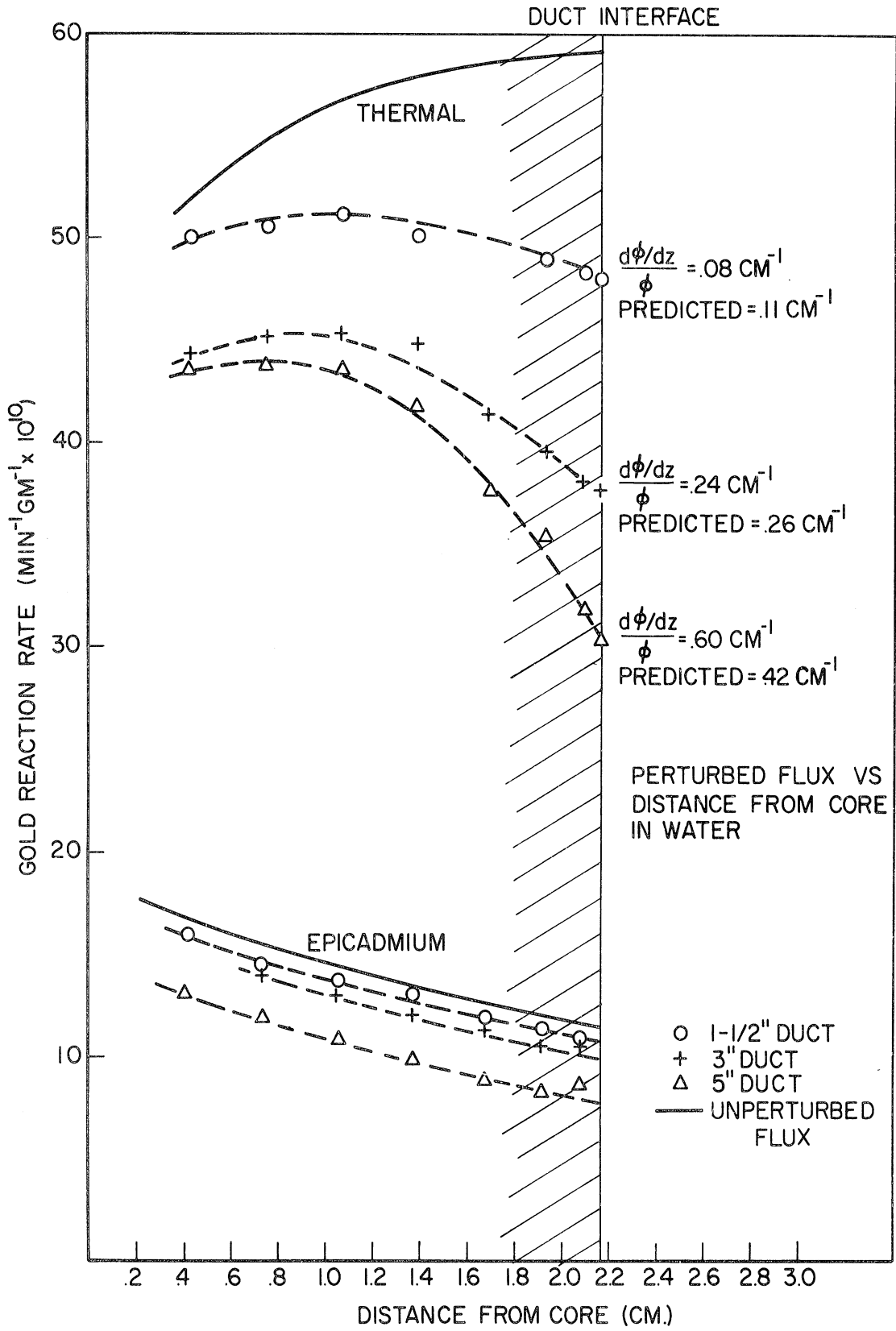


Figure 3.12. Perturbed axial flux distributions at duct mouths.

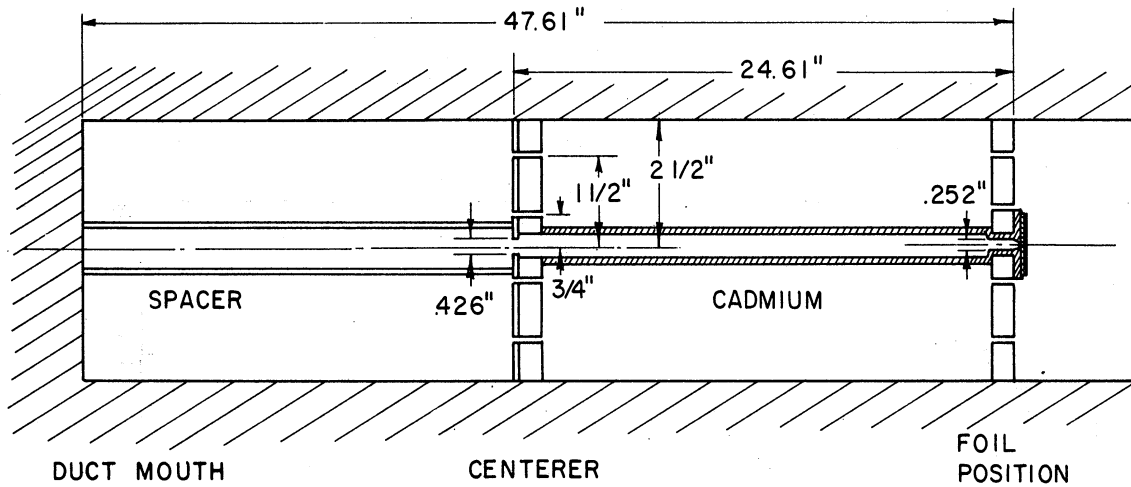


Figure 3.13. Collimator design.

neutron detector at the exit to view .905 sq. in. of the mouth regardless of the duct diameter.

The high epithermal content of the spectrum at the collimator exit necessitated employment of a detector possessing a relatively low resonance integral. Manganese combined this attribute with a high activation rate.\* The bare and cadmium-covered foils were irradiated simultaneously by offsetting the covered foils by  $3/8$  in. from the centerline. A copper impurity in the manganese required that the foils be counted in the single channel well counter within one manganese half-life.

The results of the collimator measurements are plotted in Figure 3.14.

\*The reactivity perturbations induced by the introduction of the larger ducts caused power fluctuations in the reactor system. Since the measuring foils and normalizing foils possessed different decay constants, the transient was not automatically corrected for by the normalizing foils. It was necessary to evaluate the normalization by the analysis presented in Appendix F.

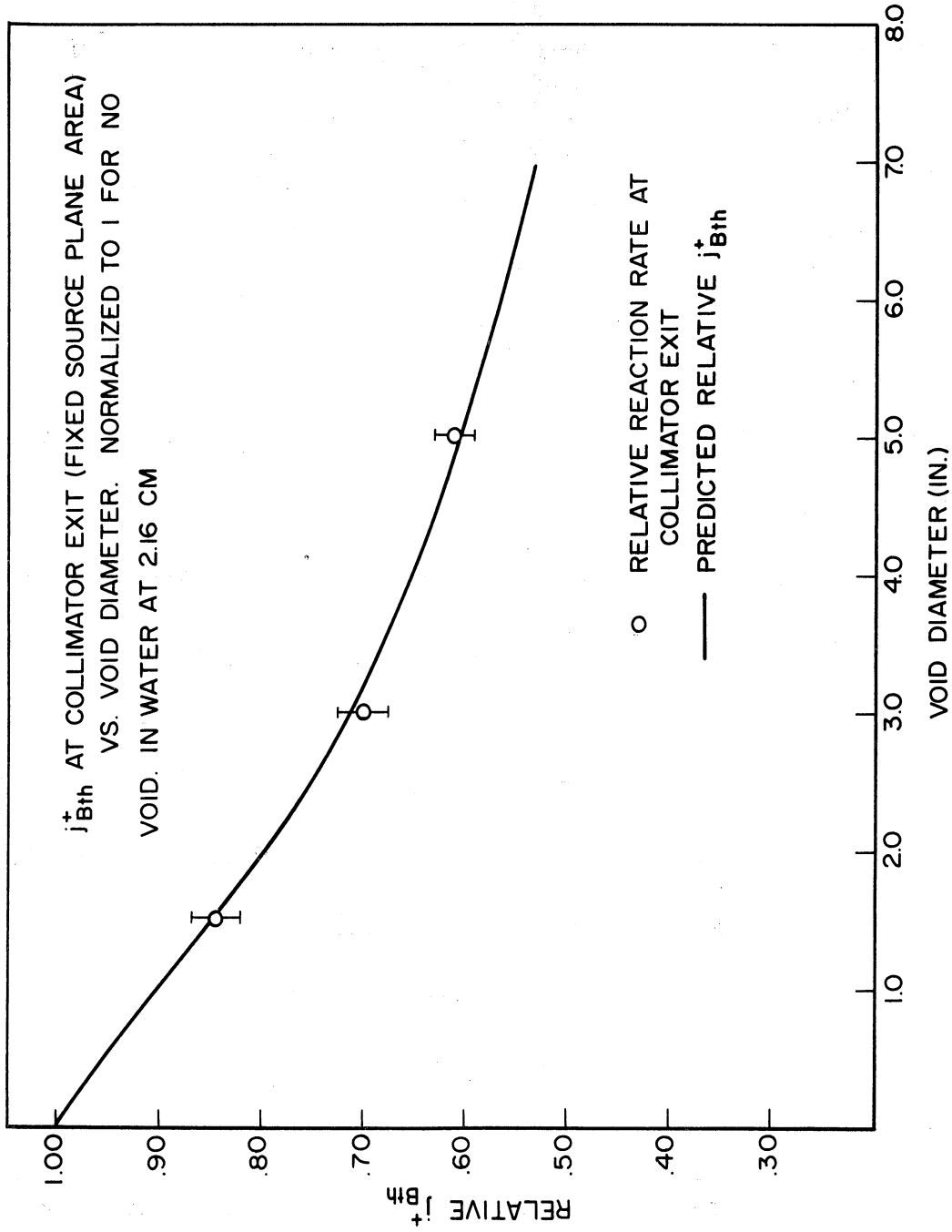


Figure 3.14.  $j_{Bth}^+$  at collimator exit.



The solid line presents the prediction for  $j_{B_{th}}^+$ . The data and the predictions for  $j_{B_{th}}^+$  are normalized to a value of unity for no void.

### 3. Thermal Flux Attenuation Within the Empty Ducts

The behavior of the flux within the empty duct is related to the main topic of this study, and a series of experiments was performed to examine the attenuation of the forward component of the thermal flux. Bare and cadmium-covered measurements were performed separately. The detectors consisted of 1/16 in. square 1 mil gold foils. The bare foils were backed with cadmium, which posed the formidable problem of mutual shielding. In order to avoid the laboriousness of separate runs for each foil position, the five foils were positioned to avoid shadowing by spacing them 60° apart. Investigations within the 5 in. duct demonstrated that the radial flux was reasonably flat near the exit of the 5 in. duct (Figure 3.15).

The thermal reaction rates within the 1-1/2 in. and 5 in. ducts as a function of axial distance from the mouth are plotted in Figure 3.16. The measured slopes at 44 in. are recorded in the figure.

#### I. Thermal Spectrum

A question of some concern was the influence of the void on the thermal spectrum, and consequently the spectral effect on the apparent perturbations measured. Results published by Walton et al.<sup>25</sup> indicate no

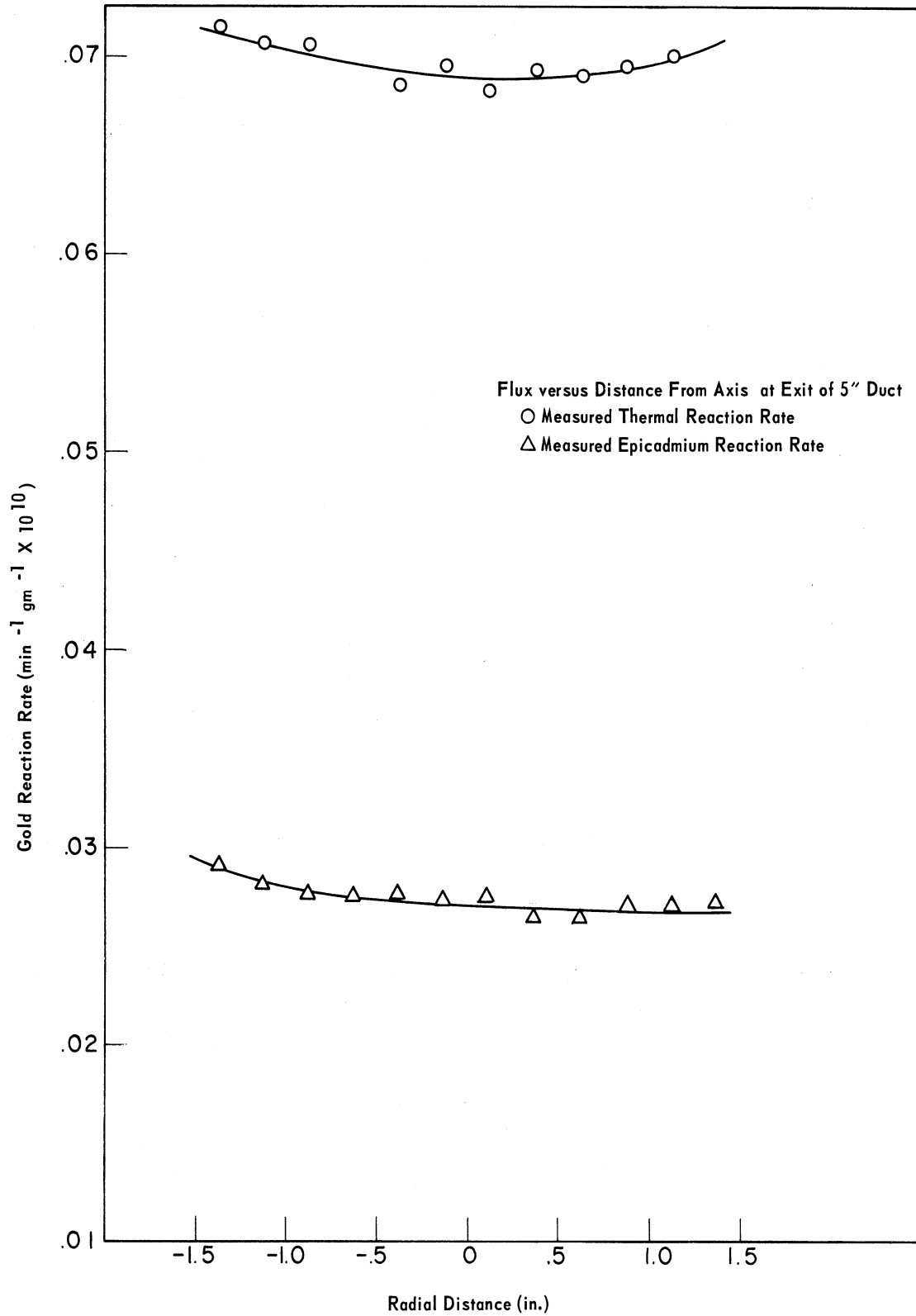


Figure 3.15. Radial variation of flux at 5-in. duct exit.

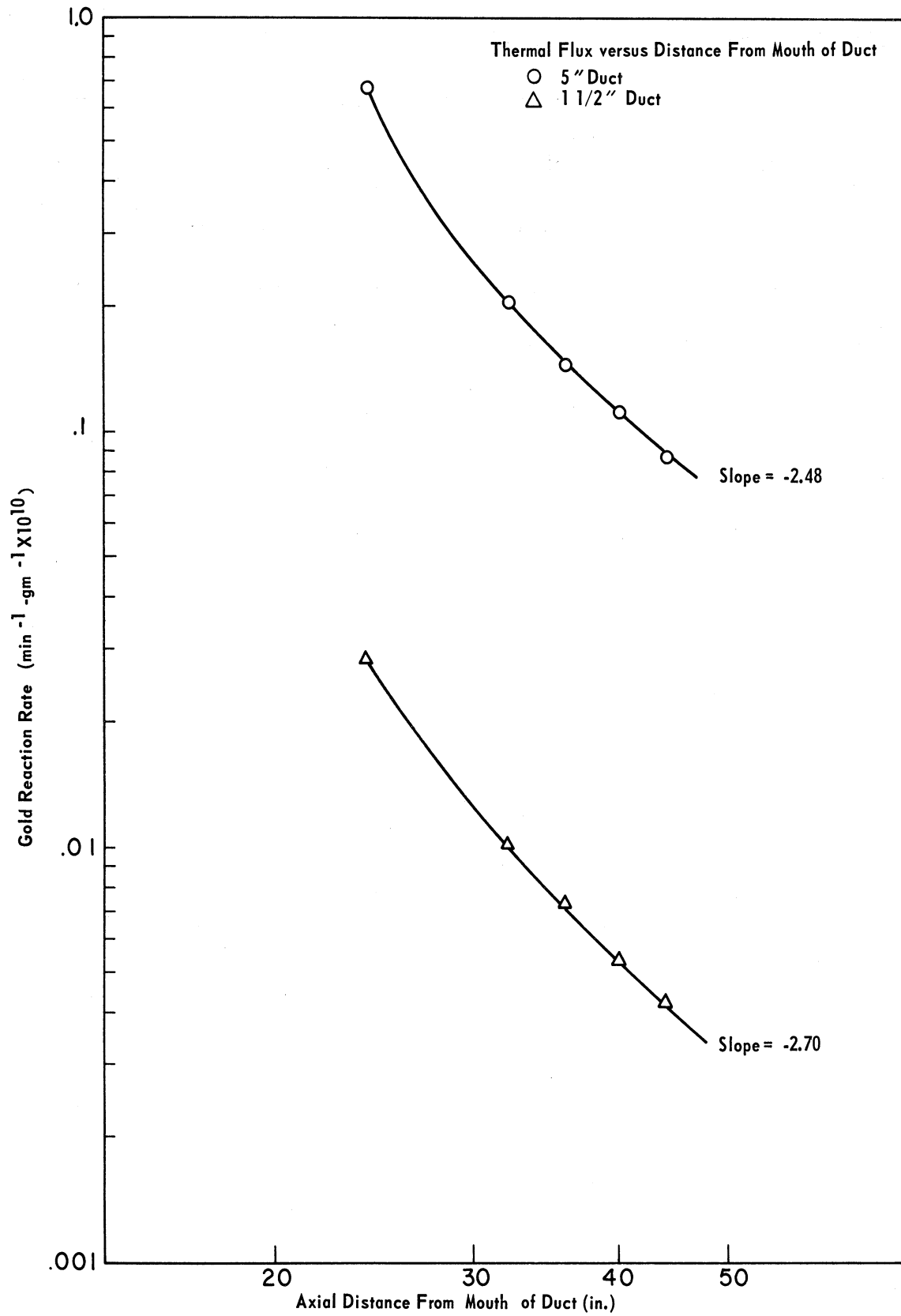


Figure 3.16. Thermal flux attenuation within 1-1/2- and 5-in. ducts.

hole effect on the spectrum in polyethylene with voids up to 2 in. in diameter. The effect of the 5 in. duct on the thermal neutron temperature at the mouth was measured using the .14 ev resonance in the  $\text{Lu}^{176}$  absorption cross section as a spectral index. Bare and cadmium-covered 10 mil, 2-1/2 percent Lu-Al foils were irradiated simultaneously with manganese\* at the mouth of the voided 5 in. duct and at the same positions with the duct filled with water. The activities were measured on a multichannel analyzer corrected for drift with a  $\text{Co}^{59}$  standard. The resultant activities are listed in Table III.5.

TABLE III.5

## NEUTRON TEMPERATURE MEASUREMENT

$\text{H}_2\text{O}$ Medium	
Bare $\text{Lu}^{176}$	$21.82 \times 10^5 \text{ gm}^{-1}\text{-min}^{-1}$
Cd.-covered $\text{Lu}^{176}$	...
Bare Mn	$11250 \times 10^5$ "
Cd.-covered Mn	$356 \times 10^5$ "
$A^{\text{th}}(\text{Lu}^{176})/A^{\text{th}}(\text{Mn})$	.00200
5 in. Void	
Bare $\text{Lu}^{176}$	$10.99 \times 10^5 \text{ gm}^{-1}\text{-min}^{-1}$
Cd.-covered $\text{Lu}^{176}$	...
Bare Mn	$5561 \times 10^5$ "
Cd.-covered Mn	$276 \times 10^5$ "
$A^{\text{th}}(\text{Lu}^{176})/A^{\text{th}}(\text{Mn})$	.00208

\*Manganese was used as the l/v detector because  $\text{Lu}^{175}$  possesses a large resonance integral, giving a cadmium ratio of only 1.59 for the voided duct.

The ratio of the reaction rate of  $\text{Lu}^{176}$  to that of  $1/v$  detector is calculated using the form of the resonance given by Schmid and Stinson:<sup>26</sup>

$$\sigma(E)\sqrt{E} = \frac{\text{Const.}}{1 + 1108(E-.142)^2} \quad (3.4)$$

The calculated ratio, normalized to unity at  $0^\circ\text{C}$ , is plotted up to  $100^\circ\text{C}$  in Figure 3.17. In this range of temperatures, the observed ratios suggest a temperature rise at the mouth of the voided duct of  $10^\circ \pm 5^\circ\text{C}$ . A  $10^\circ\text{C}$  temperature rise at  $300^\circ\text{K}$  would account for a 1.7 percent depression in the average activation cross section of a  $1/v$  detector.

#### J. Measurements in Complete Graphite Reflector

Graphite was chosen as a second medium in which to examine duct effects. The selection of graphite was based upon diffusing properties widely different\* from those of light water, as well as accessibility at the FNR. The south face of the core illustrated in Figure 3.1 was covered with three rows of 3 in. x 3 in. graphite reflector elements, except for two columns at the center, which were left open to accommodate the solid graphite (reactor grade) insert sketched in Figure 3.18. The axis of the 5 in. hole bored through the graphite was along the centerline of the reactor core. Graphite plugs were designed to accommodate 1-1/2 and 3 in. aluminum ducts.

---

\*The thermal diffusion coefficient for light water is .155 cm and for pure graphite .915 cm.

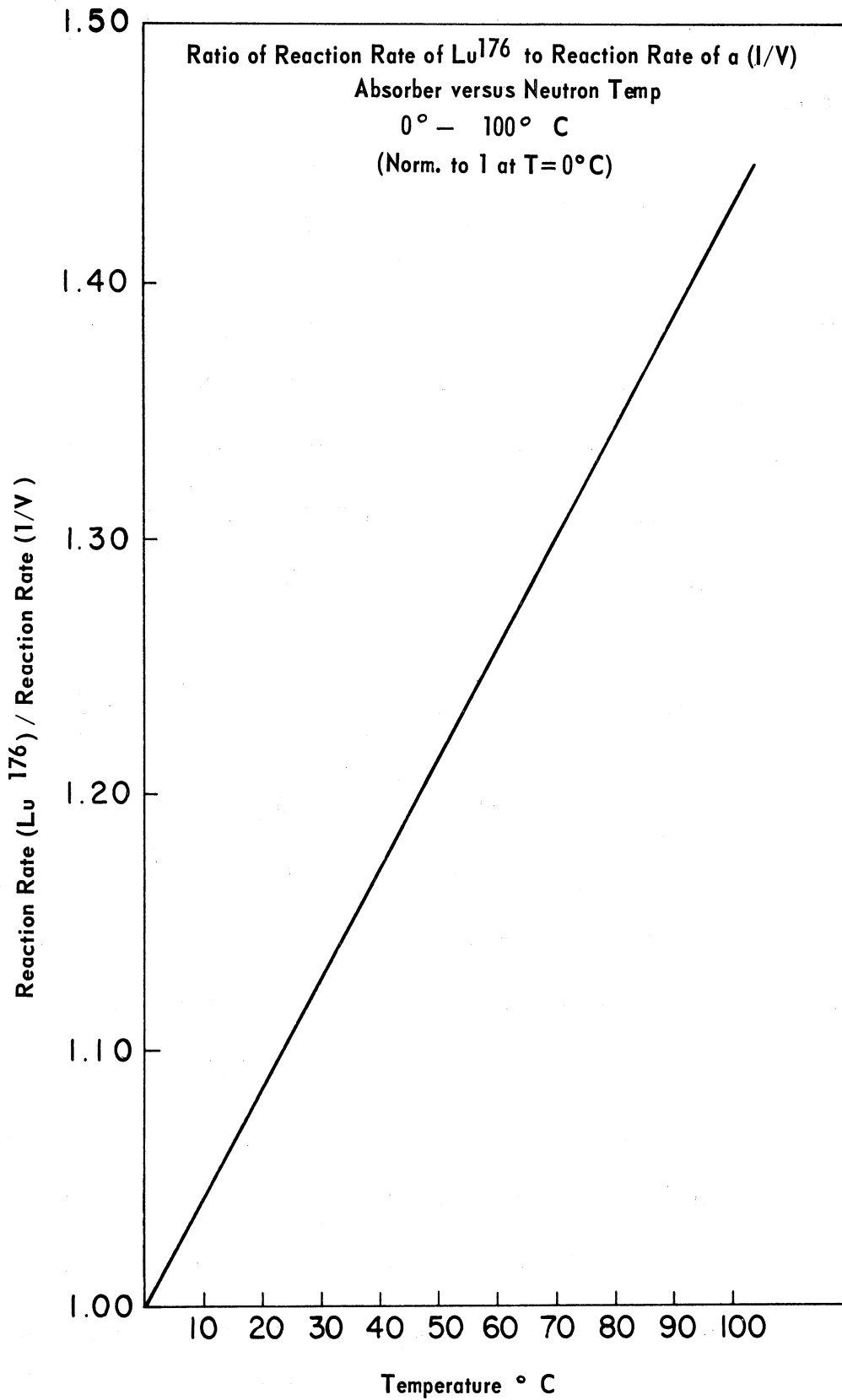


Figure 3.17. Ratio of reaction rate of Lu<sup>176</sup> to reaction rate of 1/v absorber.

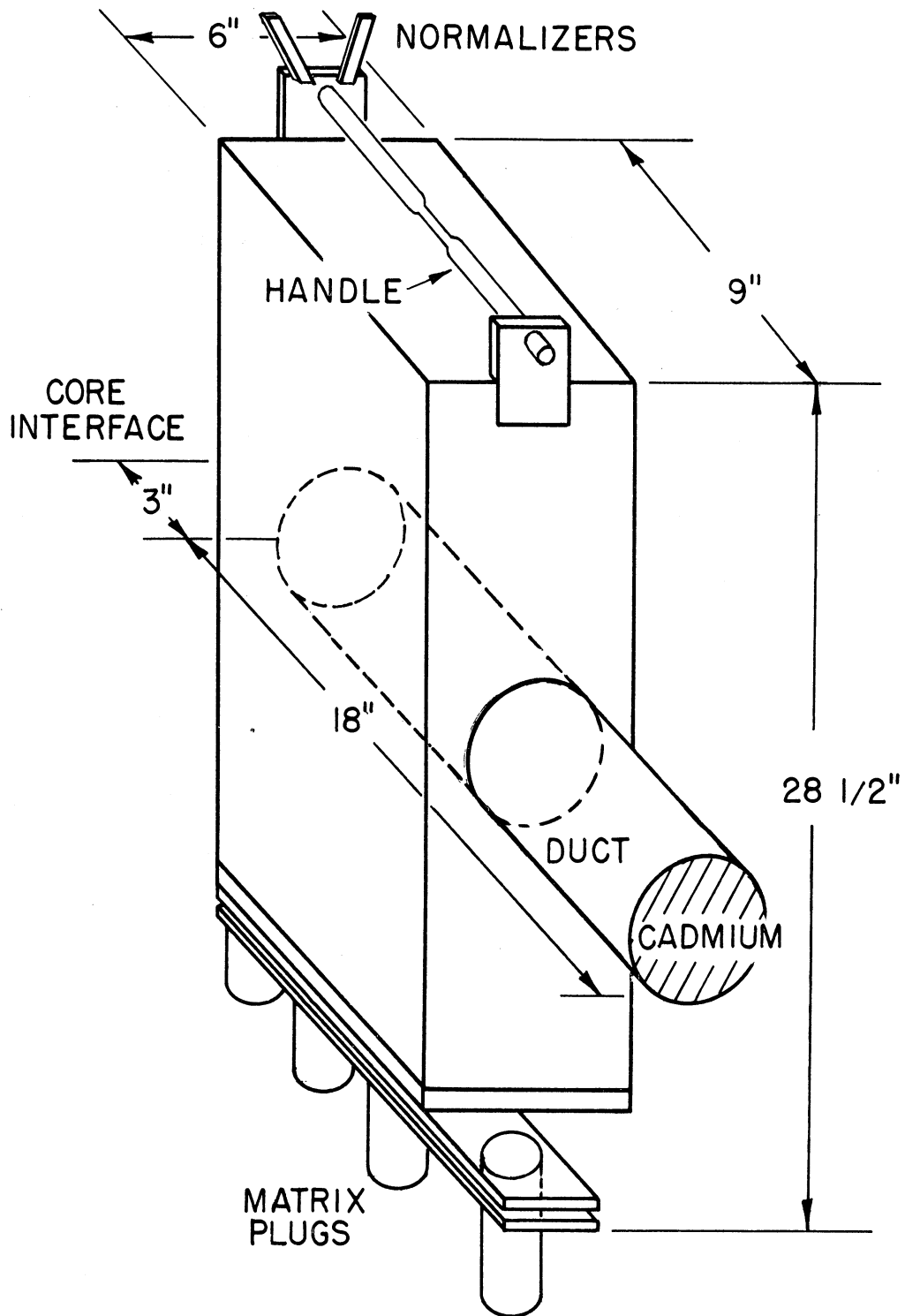


Figure 3.18. Graphite insert.

Measurements were made with the insert positioned against the south face of the reactor core. The side clearance was such as to allow no more than a .050 in. water gap between the insert and the columns of reflector elements. Time limitations allowed only scalar fluxes at the duct mouth to be measured. For this reason, the duct lengths were limited to 1-1/2 ft., which is effectively a void of infinite length from the standpoint of the perturbation at the mouth of the largest duct. The ducts were evacuated and positioned 3 in. from the core-graphite interface.

It was anticipated that water absorption might be a serious problem. To avoid the consequences of water penetration the graphite insert was coated with a thin layer of an Epoxy resin. It was verified that this was an effective sealer by soaking coated and uncoated samples of graphite in water and weighing shortly after removal.

Since the insert represented a large amount of reactivity, the reactor was brought critical with the insert in place on the south face of the core. The normalization was accomplished with four foils extending into the water from lucite brackets. Comparing the normalization results with counts from the fission chambers revealed that normalization was not influenced by the presence of the ducts.

Inasmuch as the thermal neutron mean free path is long in graphite, simultaneous bare and cadmium-covered measurements were avoided. A cadmium ratio of 25 in the graphite permitted the use of bare foil measure-



ments exclusively. If the epicalcium flux had been perturbed by the 5 in. duct to the same extent as the thermal flux, such a procedure could lead to an error of no more than 1-1/2 percent.

Figure 3.19 presents the results of unperturbed flux measurements in the solid graphite insert. The results are normalized at 7.62 cm to the distributions obtained by a two-group, one-dimensional diffusion calculation. A radial traverse is shown in Figure 3.20.

The flux measurements at the duct mouth were made at two positions 3/8 in. from the centerline, and agreed within 1 percent. The data are plotted in Figure 3.21. The solid line is the predicted scalar flux at the mouth obtained by using the measured unperturbed flux distribution to compute the boundary condition. Figure 3.22 displays the axial distribution at the mouth of the 5 in. duct and compares the data with the diffusion theory result.

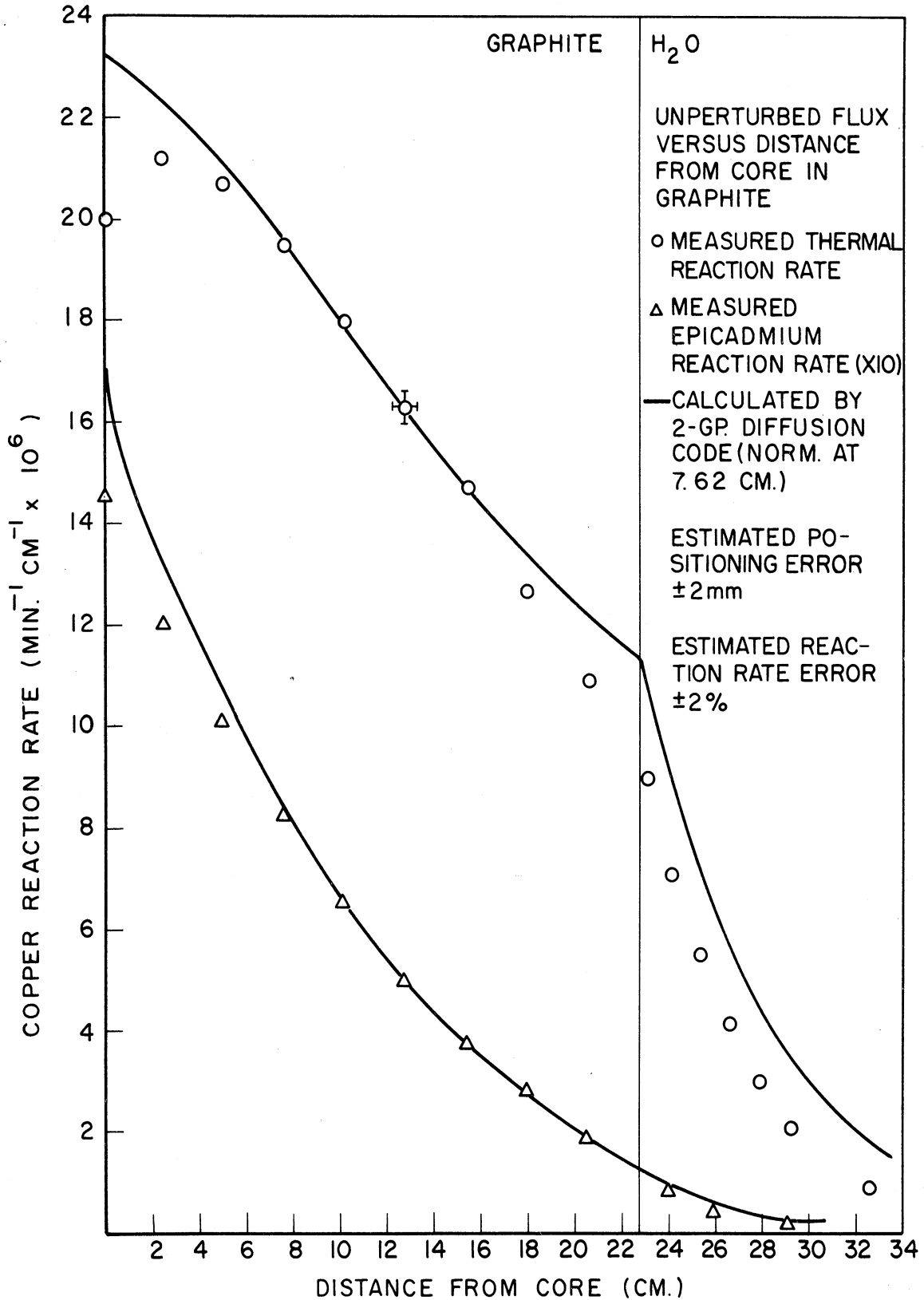


Figure 3.19. Unperturbed thermal and epicadmium flux in graphite insert.

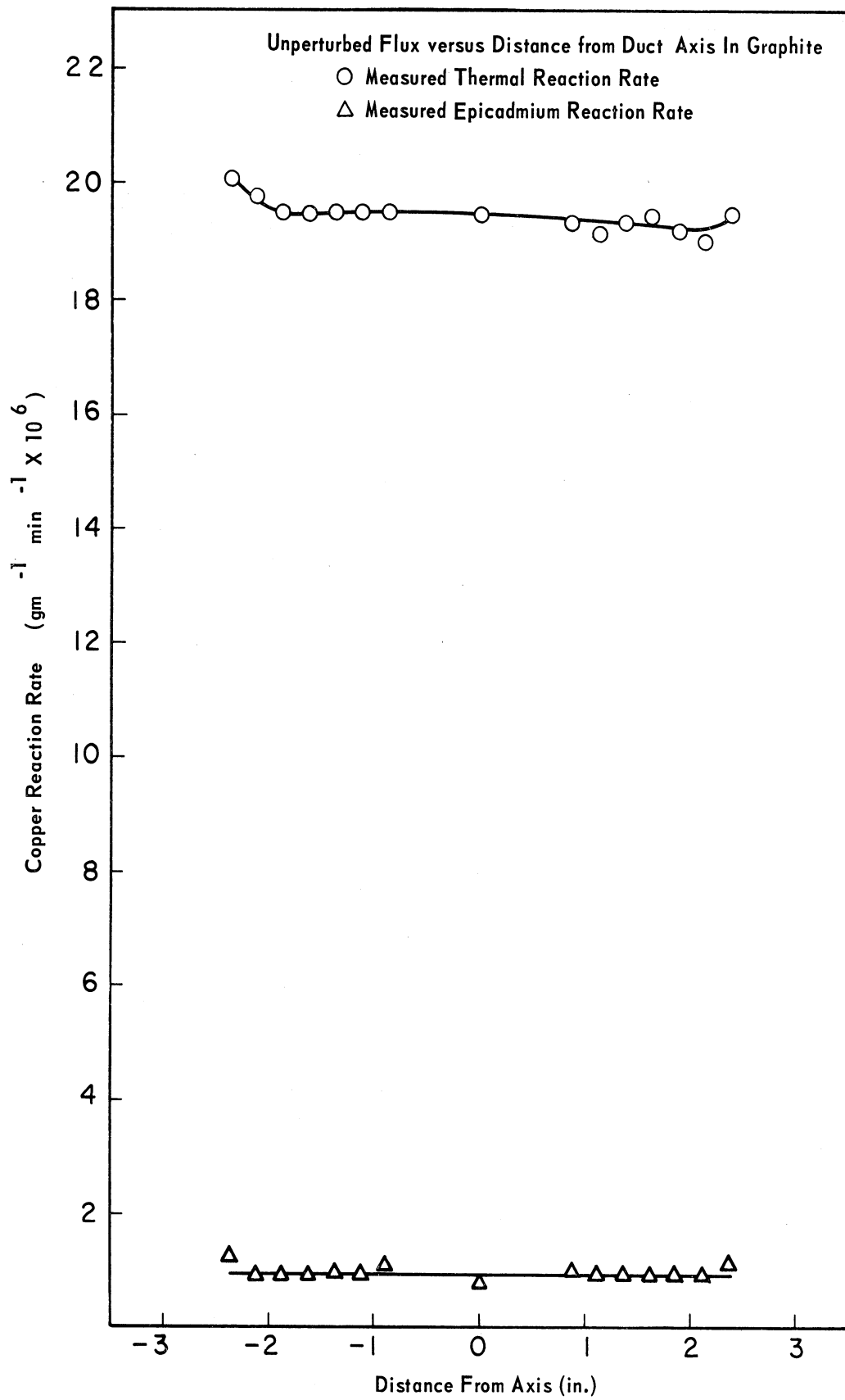


Figure 3.20. Radial flux distribution in graphite insert.

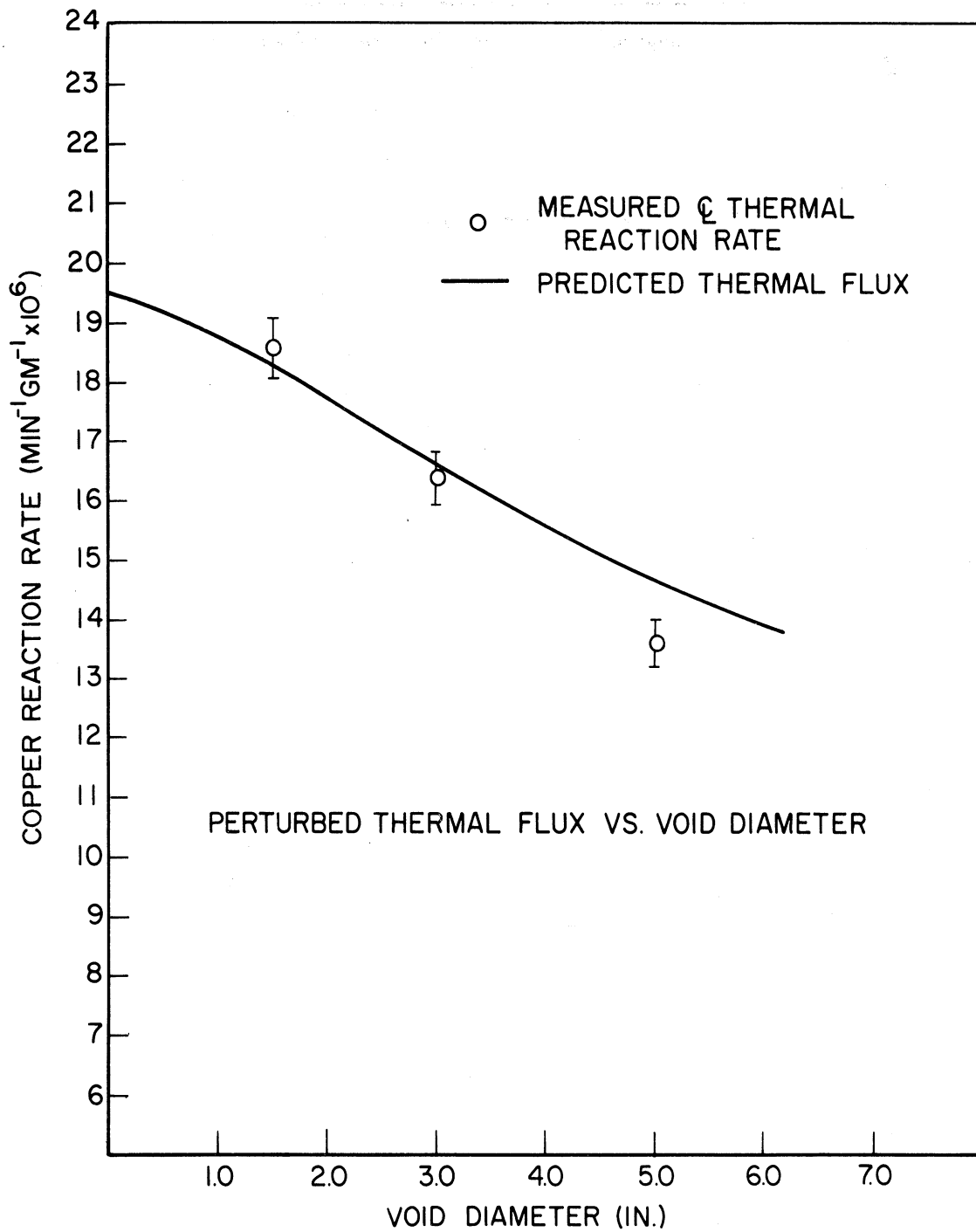


Figure 3.21. Perturbed thermal flux at center of duct mouths in graphite.

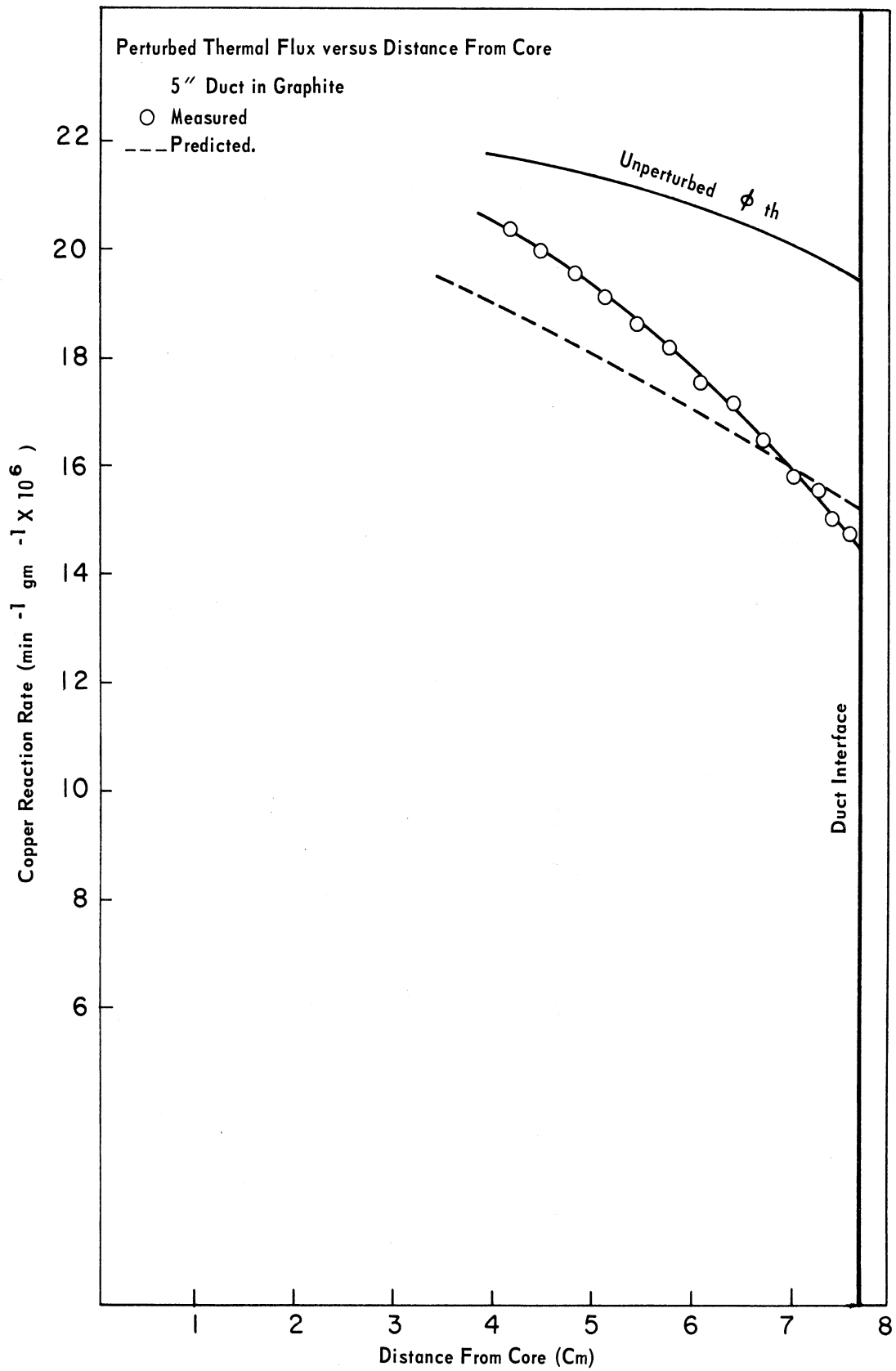


Figure 3.22. Axial distribution of thermal flux at mouth of 5-in. duct in graphite.

## IV. DISCUSSION

### A. Unperturbed Thermal Flux Distributions

The measured unperturbed thermal flux distributions, rather than the computed ones, were used to obtain the predictions presented in Chapter III. Utilization of the computed unperturbed thermal flux distributions, however, leads to no more than 3 percent disparity in the prediction of the duct mouth thermal flux at the positions studied. This is significant in that it suggests that duct perturbations can be predicted from diffusion theory flux distributions without the need for experiment. It should be pointed out, however, that the unperturbed flux shape in the immediate vicinity of the duct mouth must be accurately described by theory.

It is generally recognized that few-group diffusion theory has limitations when used to predict accurate flux distributions in reflectors. The cross section averaging procedure<sup>27</sup> and the high degree of fast flux anisotropy<sup>28</sup> give rise to deviations between theory and experiment. Theory and experiment are compared in Figures 3.8 and 3.19. The percentage deviation increases with distance from the core, although for the graphite reflector the situation is complicated by the existence of interfaces between highly dissimilar media. Utilization of more than two groups in the few-group scheme does not improve the agreement. No attempt has been made to include spectral effects close to the core-

reflector interface, nor has the curvature of the fuel element, which introduces up to 1/4 in. of water in front of the graphite insert, been considered. Infinite medium, Maxwellian-averaged cross sections were used in the reflector region. Presumably accurate predictions for the flux distribution far into the reflector region can be attained provided that appropriate transport and multigroup techniques are utilized. A thorough examination of this problem is beyond the scope of this study.

#### B. 1-1/2-In. Duct Experiments

The agreement between the experimental data shown in Figure 3.9 and the prediction based upon the perturbed angular flux at the duct mouth is good. It should be recalled, however, that unlike the calculations the measurements include the leakage contribution from the walls of the duct. This implies that the wall leakage contribution in the region examined is either a small or a constant percentage of the mouth contribution. Measurements with the duct at 2.16 cm indicate a 21 percent contribution from the walls. This number compares well with the results of similar measurements reported by Piercey.<sup>10</sup> Summing contributions from the lateral surfaces based upon the unperturbed thermal flux in the medium, a wall leakage contribution of 15 percent is predicted. The disparity of 6 percent could be accounted for by an albedo\* contribution

---

\*The albedo contribution is taken to mean neutrons of all energies which, having entered the duct through the mouth, make at least one scattering collision in the wall before they diffuse back into the duct and are detected as thermal neutrons.

of the fast neutrons passed by the cadmium.

Subtraction of the wall leakage contribution permits the prediction of  $j_{B_{th}}^+$ . The excellent agreement presented in Table III.4 suggests that any thermal neutron albedo contribution from the mouth at the exit of the 1-1/2 in. duct lies within the experimental error.

The 1-1/2 in. duct was provided with the internal collimator sketched in Figure 3.13 to completely eliminate duct wall and albedo considerations. A measurement was performed with identical copper foils at the duct mouth and the collimator exit. This permitted a convenient comparison between the experimental value and the prediction for the mouth contribution to the exit thermal activation. The difference between the two was within the uncertainty in the collimator dimensions. Unfortunately no data comparable to the uncollimated data of Figure 3.9 were obtained.

### C. Thermal Flux Attenuation Within the Empty Ducts

The "duct streaming" measurements within the empty 1-1/2 in. and 5 in. ducts were motivated more out of academic interest than from any direct bearing on the main theme of this study. It was of interest to determine whether the thermal flux far from the mouth of the duct obeyed the  $1/r^2$  geometrical attenuation predicted by Simon and Clifford.<sup>9</sup> The cadmium-backed foils were allowed to view all surfaces of the duct directly in front of them in order to include the albedo contribution. For the 1-1/2 in. duct  $h/R = 60$  at the farthest measured distance from the



mouth, and for the 5 in. duct  $h/R = 18$ .

The experiment did not correspond to the configuration studied by Simon and Clifford in that they treated a point isotropic source at the duct mouth. The distributed source available experimentally at the duct mouth does not alter the results of their analysis. The presence of direct streaming sources in the duct walls, however, is estimated to give rise to a slightly more rapid attenuation than  $1/r^2$ .

If we assume an attenuation of the form  $1/r^n$ , the measurements (Figure 3.16) yield exponents of  $n \approx 2.7$  for the 1-1/2 in. duct and  $n \approx 2.5$  for the 5 in. duct. The large value of the exponent for the 1-1/2 in. duct is surprising, since the thermal albedo contribution from the mouth was estimated from other measurements (see Section IV. B) to be insignificant. In spite of the precautions taken, however, mutual shadowing between foils might have taken place.

#### D. Radial Flux Distributions at the Duct Mouth

We have assumed in the analysis that the flux is flat over the entire duct mouth. Examination of the distributions in Figure 3.11 reveals that this is not entirely correct, but that most of the recovery in the flux occurs close to the walls of the duct. The skewing of the perturbed thermal flux distributions is caused by the asymmetry of the unperturbed radial distribution. In any case, the analytical technique treats only the center of the duct mouth. The degree of accuracy achieved

in applying the analysis to the entire source plane, then, depends upon the extent of collimation utilized in a practical situation. The average perturbed scalar flux over the entire duct mouth is approximately 10 percent higher than the flux minimum at the center.

#### E. Fast Flux Perturbation

In assuming a negligible fast flux perturbation at the duct mouth it was anticipated that even significant changes would affect the thermal flux in only a minor way. It is conceivable that the epithermal region of the spectrum (for example, .625 ev to 5 Kev) could be treated by the analytical method applied to the thermal flux, but no attempt was made to predict duct perturbations in the epithermal region. Epicadmium gold activations, which primarily measure the 4.9 ev flux, indicate a 26 percent scalar flux depression at the mouth of the 5 in. duct. Epicadmium manganese activations, constituting absorption in a 340 ev resonance plus a significant portion of the  $1/v$  portion of the spectrum, indicate a 22 percent scalar flux depression. It is reasonable to assume that the duct perturbation to the higher energy, more nearly monodirectional\* components of the spectrum is smaller. The integrated effect from the point of view of slowing down sources into the thermal region is difficult to

---

\*Figure 4.1 displays angular distributions for the very fast flux (.82 to 10 Mev) derived from an  $S_8$  calculation.

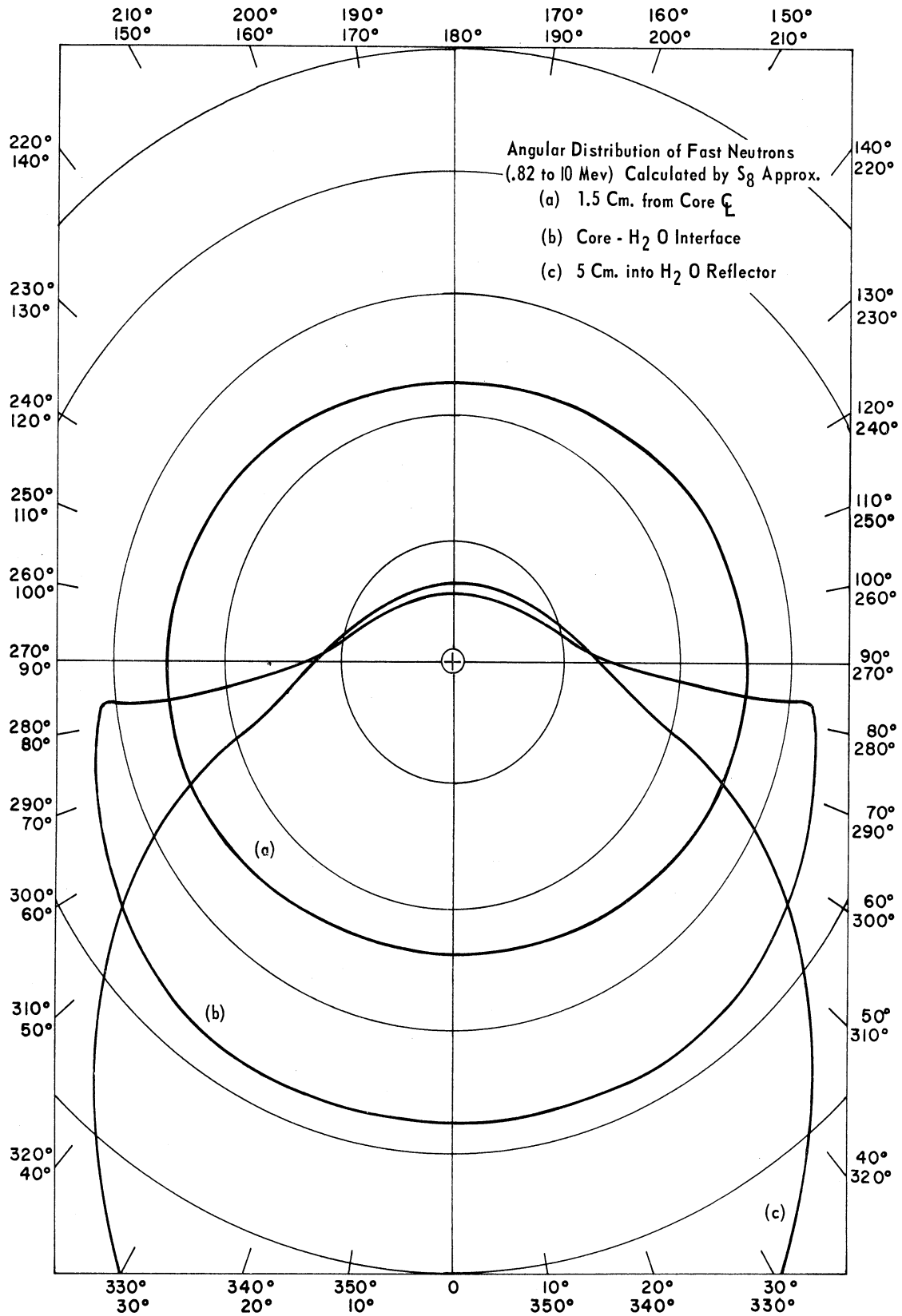


Figure 4.1. Angular distribution of fast neutrons.

evaluate. Figure 4.2 presents the calculated effect of assuming various group 1 (fast) flux depressions at the mouth on the group 2 (thermal) flux for the 5 in. duct. This is computed on the basis of a constant thermal return current to the duct mouth. The results suggest that a 25 percent depression in the integrated fast flux at the duct mouth only leads to a 3 percent depression in the thermal flux.

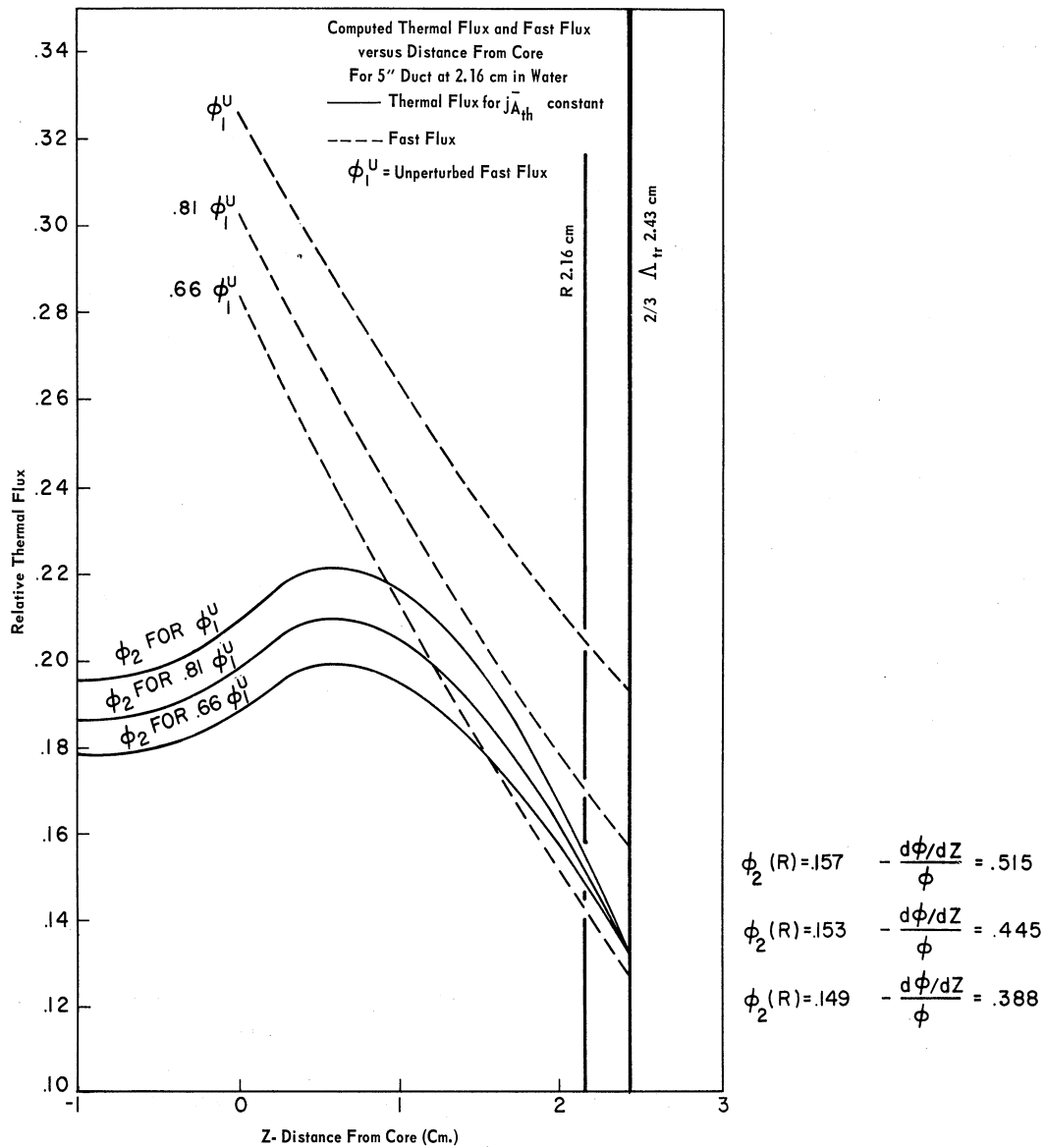


Figure 4.2. Effect on predicted thermal flux of fast flux depression.

The analysis is inapplicable to ducts which appreciably perturb the overall fission source in the multiplying medium. The assumption of small fission source perturbations should, of course, be realized for small ratios of the void area to the core face area, or for voids inserted sufficiently far from the reactor core (i.e., for small reactivity effects). The cross-sectional area of the 5 in. duct in the experimental configuration is of the order of 5 percent of the total area of the reactor face normal to the duct axis. Epicadmium flux measurements along the walls of the 5 in. duct indicate no significant depression in the fast flux. Ducts which appreciably perturb the reactor fission source may be amenable to an iteration analysis involving one and two-dimensional group-diffusion codes.

#### F. Thermal Spectrum

The  $10^{\circ} \pm 5^{\circ}\text{C}$  hardening of the thermal spectrum measured at the mouth of the 5 in. duct is insignificant in the present study (the effect was estimated to lower the average activation cross section of a  $1/v$  detector by less than 2 percent). The fact that a measurable effect was observed, however, suggests that spectral hardening induced by the void may be important in experimental determinations of the neutron spectrum at the exit of a beam port.

Measurements at the Ford Nuclear Reactor using a crystal spectrometer<sup>29</sup> at the exit of the 6 in. beam port sketched in Figure 3.1 determined

a neutron temperature of  $40^\circ \pm 5^\circ\text{C}$ . The temperature of the pool water is  $28^\circ\text{C}$  at a reactor power level of one megawatt. It is reasonable to assume that the 3 in. of graphite and 1-1/2 in. of water between the mouth of the port and the core are sufficient to bring the core neutrons into equilibrium with the diffusing medium. Using the Brown prescription<sup>30</sup> for the hardening effect in water:

$$T_{\text{eff}} = T_0 \left[ 1 + .876 \frac{\sum_a(T_0)}{\sum_{S^\infty}} \right], \quad (4.1)$$

we expect a neutron temperature in the unperturbed medium of less than  $32^\circ\text{C}$ . The difference of  $8^\circ \pm 5^\circ\text{C}$  between the estimated unperturbed neutron temperature and the measured value is presumably due to spectral hardening induced by the port void.

#### G. Scalar Flux at the Duct Mouth

The thermal flux measurements at the center of the 5 in. duct mouth lie approximately 7 percent below the predicted values in both media, as seen in Figures 3.11 and 3.21. Assuming for the moment that the unperturbed flux is a correct representation for the distribution at the duct walls, attenuation by the aluminum walls of the duct, which is difficult to evaluate, in addition to the fast flux depression and hardening of the thermal spectrum, which have been discussed earlier, all act to depress slightly the measured thermal flux at the mouth. The current measurement

at the exit of the collimated duct in water, however, shown in Figure 3.14, agrees well with the predicted value. The arguments presented in Section II.B indicate that in the limit of the infinite half-space ( $j_{A_{th}}^- = 0$ ) P-1 theory affords an adequate prediction for the angular current at the boundary (for  $\mu = -1$ ), but the P-1 scalar flux prediction is 15 percent higher at the boundary than the exact quantity. Since the experimental data conform to this trend (in water  $j_{A_{th}}^-$  is less than 50 percent of the unperturbed return current to the 5 in. duct mouth), it is reasonable to ascribe the discrepancy in the scalar flux to measurable deviations from diffusion theory. Further evidence for deviations from diffusion theory is afforded by the comparison of the measured and predicted gradients at the mouth. In water the measured gradient is 40 percent higher than the predicted value from diffusion theory, and in graphite the measurement is 70 percent higher. Examination of the Milne problem reveals that the exact solution for the gradient possesses a logarithmic infinity at the mouth.

A measurement of  $j_{B_{th}}^+$  was not performed in the complete graphite reflector. However, we infer from the results of the perturbed scalar flux measurements at the duct mouths that the analysis applied to the water medium should be equally valid in graphite. Figure 4.3 is a plot of the prediction for  $j_{B_{th}}^+$  in graphite. It should be pointed out that since the constant cross section approximation used to obtain Eq. (2.25) is not strictly valid here, this equation is not rigorously applicable. The results of a numerical integration of Eq. (2.23), however, agree to within

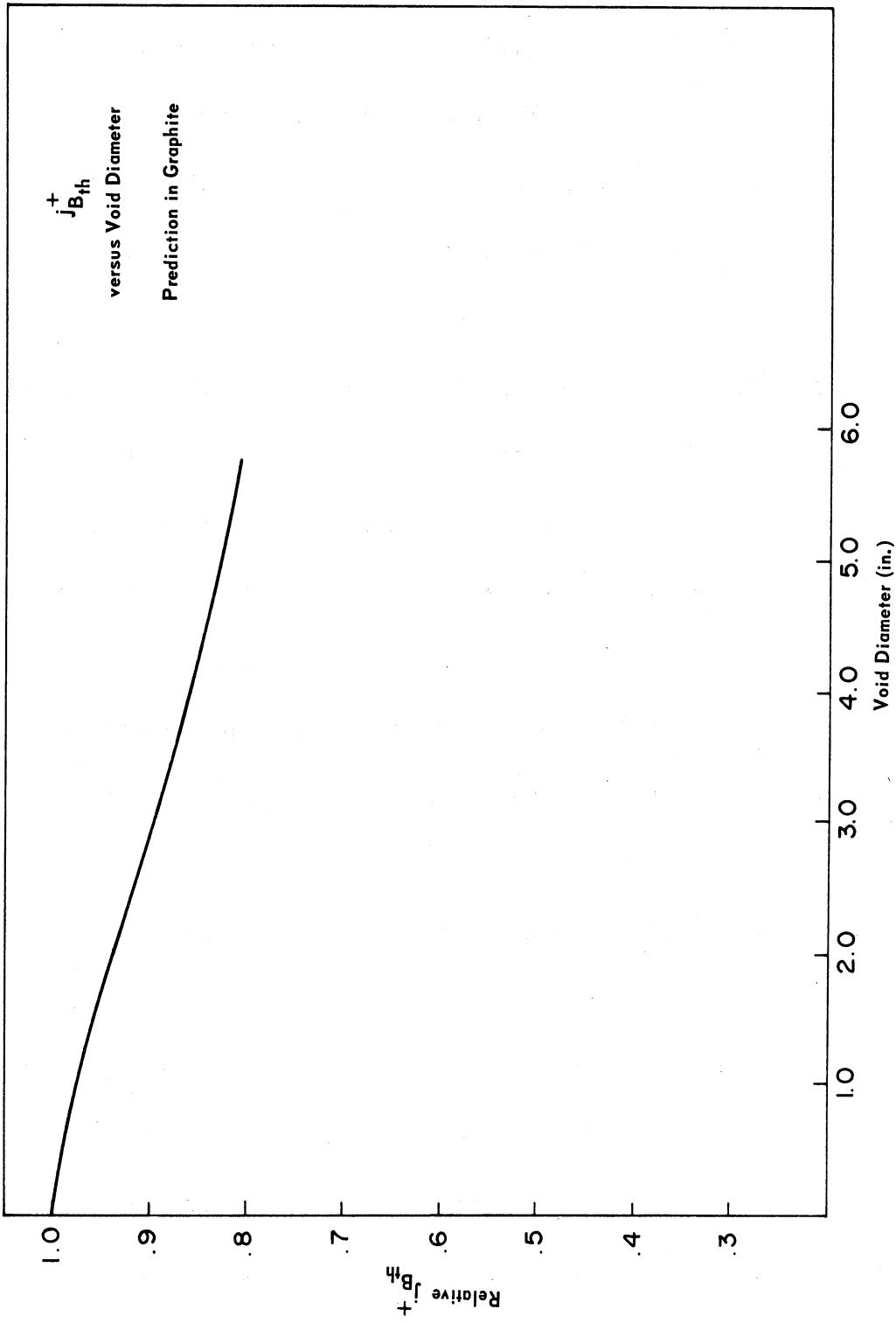


Figure 4.3. Predicted  $j_{B_{th}}^+$  for graphite.



one percent with predictions based upon the constant cross section approximation.

#### H. Scalar Flux Distribution Along the Duct Walls

An idealization of the scalar flux distribution along the duct walls has been incorporated into the framework of the analysis. Predictions within this framework have compared favorably with the experimental results. Nevertheless, it would have been more satisfying to use the realistic flux distribution in Eq. (2.41) to compute the return current. Up to this point, however, an examination of the behavior of the realistic scalar flux distribution along the duct walls has been avoided.

Information concerning the realistic duct wall flux distribution was accessible experimentally. The configuration which gave rise to the largest flux perturbation at the mouth, the 5 in. duct in water, was examined. Foil strips fastened to thin lucite brackets were mounted perpendicular to the duct wall at 1, 3, 5, and 8 cm from the mouth. The relative thermal reaction rates for strips mounted on the east and west sides of the duct are plotted versus radial distance from the duct wall in Figure 4.4. The ratio of the radial component of the gradient at the wall to the scalar flux,  $\frac{\partial\phi/\partial r}{\phi} \Big|_Z^R$ , is recorded by each curve.\*

Figure 4.5 is a plot of the perturbed scalar flux distribution along

---

\*The fact that the gradients are higher on the east side of the duct originates from the asymmetry of the unperturbed radial distribution.

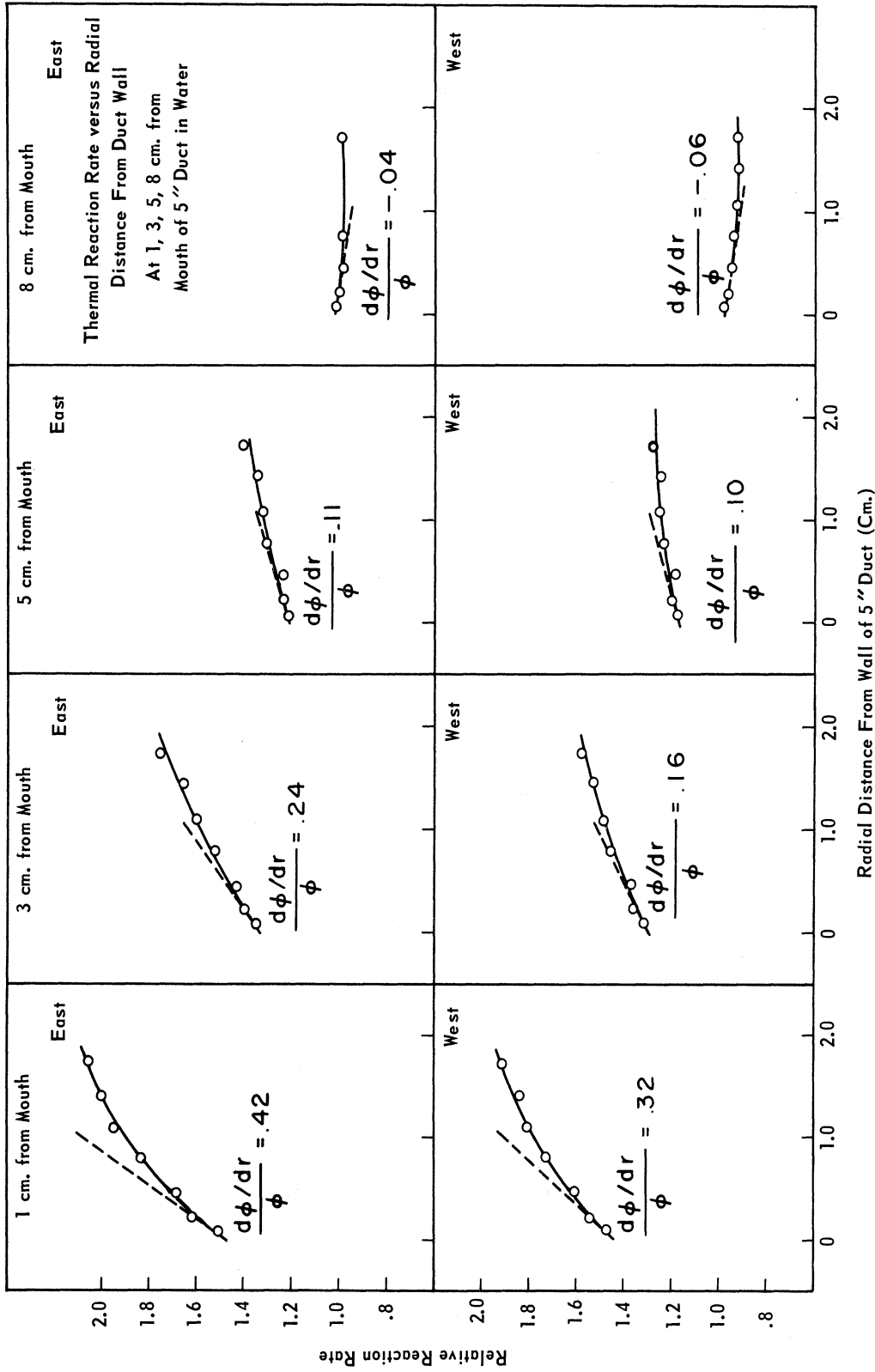


Figure 4.4. Radial thermal flux behavior at four positions along 5-in. duct wall.

the 5 in. duct wall compared with the unperturbed scalar flux distribution in the medium out to 8 cm from the mouth. As anticipated, the scalar flux is initially depressed close to the mouth, but recovers rapidly and eventually exceeds the unperturbed flux where the radial component of the gradient has become negative. Unfortunately, no data were obtained beyond 8 cm. However, assuming for the moment that the perturbed distribution is identical to the unperturbed distribution beyond 7 cm, utilization of the perturbed distribution in the calculation of  $\bar{j}_{A_{th}}$  predicts a value for the duct mouth scalar flux which is 10 percent lower than that obtained from the unperturbed distribution. Since we have concluded earlier that the unperturbed distribution predicts the correct P-1 value of the duct mouth scalar flux, the enhancement of the perturbed distribution beyond 7 cm must compensate for the depression close to the mouth.

An attempt to predict the realistic behavior of the thermal flux distribution along the duct walls was made by the following method. An initial estimate of the quantity  $\frac{\partial\phi/\partial r}{\phi}\Big|_z^R$  was obtained for several discrete axial positions along the duct wall using the unperturbed axial flux distribution in Eq. (2.50) (revised to include the two terms given in expression (2.54) to account for the mouth contribution), the separated form of the current balance relationship. A computer program written to evaluate the initial estimate of  $\frac{\partial\phi/\partial r}{\phi}\Big|_z^R$  is presented in Appendix G. The initial estimate of the relative radial component of the gradient at the mouth,  $\frac{\partial\phi/\partial r}{\phi}\Big|_0^R$ , was obtained in the usual way. The relative gradients

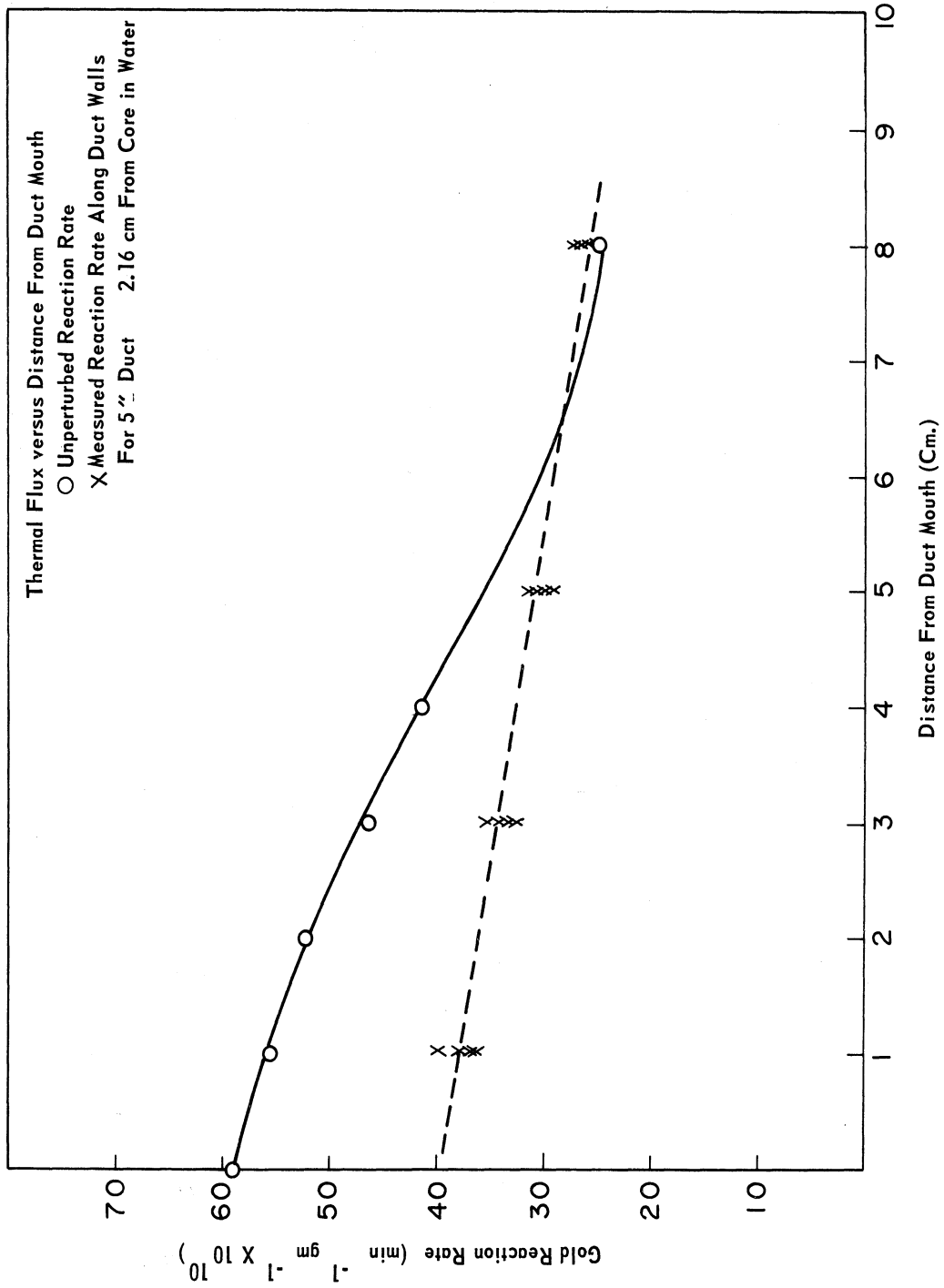


Figure 4.5. Axial thermal flux distribution along walls of 5-in. duct.

were used for a  $z$  varying boundary condition along the water-duct interfaces in a two-dimensional group-diffusion code.\* The cylindrical geometry approximation to the actual configuration is sketched in Figure 4.6. The calculations were performed with two energy groups, and the fast flux was assumed unperturbed.

It was intended that the resulting perturbed flux distribution be used in the unseparated current balance relationship, Eq. (2.45) (revised to include the terms in expression (2.54)), to obtain improved estimates for  $\frac{\partial\phi/\partial r}{\phi}\Big|_R$ . The procedure forms a basis for an iteration technique which was expected to converge rapidly. The initial estimates for  $\frac{\partial\phi/\partial r}{\phi}\Big|_R$ , however, did not permit convergence of the group-diffusion code for the 3 in. or 5 in. ducts. Even when the computation was forced into convergence by diminishing the absolute magnitudes of  $\frac{\partial\phi/\partial r}{\phi}\Big|_R$  far from the mouth, the computed flux distributions were unrealistic, tending to increase with distance from the core. The initial estimates and altered values (to achieve code convergence) of  $\frac{\partial\phi/\partial r}{\phi}\Big|_R$  for the 1-1/2, 3 and 5-in. ducts in water are recorded in Table IV.1. Comparisons with the measured gradients at the walls of the 5 in. duct recorded in Figure 4.4

---

\*The TWENTY GRAND code, described in Appendix B, provides for a logarithmic-derivative or "rod-region" boundary condition, specified by:

$$D^i \frac{d\phi^i}{dr} = -C^i \phi^i$$

for energy group  $i$ .  $C^i$  is supplied as input data for any region specified as a "rod-region."

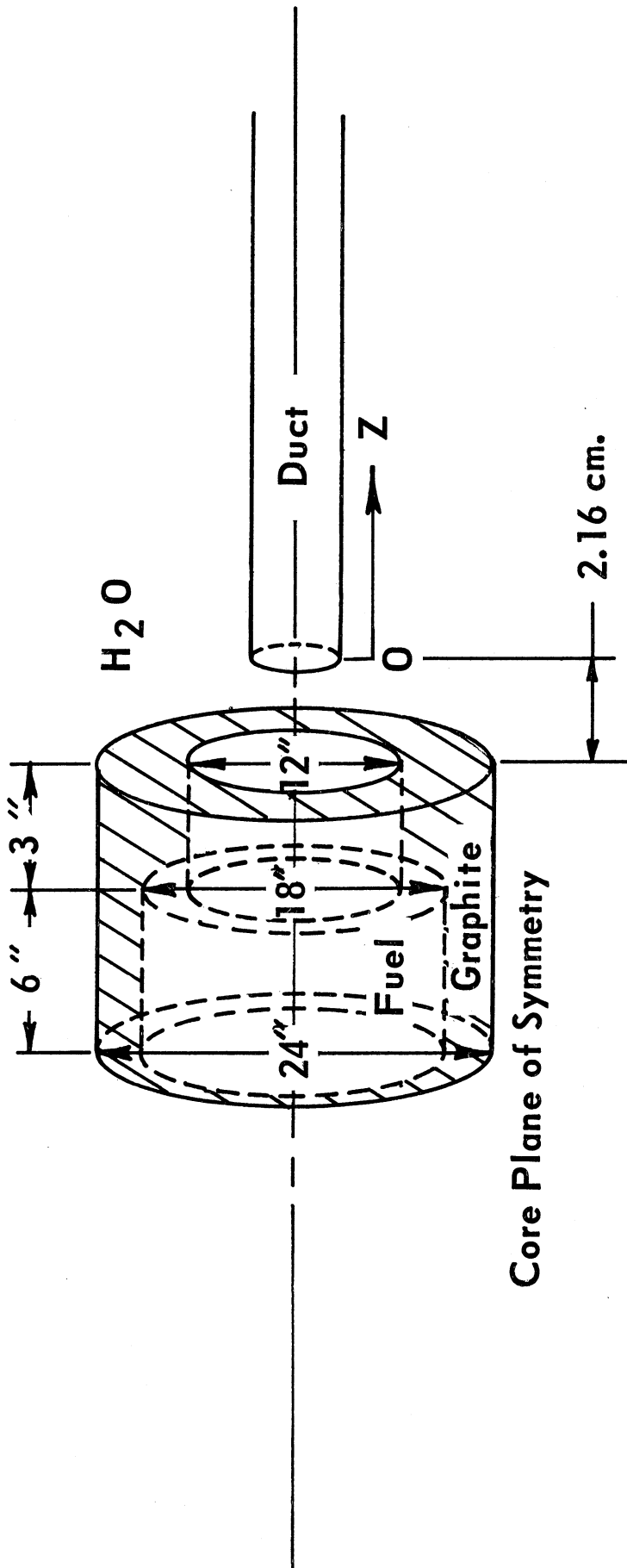


Figure 4.6. Cylindrical geometry approximation to core-duct configuration.

TABLE IV.1

FIRST ESTIMATE OF THE RADIAL COMPONENT OF THE GRADIENTS FOR BOUNDARY  
CONDITION IN TWO-DIMENSIONAL CALCULATION

z Distance from Duct Mouth (cm)	1-1/2 In. Duct		3 In. Duct		5 In. Duct	
	$\frac{\partial\phi/\partial r}{\phi} \Big _z^R$ cm <sup>-1</sup>	Altered $\frac{\partial\phi/\partial r}{\phi} \Big _z^R$ cm <sup>-1</sup>	$\frac{\partial\phi/\partial r}{\phi} \Big _z^R$ cm <sup>-1</sup>	Altered $\frac{\partial\phi/\partial r}{\phi} \Big _z^R$ cm <sup>-1</sup>	$\frac{\partial\phi/\partial r}{\phi} \Big _z^R$ cm <sup>-1</sup>	Altered $\frac{\partial\phi/\partial r}{\phi} \Big _z^R$ cm <sup>-1</sup>
0	.120	Unaltered	.240	.240	.400	.400
1	.150		.340	.340	.547	.547
2	.104		.265	.265	.450	.450
3	.051		.164	.164	.310	.310
4	.000		.057	.057	.149	.149
5	-.047		-.050	-.050	-.020	-.020
6	-.090		-.154	-.154	-.193	-.193
7	-.130		-.254	-.254	-.365	-.365
8	-.165		-.350	-.350	-.536	-.450
9	-.198		-.442	-.396	-.704	-.450
10			-.531	-.396	-.870	-.450
11					-1.033	-.450
12					-1.195	-.450
13					-1.355	-.450
14					-1.516	-.450
15					-1.678	-.450
16					-1.841	-.450
17					-2.006	-.450
18					-2.175	-.450

indicate that the estimated gradients close to the duct mouth are not unreasonable. The apparent deadlock is attributed to the large negative estimates of the gradients far from the duct mouth. Either these values or the treatment of the negative gradients by the code (as a negative absorption in the duct region) is unrealistic.

### I. Reactivity Predictions

A far more encouraging prediction emerges from an examination of the eigenvalues computed by the two-dimensional code. The duct reactivity calculated by using the altered estimates of the duct wall gradients listed in Table IV.1 compare favorably with experiment. This is not surprising, since the fundamental eigenvalue of the diffusion equation is relatively insensitive to the flux distribution. However, inasmuch as the altered gradient estimates for the 5 in. duct provided a highly unrealistic flux distribution, an additional calculation was performed that utilized only the positive gradients ( $\frac{\partial\phi}{\partial r}\Big|_R$  was set equal to zero past 4 cm). Considering the degree of approximation to the realistic geometry, the result of this calculation was also in reasonable agreement with experiment. The reactivity results are presented in Table IV.2.



TABLE IV.2

DUCT REACTIVITY—MEASURED AND PREDICTED  
 DUCTS AT 2.16 CM FROM CORE IN WATER

Duct Diameter (in.)	$\delta k/k$ Measured, %	$\delta k/k$ Predicted using altered $\frac{\partial \phi / \partial r}{\phi} \Big _R$ $z$ , %	$\delta k/k$ Predicted using positive $\frac{\partial \phi / \partial r}{\phi} \Big _R$ $z$ (Zero past 4 cm), %
1-1/2	-.007	-.007	—
3	-.03	-.04	—
5	-.10	-.11	-.16

## V. CONCLUSIONS

The main results of the analysis and measurements discussed in Chapters II, III, and IV may be summarized as follows:

1. P-1 theory can be used to predict adequately the thermal neutron current at the exit of a collimated beam port. The source plane scalar flux can be predicted using P-1 theory with somewhat less accuracy. The method has been applied by computing the return current at the duct source plane in terms of the measured distribution of the unperturbed scalar flux in the reflector. The return current is used in a few-group diffusion calculation in the form of a pseudo boundary condition on the scalar flux. Predicted exit thermal neutron currents for ducts up to 5 in. in diameter in the water reflector at the Ford Nuclear Reactor agree within  $\pm 3$  percent with activation measurements. Predicted source plane scalar fluxes in water and graphite reflectors agree within 7 percent with the measurements.

2. The method can be applied satisfactorily if the calculated distribution of the unperturbed scalar flux in the reflector as obtained from few-group diffusion theory is used to compute the return current. The unperturbed scalar flux distributions in the reflector deviate significantly from the few-group diffusion theory results close to boundaries and far from the reactor core. Predictions for the beam port exit currents obtained from the calculated distributions, however, deviate by only 3 percent from those obtained from the measured distributions.

3. An iteration technique was proposed in an attempt to predict the realistic distributions of the scalar flux along the lateral surfaces of the ducts. Unfortunately, the initial estimates of the radial component of the gradients (obtained by separation of variables) failed to produce convergence of the two-dimensional group-diffusion code. Further work is needed to explore this difficulty.

4. The results of a survey to optimize thermal neutron leakage flux from the Ford Nuclear Reactor clearly indicate that:

- a. The optimum geometry is a slab reactor with the beam port external to the core face normal to the smallest core dimension.
- b. An increase in power density by improved reflection is more desirable than an increase in integrated power because of a reduction in the ratio of fast to thermal flux.
- c.  $D_2O$  is the most effective reflector material for this purpose.

## APPENDIX A

### A SURVEY FOR THE ENHANCEMENT OF THERMAL NEUTRON LEAKAGE FLUX

#### 1. Introduction

This survey is directed toward an optimization of the thermal neutron flux intensity and the neutron spectrum in a reflector region of the Ford Nuclear Reactor (FNR) for beam port applications. The FNR was briefly described in Chapter III. Although the results of the investigation pertain to a swimming pool reactor facility of the FNR type, they should apply at least qualitatively to a more general type of thermal reactor.

For purposes of efficiency, as well as compliance with economic and physical limitations at the existent reactor facility, the following constraints were established:

- (a) The core composition was held constant. For this the FNR regular fuel element was adopted (partial elements and poison rods were disregarded).
- (b) The integrated reactor power was held constant.
- (c) The vertical core dimension was fixed at 24 in., the height of the "meat" portion of the FNR fuel element.
- (d) The beam port was aligned with a radius of the core outside of the fuel region.

- (e) The beam port influence on the exit current was neglected in this phase of the study.

In keeping with these constraints, the survey considers variations in reflector materials and core-reflector configurations.

The computer codes utilized for the numerical computations are described in Appendix B. Compositions and group constants are tabulated in Appendix C. Four-group diffusion theory was adopted. The four-group scheme, with breakpoints listed in Appendix C, has been highly successful in treating small, enriched, light-water reactors.<sup>31</sup> Moreover, a four-group study affords some useful information concerning the neutron spectrum.

## 2. Three-Dimensional Simulation

Three-dimensional group-diffusion calculations would be prohibitively time-consuming for an inquiry of this nature. Two-dimensional calculations were performed whenever possible, but they were limited in usefulness, since criticality search routines were not included. Therefore, most of the computations were performed using one-dimensional simulation of the three-dimensional geometry. This was accomplished by holding two of the dimensions,  $y$  and  $z$ , constant and searching for the critical size and flux distribution in a variable third dimension,  $x$ . Leakage in the  $y$  and  $z$  directions was incorporated as a transverse buckling.

The transverse buckling was obtained in the following manner. One-dimensional flux distributions in the y and z directions were acquired for each of the four groups for constant y and z dimensions (leakage in the x direction was accounted for by allowing the code to search for the critical transverse buckling). Then for each group the bucklings transverse to the x direction were derived from the following relationships:

$$\langle (B_y^2) \rangle^i = \frac{- \int_{\text{core}} \nabla^2 \phi^i(y) dy}{\int_{\text{core}} \phi^i(y) dy} , \quad (\text{A.1})$$

and:

$$\langle (B_z^2) \rangle^i = \frac{- \int_{\text{core}} \nabla^2 \phi^i(z) dz}{\int_{\text{core}} \phi^i(z) dz} . \quad (\text{A.2})$$

Transverse buckling components which were used in the acquisition of the subsequent results are listed in Table A.I.\* The total buckling transverse to the x-direction for the ith group is given by:

$$\langle (B_t^2)_{T_x} \rangle^i = \langle (B_y^2) \rangle^i + \langle (B_z^2) \rangle^i . \quad (\text{A.3})$$

---

\*Transverse bucklings obtained for the core were used in all regions. Refinements to some of the subsequent results could be achieved by using region-dependent as well as group-dependent bucklings.

TABLE A. I

## TRANSVERSE BUCKLINGS

(cm<sup>-2</sup>)

	Cold-Clean Core			Equil. Xe, 8.4% BU Core				
	(B <sub>1</sub> ) <sup>2</sup> T	(B <sub>2</sub> ) <sup>2</sup> T	(B <sub>3</sub> ) <sup>2</sup> T	(B <sub>4</sub> ) <sup>2</sup> T	(B <sub>1</sub> ) <sup>2</sup> T	(B <sub>2</sub> ) <sup>2</sup> T	(B <sub>3</sub> ) <sup>2</sup> T	(B <sub>4</sub> ) <sup>2</sup> T
Vertical	.00296	.00253	.00153	-.00472	.00298	.00253	.00156	-.00448
3 Rows Horiz.	.00933	.00493	.00499	-.00026	---	---	---	---
Total	.01229	.00746	.00652	-.00498	---	---	---	---
4 Rows Horiz.	.00635	.00337	.00341	-.000202	.00651	.00346	.00348	-.000057
Total	.00931	.00590	.00494	-.00492	.00949	.00599	.00504	-.00454
5 Rows Horiz.	.00464	.00248	.00252	-.00016	.00475	.00254	.00255	-.000042
Total	.00760	.00501	.00405	-.00488	.00773	.00507	.00411	-.00452
7 Rows Horiz.	.00283	.00152	.00155	-.000117	.00289	.00155	.00156	-.000035
Total	.00579	.00405	.00308	-.00484	.00587	.00408	.00312	-.00451
8 Rows Horiz.	---	---	---	---	.00235	.00126	.00127	-.000032
Total	---	---	---	---	.00533	.00379	.00283	-.00451

## 3. Streaming Flux

The scalar flux distributions, which together with the fundamental eigenvalue constitute the principal output of the group-diffusion codes, are not the quantities of foremost interest from the point of view of the present study. Rather, we are interested in the angular flux at the source plane in the direction of the beam port exit. The angular flux is given by Eq. (2.23) in the constant cross section approximation. If the constant cross section restriction is removed:

$$\phi(\bar{r}, \bar{\Omega}) = \frac{1}{4\pi} \int_0^\infty d\eta [\Sigma_s(\bar{r}-\eta\bar{\Omega})\phi_0(\bar{r}-\eta\bar{\Omega}) + s(\bar{r}-\eta\bar{\Omega})] e^{-\int_0^\eta \Sigma_t(\bar{r}-\eta'\bar{\Omega}) d\eta'}. \quad (\text{A.4})$$

$s(\bar{r}-\eta\bar{\Omega})$  is defined here as the source integrated over all angles.

For long ports,  $(h/R) \gg 1$ , it is the forward flux, close to  $\mu = -1$ , which is detected at the exit. In the limit of a collimated port of infinite length, Eq. (A.4) can be approximated by the one-dimensional integration:

$$\phi(x, \mu=-1) \approx \frac{1}{4\pi} \int_0^\infty dx' [\Sigma_s(x-x')\phi_0(x-x') + s(x-x')] e^{-\int_0^{x'} \Sigma_t(x-x'') dx''}. \quad (\text{A.5})$$

Then for any position  $x$  in the reflector and energy group  $i$ , we define the streaming flux:



$$\mathcal{J}^i(x) = \int_0^{\infty} dx' [\Sigma_s^i(x-x') \phi_0^i(x-x') + s^i(x-x')] e^{-\int_0^{x'} \Sigma_t^i(x-x'') dx''} \quad (A.6)$$

The streaming flux is emphasized in the subsequent presentation of results. Since beam port perturbations were neglected in this survey, the unperturbed scalar flux and source distributions were used to compute this quantity. Slowing down sources were neglected. Subroutine STREAM, written to compute  $\mathcal{J}^i(x)$  and the partial current,  $j_i^+(x)$ , in conjunction with the FOG code, is listed together with the revised main program of FOG in Section A.7.

#### 4. Configurational Effects

##### BARE REACTOR EXAMINATION

In addition to allowing a simple analysis, the bare reactor exhibits fast neutron leakage behavior which is similar to that of the reflected core. Examination of the behavior of fast neutron leakage should provide considerable insight into the influence of the reactor configuration on the thermal neutron flux intensity in a reflected system, inasmuch as the removal of fast neutrons constitutes a thermal neutron source in the reflector.

The flux in a bare homogeneous reactor satisfies the Helmholtz equation:

$$\nabla^2 \phi + B_g^2 \phi = 0 . \quad (\text{A.7})$$

The total leakage is given by:

$$- \int D(\bar{r}) \nabla^2 \phi(\bar{r}) d^3 r = B_g^2 \int D(\bar{r}) \phi(\bar{r}) d^3 r , \quad (\text{A.8})$$

and the integrated power may be expressed as:

$$\text{Power} = \text{const.} \int \Sigma_f(\bar{r}) \phi(\bar{r}) d^3 r . \quad (\text{A.9})$$

For a fixed integrated power and spatially independent properties:

$$\text{Total Leakage} \sim B_g^2 . \quad (\text{A.10})$$

A critical bare reactor, however, must satisfy the condition:

$$k_{\text{eff}} = 1 = \frac{k_{\infty} e^{-B_m^2 \tau}}{1 + L^2 B_m^2} . \quad (\text{A.11})$$

The material buckling,  $B_m^2$ , is a function only of the reactor material composition, and for a critical system it must be equal to the smallest eigenvalue, the geometrical buckling, of Eq. (A.7). Thus:

$$\text{Total Leakage} \sim B_g^2 = B_m^2 , \quad (\text{A.12})$$

which is a constant for a critical bare reactor of homogeneous composition operating at a fixed power level, regardless of the core geometry.

The average leakage per unit area, however, is a function of the

total surface area of the core. The minimum critical volume and surface area for bare reactors of three geometries<sup>13</sup> are listed in Table A.II.

TABLE A.II

CRITICAL VOLUME, AREA, AND RELATIVE LEAKAGE  
FOR BARE REACTORS OF THREE GEOMETRIES

Geometry	Minimum Critical Volume	Critical Surface Area	Relative Average Leakage/Area
Sphere	$130/B^3$	$125/B^2$	1.0
Finite Cylinder	$148/B^3$	$155/B^2$	.806
Rectangular Parallelepiped	$161/B^3$	$179/B^2$	.698

The fourth column of the table does not express the complete story, however. The leakage is strongly peaked at the center of a face of the parallelepiped, whereas it is uniform over the entire surface of the sphere. Using Gauss's theorem, the total leakage from the reactor can be expressed as:

$$-D \int_{\text{vol.}} d^3r \nabla^2 \phi(\bar{r}) = -D \int_{\text{surf.}} dS \hat{n} \cdot \nabla \phi \Big|_{\bar{r} = \bar{R}} \quad (\text{A.13})$$

The flux distribution in a bare cube of linear dimension  $c$  is given by (assume the reactor is large enough so that  $c \approx c+d$ ):

$$\phi(x,y,z) = A \cos \frac{\pi x}{c} \cos \frac{\pi y}{c} \cos \frac{\pi z}{c} . \quad (\text{A.14})$$

The average leakage per unit area is given by:

$$-\frac{D}{c^2} \int_{-c/2}^{c/2} dy \int_{-c/2}^{c/2} dz \left. \frac{\partial}{\partial x} \phi(x,y,z) \right|_{x=c/2} = \frac{4DA}{\pi c} , \quad (\text{A.15})$$

whereas the peak leakage per unit area occurs at the center of the face, and is equal to:

$$-D \hat{n} \cdot \bar{\nabla} \phi(\bar{r}) \Big|_{\bar{r} = \bar{R}} = -D \left. \frac{\partial}{\partial x} \phi(x,y,z) \right|_{\substack{y=0 \\ z=0 \\ x=c/2}} = \frac{DA\pi}{c} . \quad (\text{A.16})$$

Thus for a cube,  $\frac{\text{Peak Leakage/area}}{\text{Average Leakage/area}} = 2.46$ , and

$\frac{\text{Peak Leakage/area for a cube}}{\text{Average leakage/area for a sphere}} = 1.72$ . This result indicates that

the bare parallelepiped possesses an advantage over the more efficient reactor geometry from the point of view of maximum leakage.

Now let us estimate the effect of varying two of the dimensions of a rectangular parallelepiped, holding the third dimension constant. We designate the fixed dimension by  $c$ , and the variable dimensions by  $a$  and  $b$ . For a bare critical parallelepiped operating at constant power, the geometrical buckling is given by:

$$B_g^2 = \left(\frac{\pi}{a}\right)^2 + \left(\frac{\pi}{b}\right)^2 + \left(\frac{\pi}{c}\right)^2 = \text{constant} = 3 \left(\frac{\pi}{c}\right)^2 , \quad (\text{A.17})$$

which is the buckling for a cube. The total leakage from one face of the reactor is expressed by:

$$-D \int_{-c/2}^{c/2} dz \int_{-b/2}^{b/2} dy \left. \frac{\partial \phi(x,y,z)}{\partial x} \right|_{x=a/2} = \frac{4DA}{\pi} \left( \frac{bc}{a} \right) \quad . \quad (\text{A.18})$$

Using Eq. (A.17), we obtain for the leakage out of a face normal to dimension a:

$$\text{Leakage} = \frac{4DAc}{\pi} \frac{1}{\left( \frac{2a^2}{c^2} - 1 \right)^{1/2}} , \quad \frac{a}{c} > .707 \quad . \quad (\text{A.19})$$

Dividing by the area of the face, the average leakage/area is given by:

$$\frac{\text{Average Leakage}}{\text{Area}} = \frac{4DA}{\pi c} \frac{1}{(a/c)} \quad . \quad (\text{A.20})$$

Table A.III is a list of the total leakage and average leakage per unit area (normalized to unity for a cube) from a face of the parallelepiped normal to dimension a.

TABLE A.III

RELATIVE LEAKAGE FROM A FACE FOR BARE  
PARALLELEPIPEDS OF VARIOUS SHAPES

a/c	Total Leakage	Leakage/Area
.8	1.89	1.25
.9	1.27	1.11
1.0	1.00	1.00
1.1	.84	.909
1.2	.73	.834

Beam extraction from a face which is normal to the slender core dimension is suggested.

#### THE WATER REFLECTED PARALLELEPIPED

One group of neutrons is insufficient to study the reflected parallelepiped, thus it is convenient to solve the four-group equations on the computer. The configurations examined are shown in Figure A.1. Reactor cores with 3, 4, 5, and 7 transverse elements were considered. The critical x dimensions recorded in Figure A.1 were obtained from dimension searches using the three-dimensional simulation technique discussed earlier. The fuel (cold-clean composition) was surrounded by light water except for symmetric rows of graphite normal to the y-axis. Figures A.2-A.5 display the x-axis scalar flux and streaming flux distributions. Three of the four computed groups are presented in these and subsequent plots.

Table A.IV is a list of pertinent information from Figures A.2-A.5.

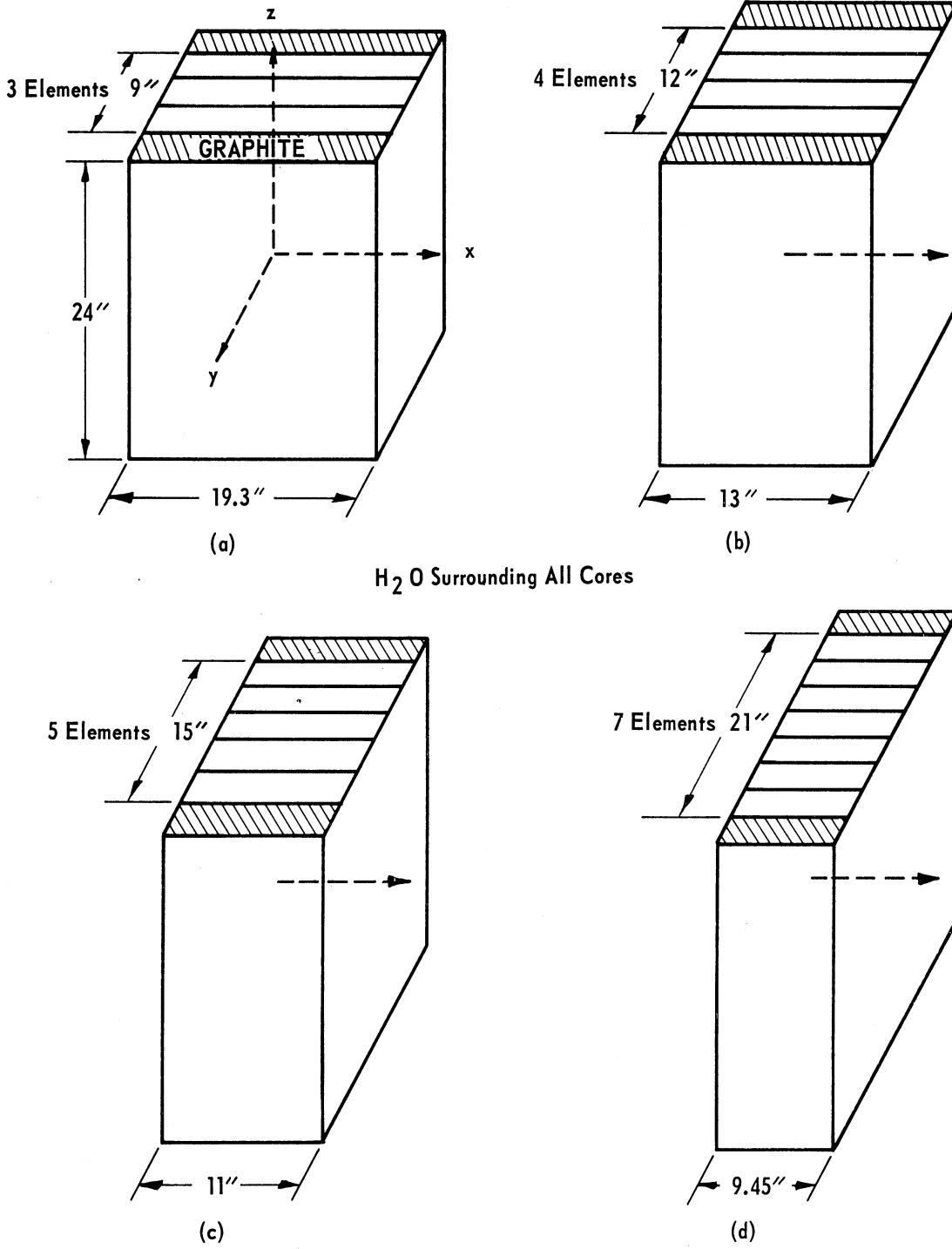


Figure A.1. Core geometries for H<sub>2</sub>O reflected configuration studies (cold-clean fuel).

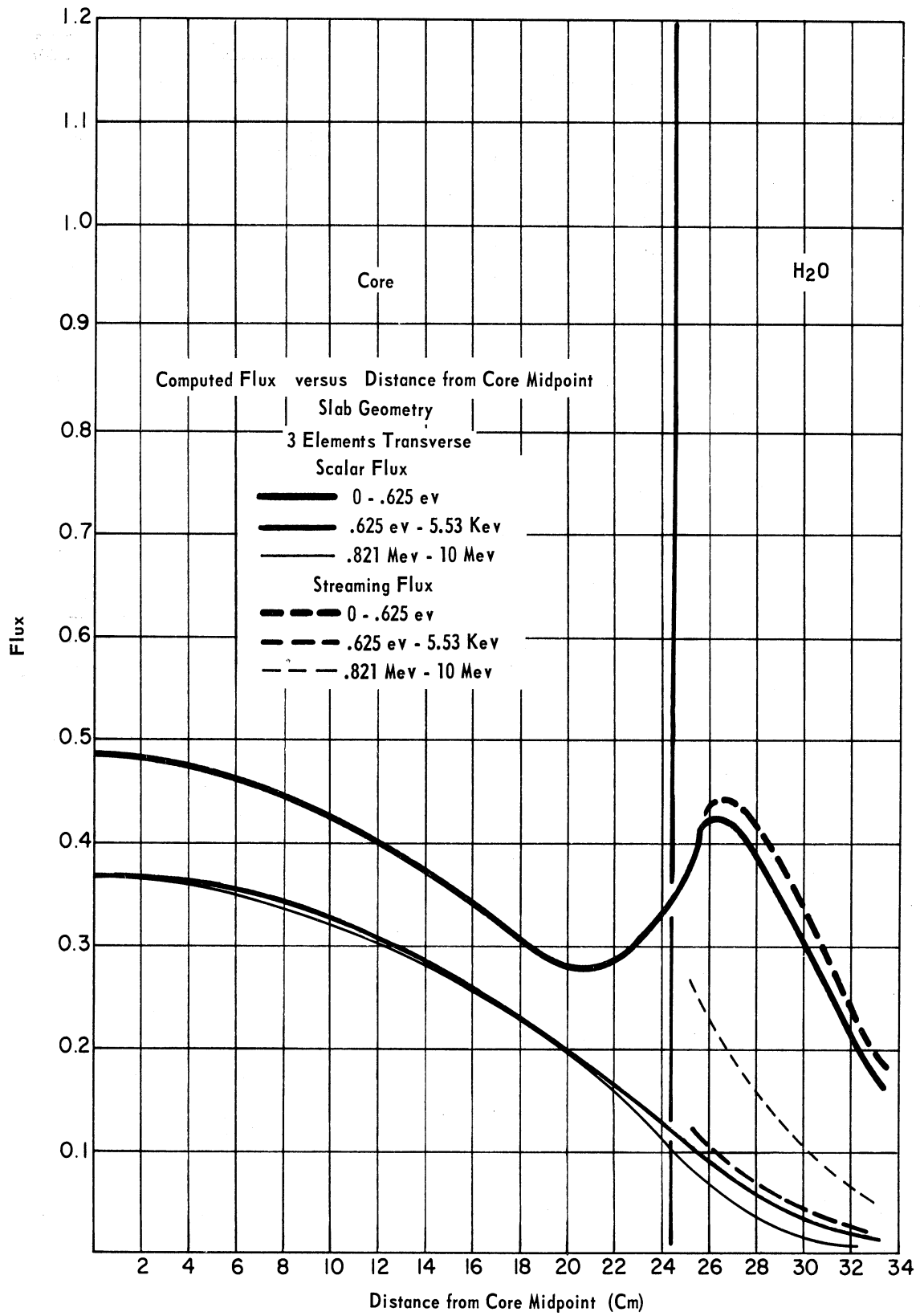


Figure A.2. Computed flux distributions; H<sub>2</sub>O reflected core; 3 elements transverse.



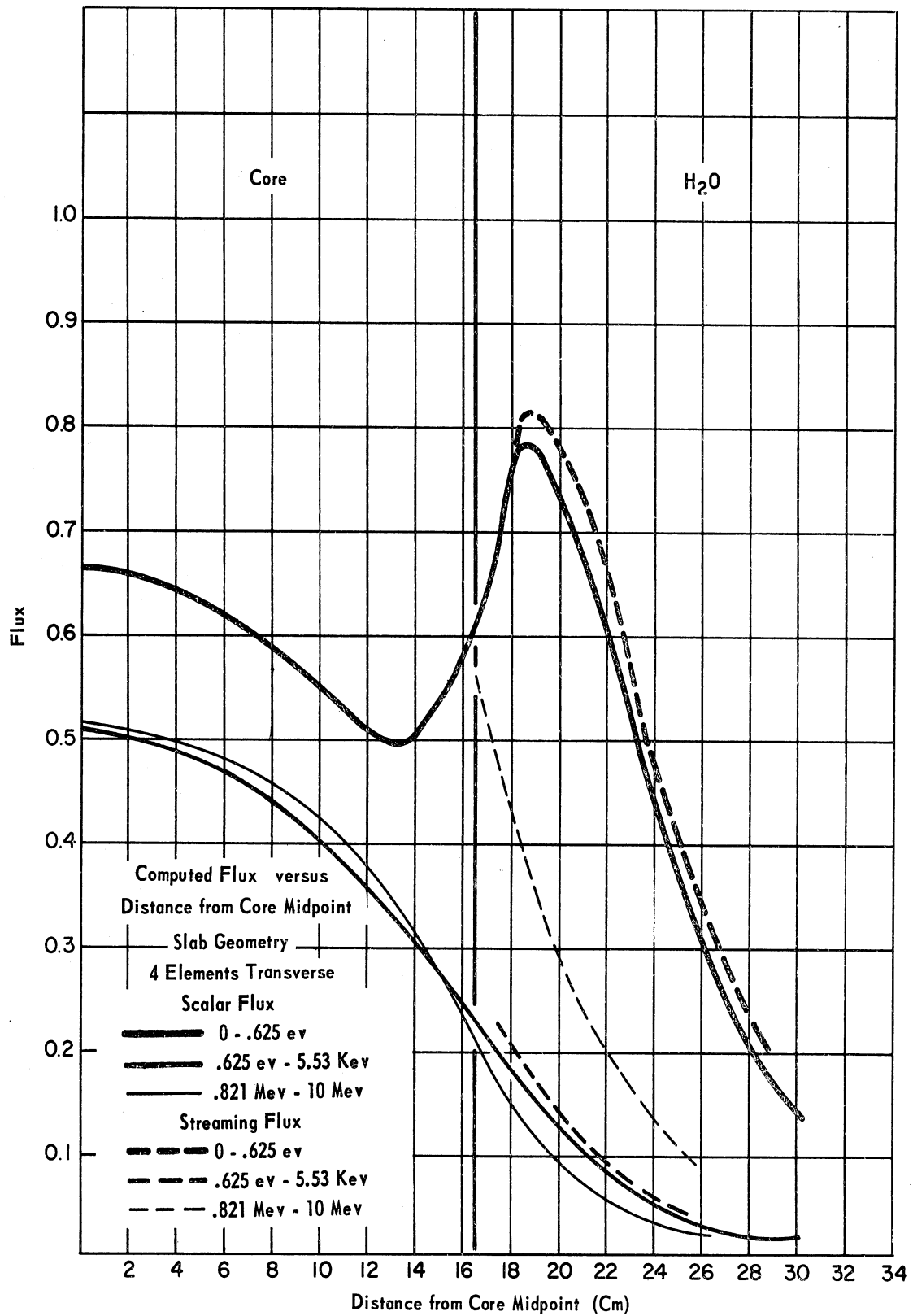


Figure A.3. Computed flux distributions; H<sub>2</sub>O reflected core; 4 elements transverse.

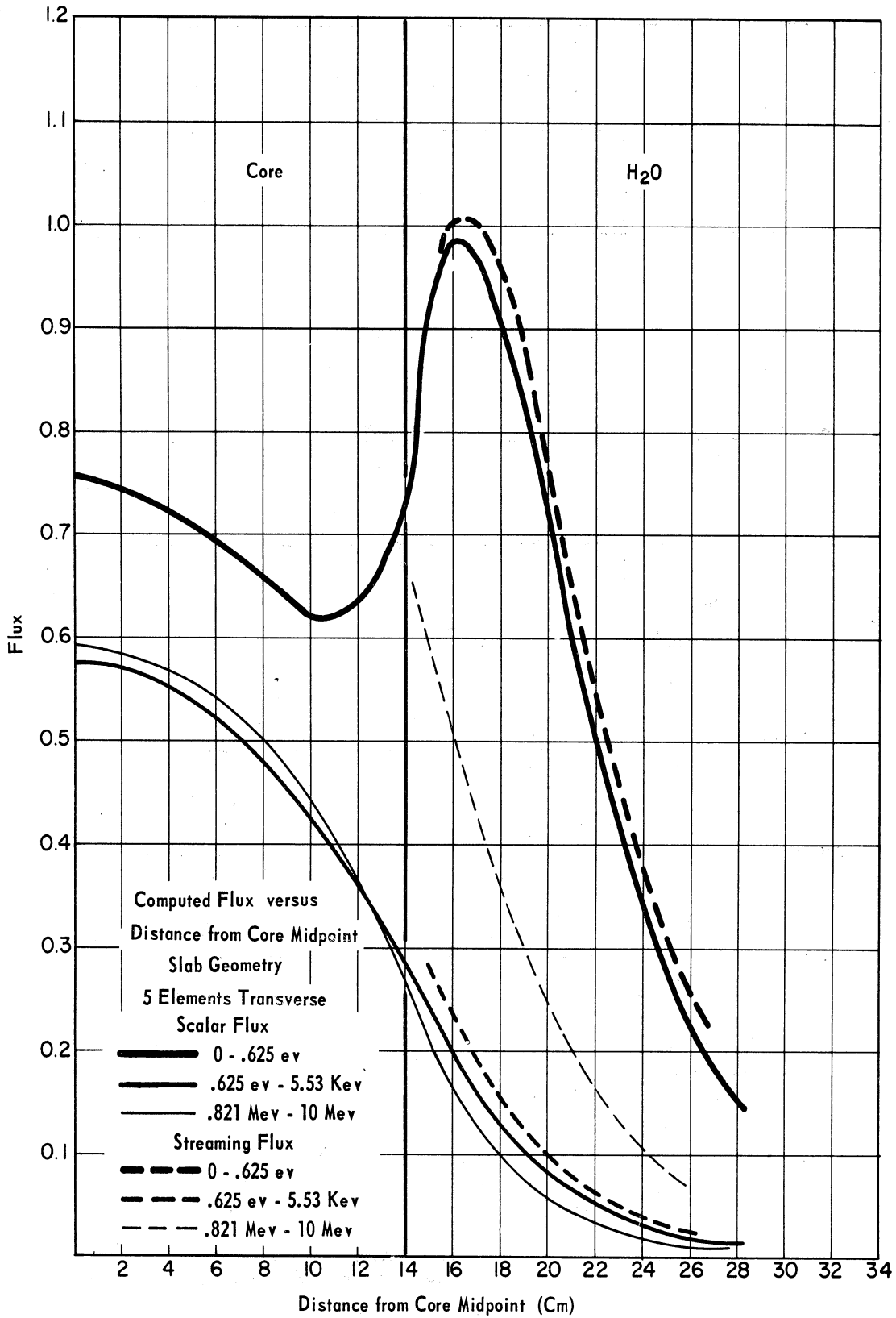


Figure A.4. Computed flux distributions; H<sub>2</sub>O reflected core; 5 elements transverse.

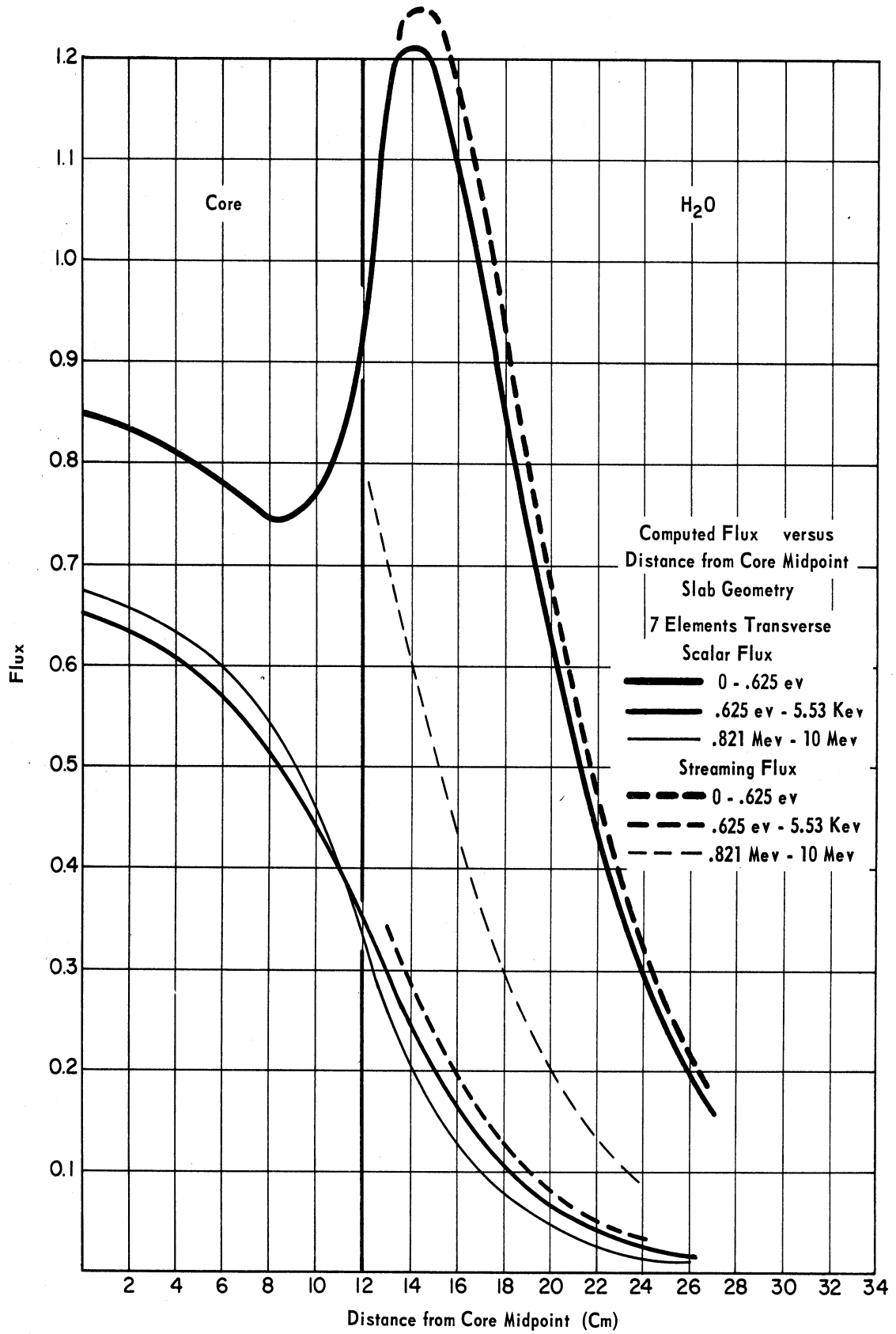


Figure A.5. Computed flux distributions; H<sub>2</sub>O reflected core; 7 elements transverse.

TABLE A.IV  
 COLD-CLEAN H<sub>2</sub>O REFLECTED PARALLELEPIPED CORES OF  
 VARIOUS SHAPES

	$S_{\max}^4$	$(S^4-S^3)_{\max}$	$(S^4-S^1)_{\max}$	$(S^3/S_{\max}^4)$	$(S^1/S_{\max}^4)$	$1/V$ in. <sup>-3</sup>
3 Elem. Trans. Cold-Clean Core	.448	.358	.256	.202	.467	.00024
4 Elem. Trans. Cold-Clean Core	.811	.647	.478	.202	.434	.00027
5 Elem. Trans. Cold-Clean Core	1.06	.794	.599	.180	.388	.00025
7 Elem. Trans. Cold-Clean Core	1.25	.990	.755	.208	.432	.00021
7 Elem. Trans. Eq. Xe- 8.4% BU Core	.965	.770	.596	.215	.422	.00016

The quantities chosen here and in the subsequent studies to be of major interest are: (i) the maximum value of the thermal streaming flux,  $J_{\max}^4$ ; (ii) the maximum difference between the thermal and epithermal and the thermal and fast streaming fluxes,  $(J^4 - J^3)_{\max}$  and  $(J^4 - J^1)_{\max}$ ; (iii) the ratio of epithermal to thermal and fast to thermal streaming fluxes at the location of the maximum thermal streaming flux,  $(J^3 / J_{\max}^4)$  and  $(J^1 / J_{\max}^4)$ ; (iv) the inverse volume of the core,  $1/V$ , a measure of the average power density of the reactor. An additional listing in Table A.IV

compares the cold-clean, seven-element transverse core with a core containing equilibrium Xe and 8.4 percent fuel burnup.

Table A.IV strongly suggests beam extraction adjacent to a face which is normal to a slender dimension of the core. Quantitative justification is presented for deforming the core to the optimum configuration (maximum power density), and going past this point if possible.

#### LOCALIZED CORE ALTERATIONS

It was of interest to examine the effects of an uneven fuel distribution. Figure A.6 presents the results of a calculation comparing the leakage flux of a core with clean fuel in the center and 8.4 percent fuel burnup on the outside with that of a core endowed with the converse loading. In the latter core the clean and burned-up fuels were loaded in approximately even proportions, while in the former core the clean fuel was moved to the central zone while enough burned-up fuel was loaded on the circumference to maintain criticality. The calculation was accomplished in cylindrical geometry, and the burned-up composition is that listed in Table C.I (minus the xenon). The slightly reduced size of the configuration with the clean fuel in the center gives rise to higher thermal streaming flux in the reflector; however, the increase is only 5 percent.

Localized fuel additions in the vicinity of a beam port would merely act to depress the thermal flux while increasing the fast flux. The effect of small water gaps at the center of the core was explored, but

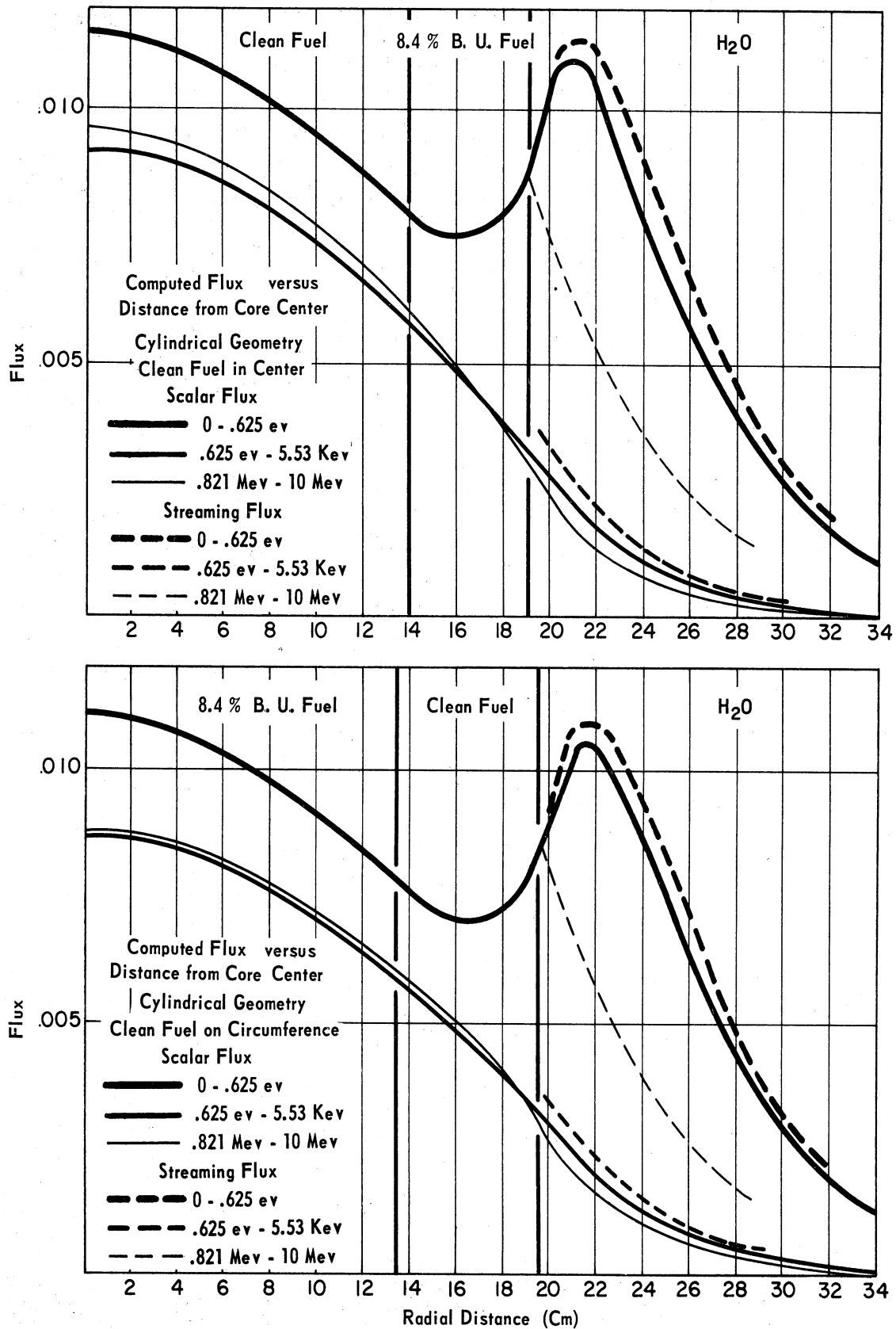


Figure A.6. Computed flux distributions; comparison of depleted fuel in center and on circumference of core.

yielded no net improvement. (A 3 in. gap, while giving rise to a 250 percent local flux peak, would increase the fuel loading by 12 percent, and decrease the reflector thermal flux by 14 percent.)

## 5. The Effect of Reflector Materials

### NEARLY INFINITE REFLECTORS IN CYLINDRICAL GEOMETRY

The initial examination of reflector materials was carried out in cylindrical geometry for a cold-clean core composition. The core was surrounded by a thickness of at least one migration length of each material to achieve the effect of a nearly infinite reflector. Group independent transverse bucklings were used for simplicity.\* The results of the computations are plotted in Figures A.7-A.12. Results for H<sub>2</sub>O, graphite, BeO, D<sub>2</sub>O, and combinations of graphite and H<sub>2</sub>O are presented. BeO results are presented because the calculations indicated that this material is at least as effective as pure Be.

Table A.V, composed of significant information from Figures A.7-A.12, points to the near linear dependence of the thermal streaming flux on the average reactor power density (tabulated as the inverse core volume). BeO, clearly the best reflector, increases the thermal streaming flux by a factor of 3.2 while raising the average power density by a factor of

---

\* $B_{T1}^2 = .00165 \text{ cm}^{-2}$  was adopted here for the core and  $B_{T2}^2 = .00125 \text{ cm}^{-2}$  for the reflector. These numbers were obtained from epicalcium flux traverses in the FNR.<sup>17</sup>

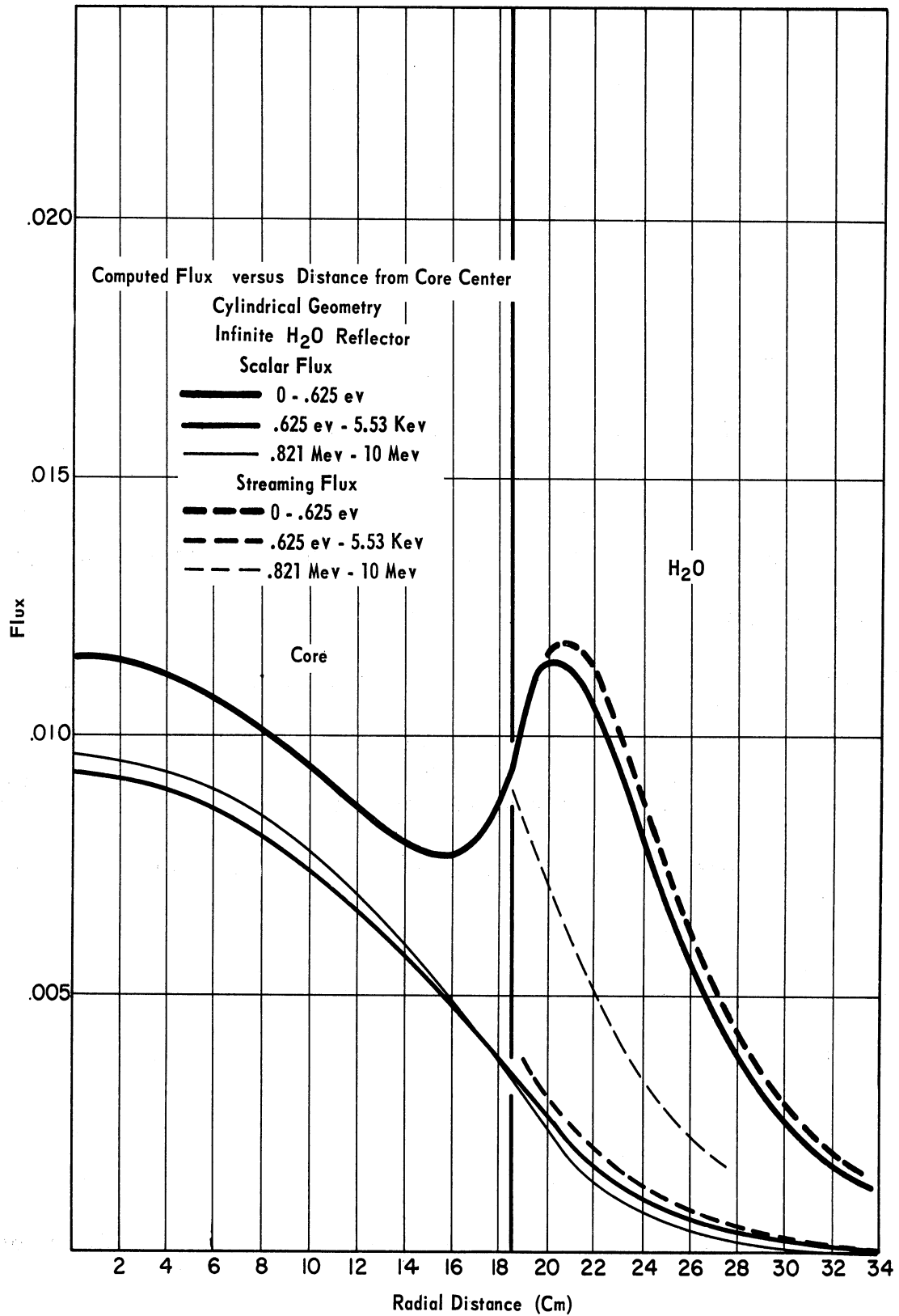


Figure A.7. Computed flux distributions; infinite H<sub>2</sub>O reflector; cylindrical geometry.



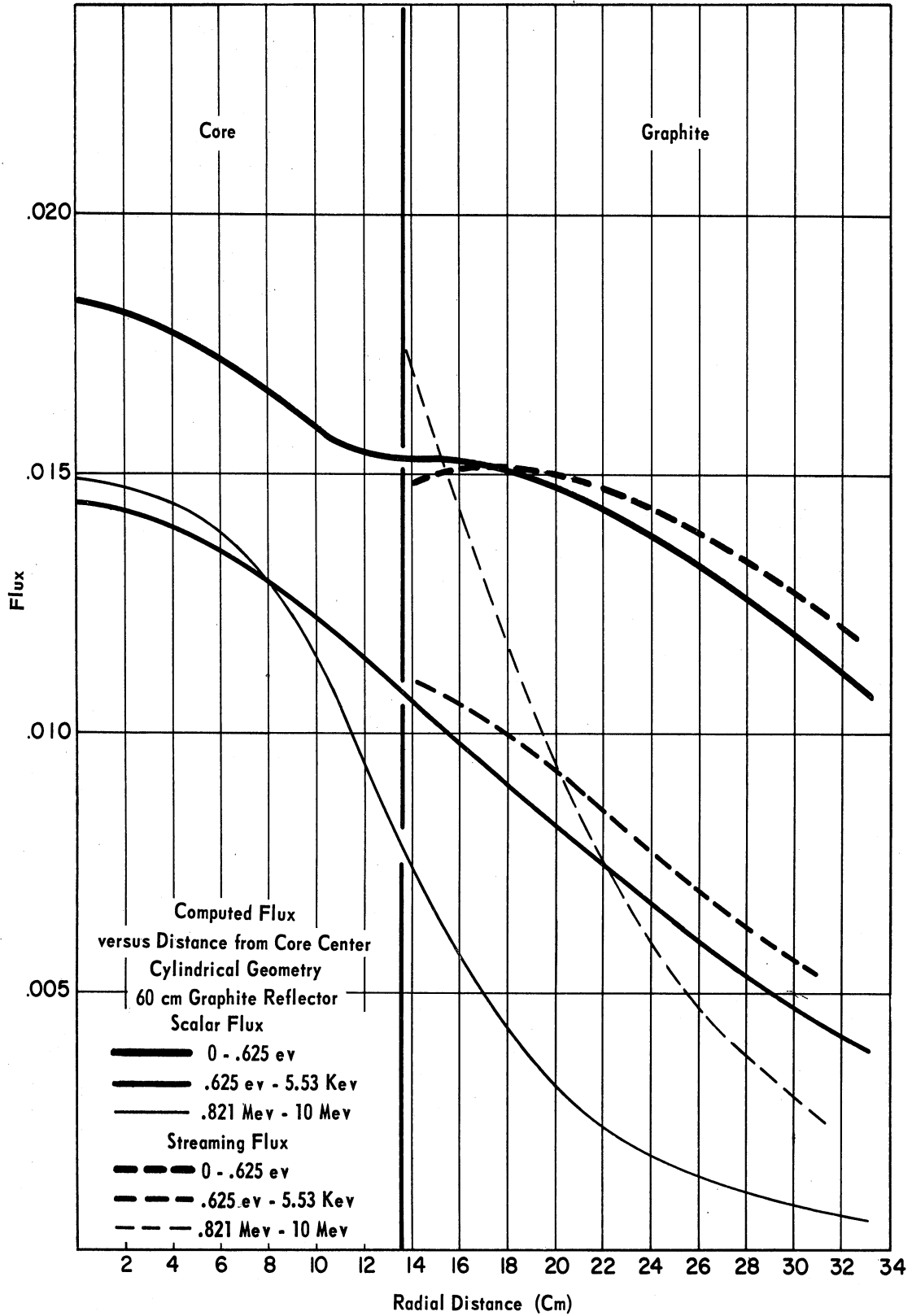


Figure A.8. Computed flux distributions; infinite graphite reflector; cylindrical geometry.

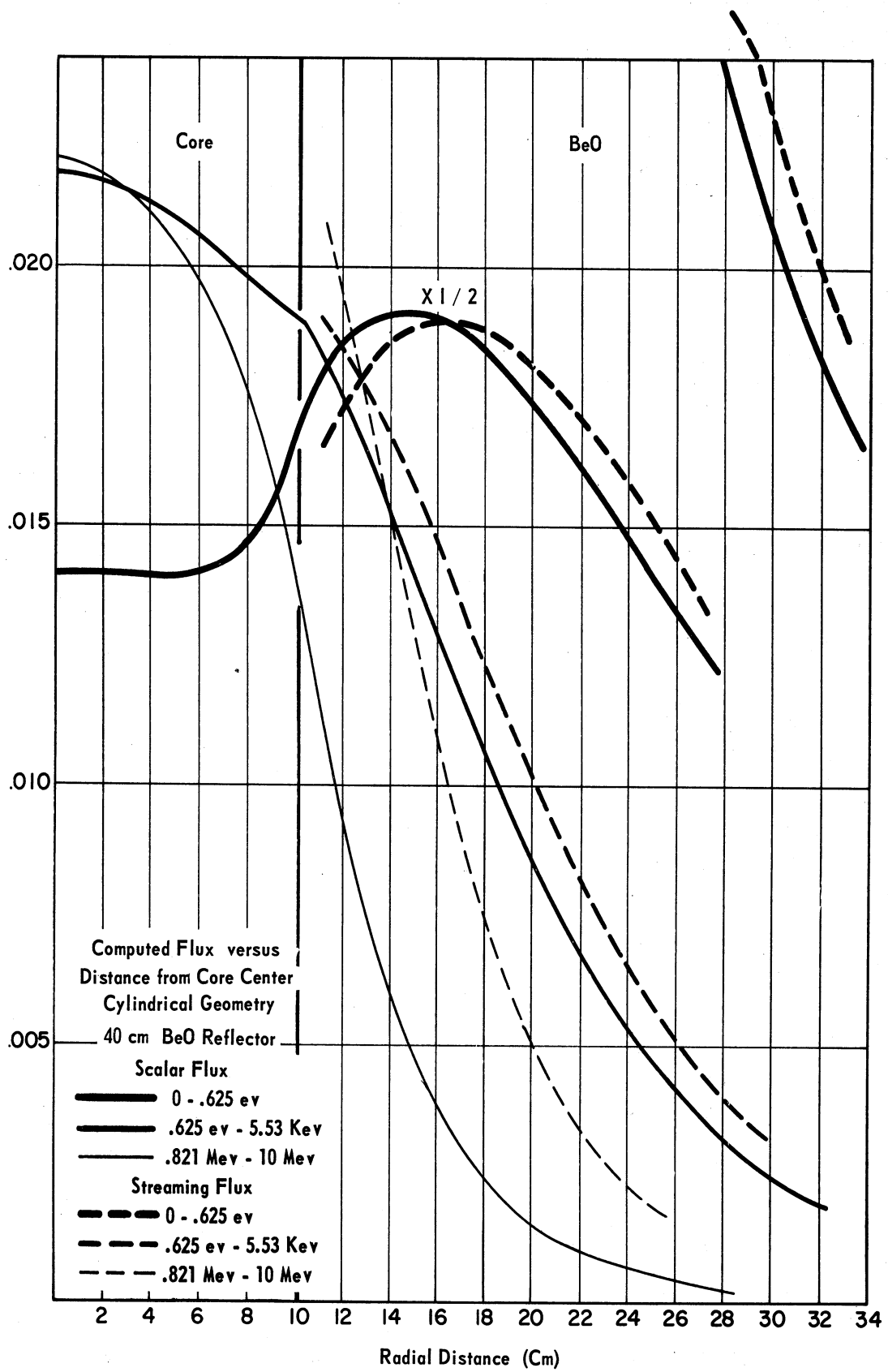


Figure A.9. Computed flux distributions; infinite BeO reflector; cylindrical geometry.

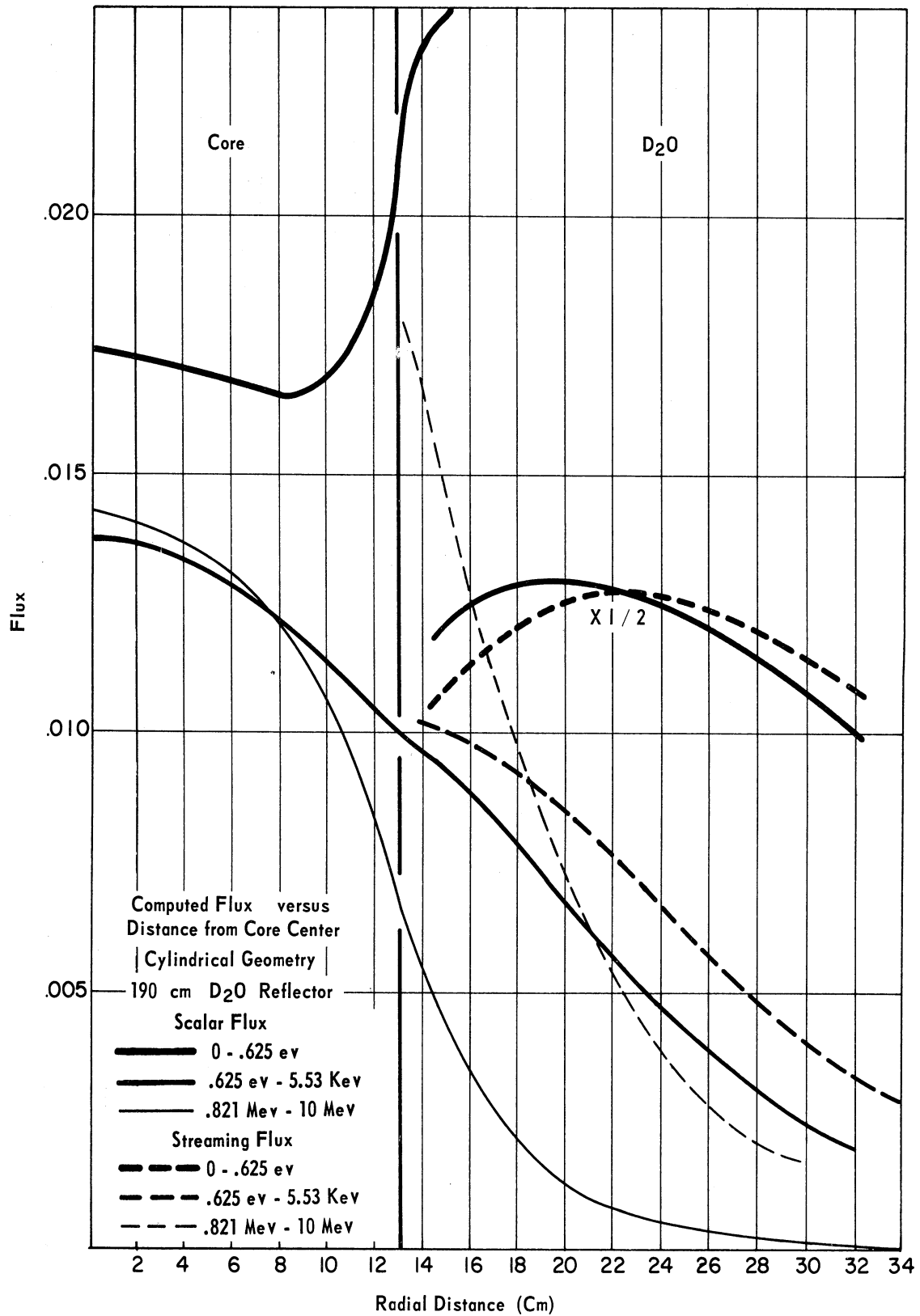


Figure A.10. Computed flux distributions; infinite D<sub>2</sub>O reflector; cylindrical geometry.

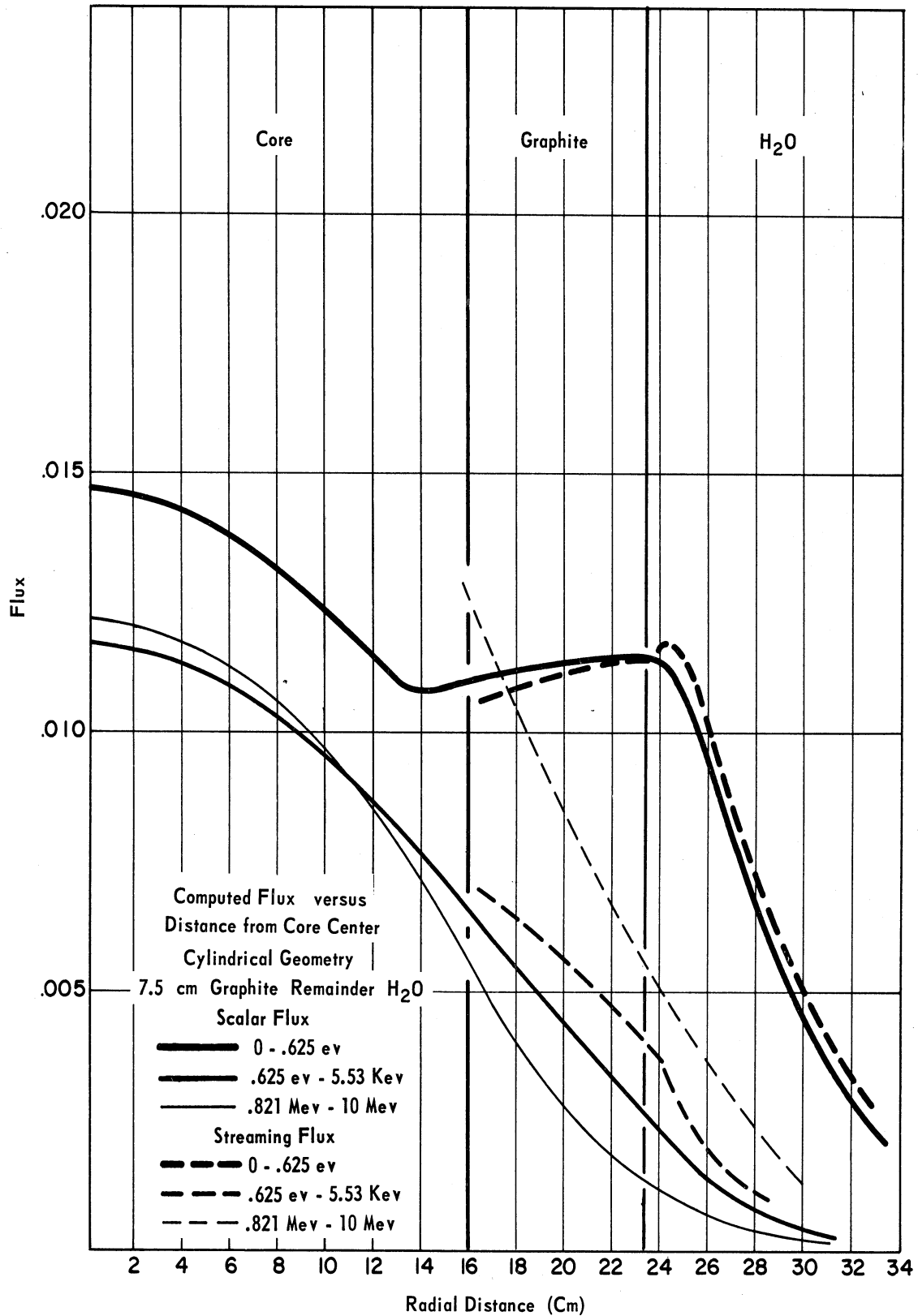


Figure A.11. Computed flux distributions; 7.5 cm graphite-remainder H<sub>2</sub>O; cylindrical geometry.

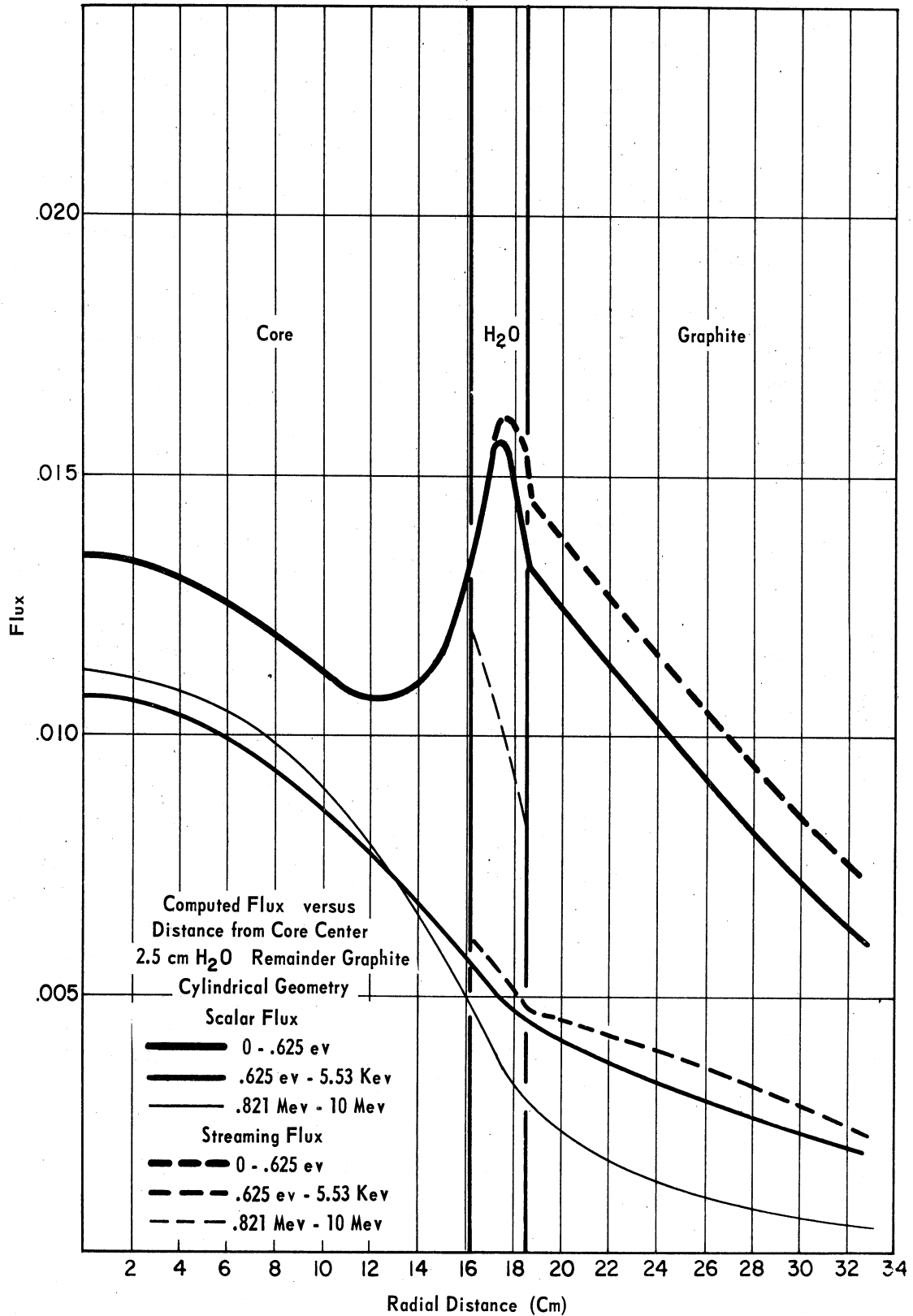


Figure A.12. Computed flux distributions; 2.5 cm H<sub>2</sub>O-remainder graphite; cylindrical geometry.

TABLE A. V

INFINITE REFLECTOR—CYLINDRICAL GEOMETRY  
VARIOUS REFLECTOR MATERIALS

	$S_{\max}^4$	$(S^4 - S^3)_{\max}$	$(S^4 - S^1)_{\max}$	$(S^3/S_{\max}^4)$	$(S^1/S_{\max}^4)$	$1/V$ in. <sup>-3</sup>
H <sub>2</sub> O Refl.	.0119	.0095	.0061	.218	.546	.00025
Graph. Refl.	.0151	.0071	.0098	.642	.690	.00046
BeO Refl.	.0379	.0258	.0309	.368	.258	.00083
D <sub>2</sub> O Refl.	.0255	.0191	.0224	.279	.183	.00050
7.5 cm Graph. Remainder	.0118	.0088	.0070	.305	.432	.00034
H <sub>2</sub> O 2.5 cm H <sub>2</sub> O Remainder Graph.	.0161	.0108	.0068	.329	.609	.00033

3.3 (compared with the H<sub>2</sub>O reflected core). The behavior of both BeO and D<sub>2</sub>O in extending the thermal streaming flux peak farther from the core than in H<sub>2</sub>O is a reason for the improved spectral ratio,  $(S^1/S_{\max}^4)$ . This fact presents a strong motivation for increasing the average reactor power density by improved reflection rather than integrated power boost. Infinite reflection by D<sub>2</sub>O increases the average power density by a factor of 2 over the H<sub>2</sub>O reflected core, whereas  $(S^4 - S^1)_{\max}$  goes up by a factor of 3.7.

Infinite graphite reflection shows up poorly in this set of calculations. Graphite used in conjunction with water demonstrates some im-

provement. The effect of 1 in. of water located between the core and the graphite is conspicuous. This configuration gives rise to significant gains in  $\beta_{\max}^4$  and  $(\beta^4 - \beta^3)_{\max}$ .

#### REFLECTOR INSERTS

The effect of reflector inserts of graphite, BeO, and D<sub>2</sub>O was examined for the equilibrium Xe, 8.4 percent fuel burnup composition. The geometry is sketched in Figure A.13. The fundamental core dimensions shown in Figure A.13a were established from a one-dimensional simulation study. Calculations were performed in XY geometry, and the vertical transverse bucklings recorded in Table A.I were used to account for leakage in the third dimension. The insert widths were chosen to enable the inserts to accommodate a six inch port. The reactivity contributions,\*  $\delta k/k$ , are recorded in Table A.VI along with the other significant quantities. Figures A.15-A.18 present the scalar flux and streaming flux distributions along the x-axes of the inserts. Figure A.19 and the bottom row of Table A.VI present the results of a calculation of the core displayed in Figure A.14, possessing full 6 in. layers of BeO.

The insert study permits a comparison of the effects of H<sub>2</sub>O, graphite, D<sub>2</sub>O, and BeO independent of power density influences (a somewhat artificial situation). Light water excels from the standpoint of suppression

---

\*The core dimensions were held constant, therefore all of the inserts, possessing better reflector properties than H<sub>2</sub>O, constituted positive reactivity perturbations. Enhancement of the thermal flux arising from an increase in power density, then, does not appear here.

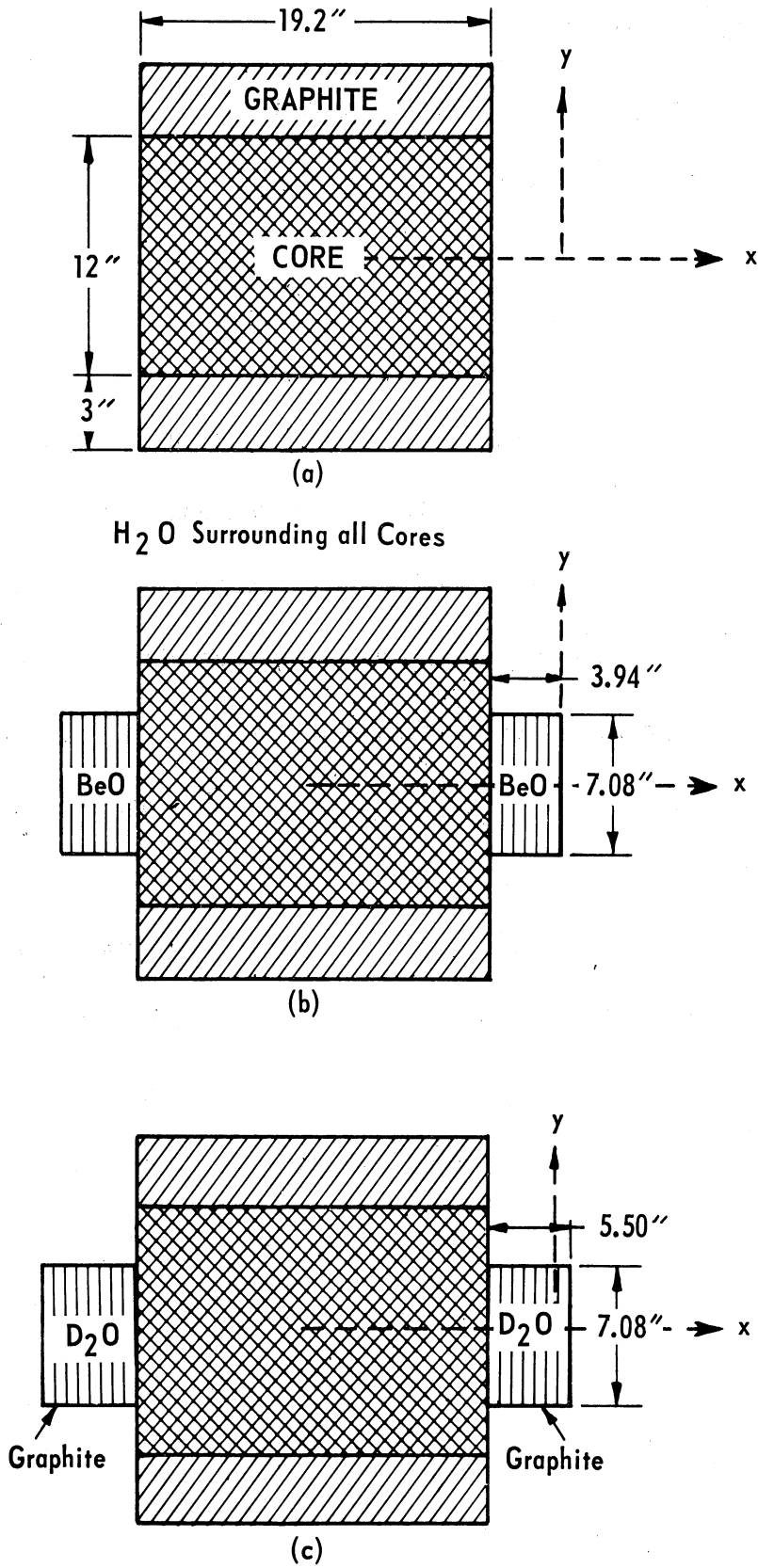


Figure A.13. Core geometries for material insert studies.



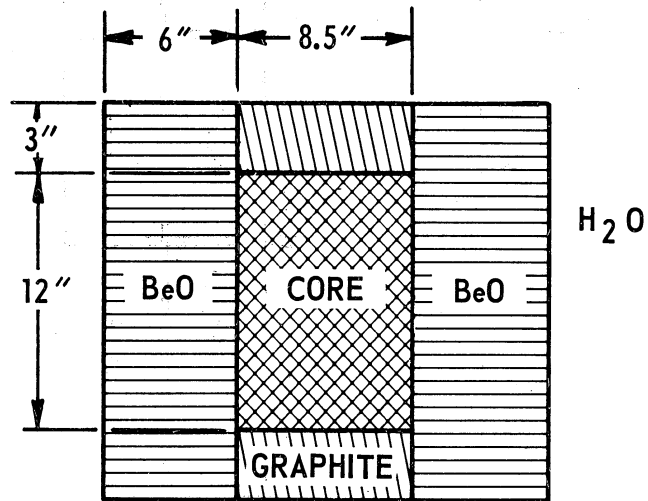


Figure A.14. Core geometry for 6 in. BeO reflector.

TABLE A. VI  
 TWO-DIMENSIONAL CALCULATIONS; FIXED SIZED CORE—INSERTS OF VARIOUS MATERIALS

	$S_{\max}^4$	$(S^4 - S^3)_{\max}$	$(S^4 - S^1)_{\max}$	$(S^3/S_{\max}^4)$	$(S^1/S_{\max}^4)$	$\delta k/k$	$1/V$ in. <sup>-3</sup>
Full H <sub>2</sub> O	.0316	.0234	.0173	.266	.506	---	.00018
Graph. Insert	.0288	.0225	.0211	.271	.347	+1.92%	.00018
BeO Insert	.0288	.0205	.0212	.389	.375	+2.3 %	.00018
D <sub>2</sub> O Insert	.0361	.0279	.0289	.266	.266	+1.86%	.00018
6 in. BeO	.0980	.0649	.0759	.330	.212	---	.00041

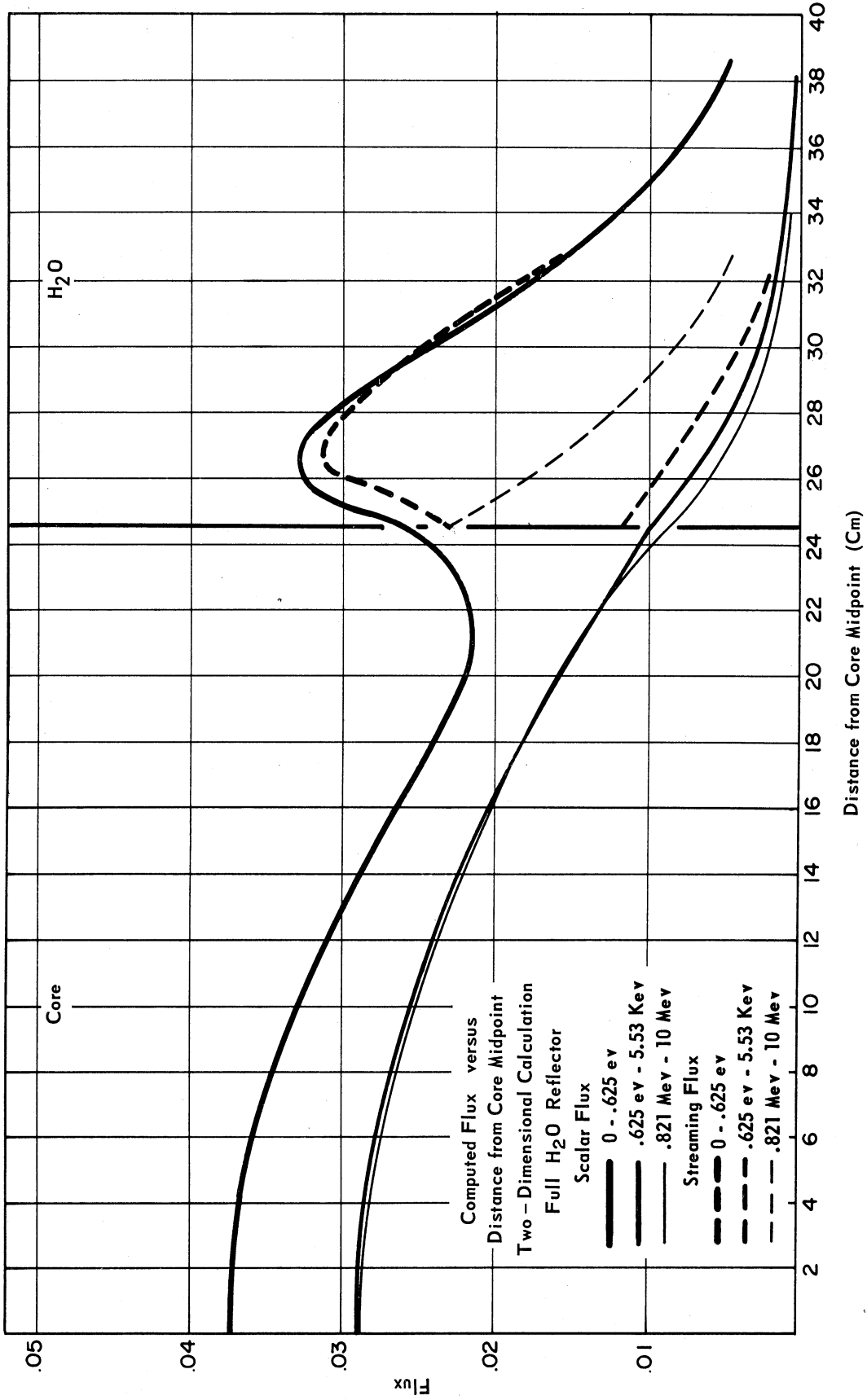


Figure A.15. Two-dimensional computed flux distributions; H<sub>2</sub>O reflected.

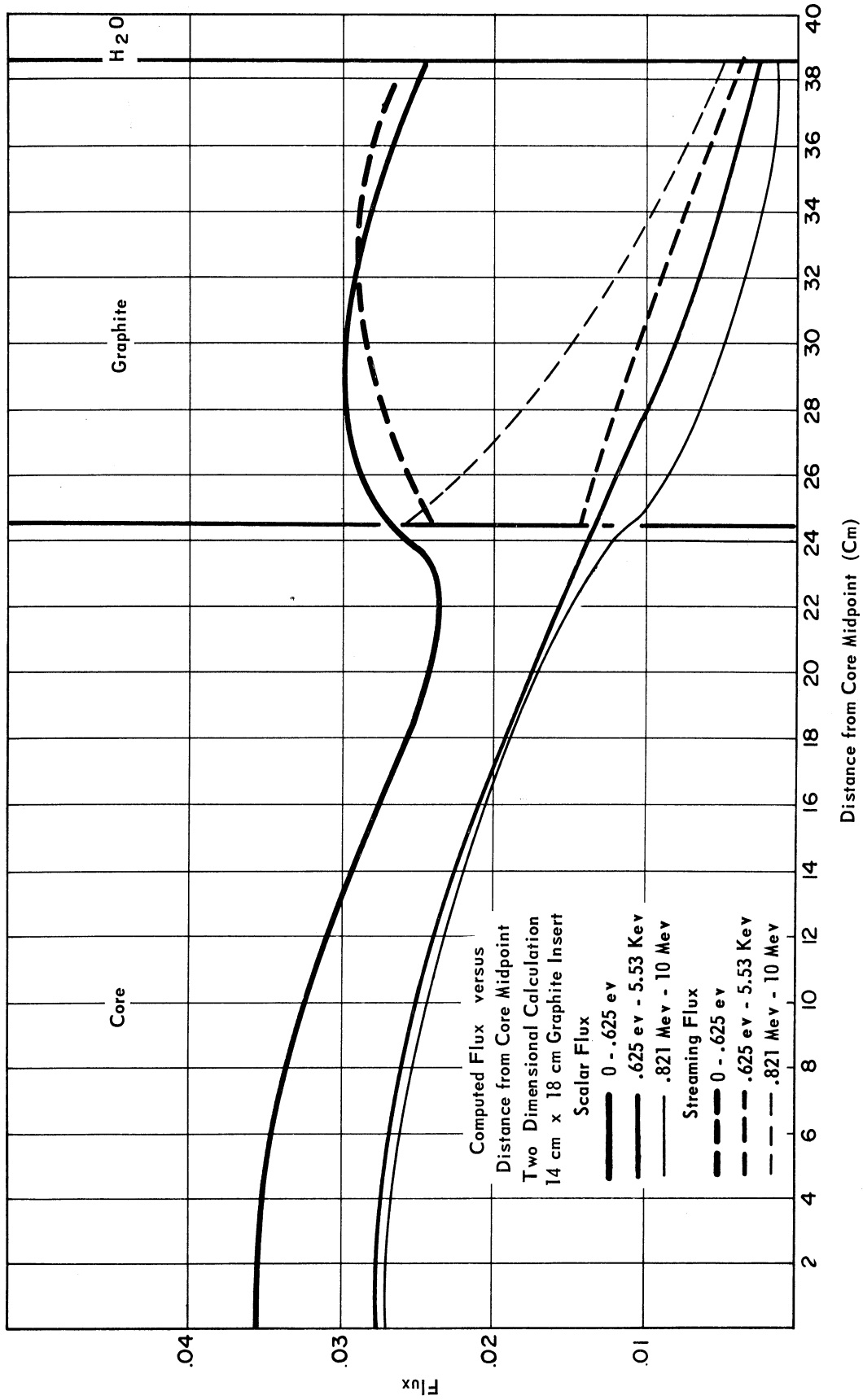


Figure A.16. Two-dimensional computed flux distributions; graphite insert.

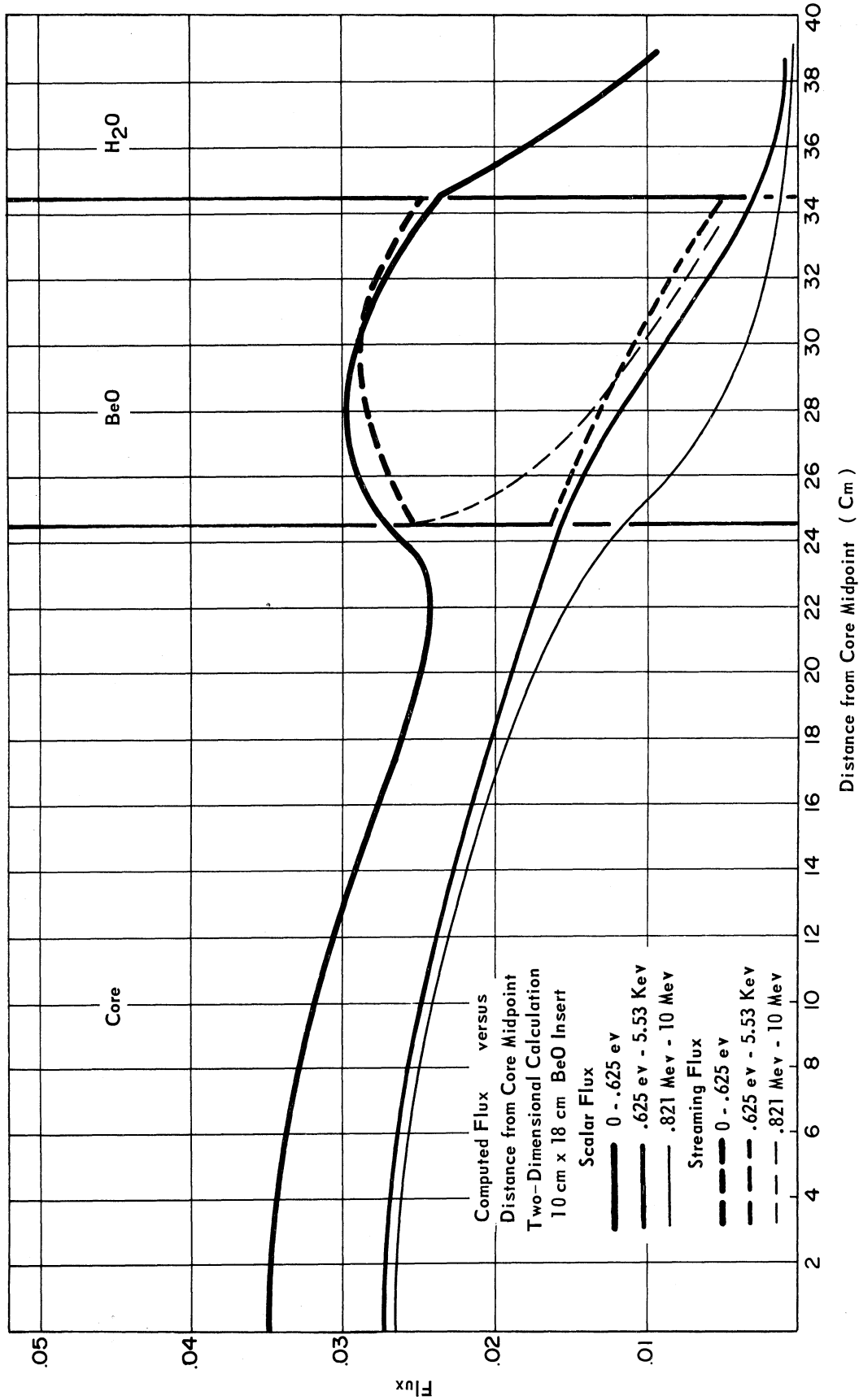


Figure A.17. Two-dimensional computed flux distributions; BeO insert.

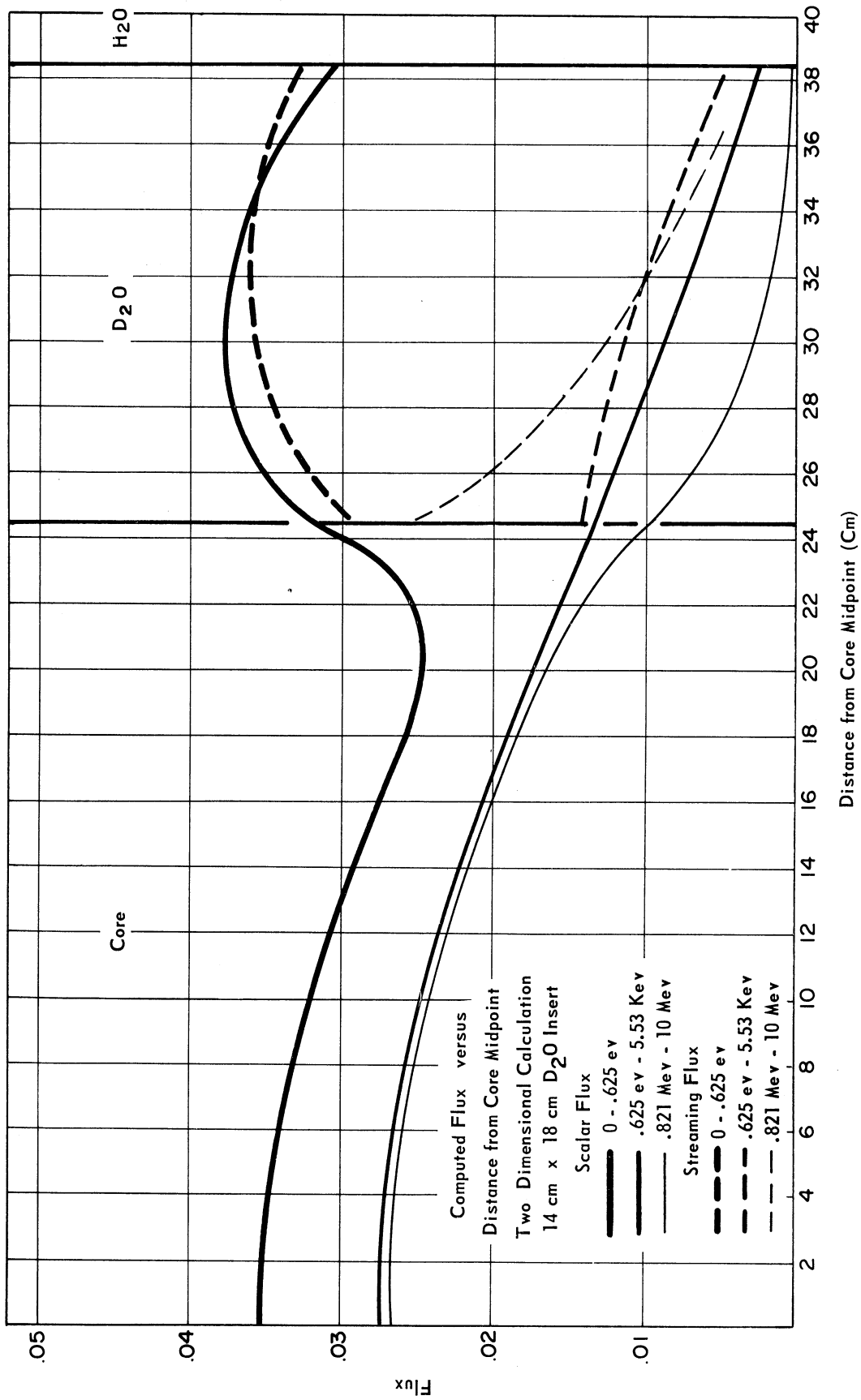


Figure A.18. Two-dimensional computed flux distributions; D<sub>2</sub>O insert.

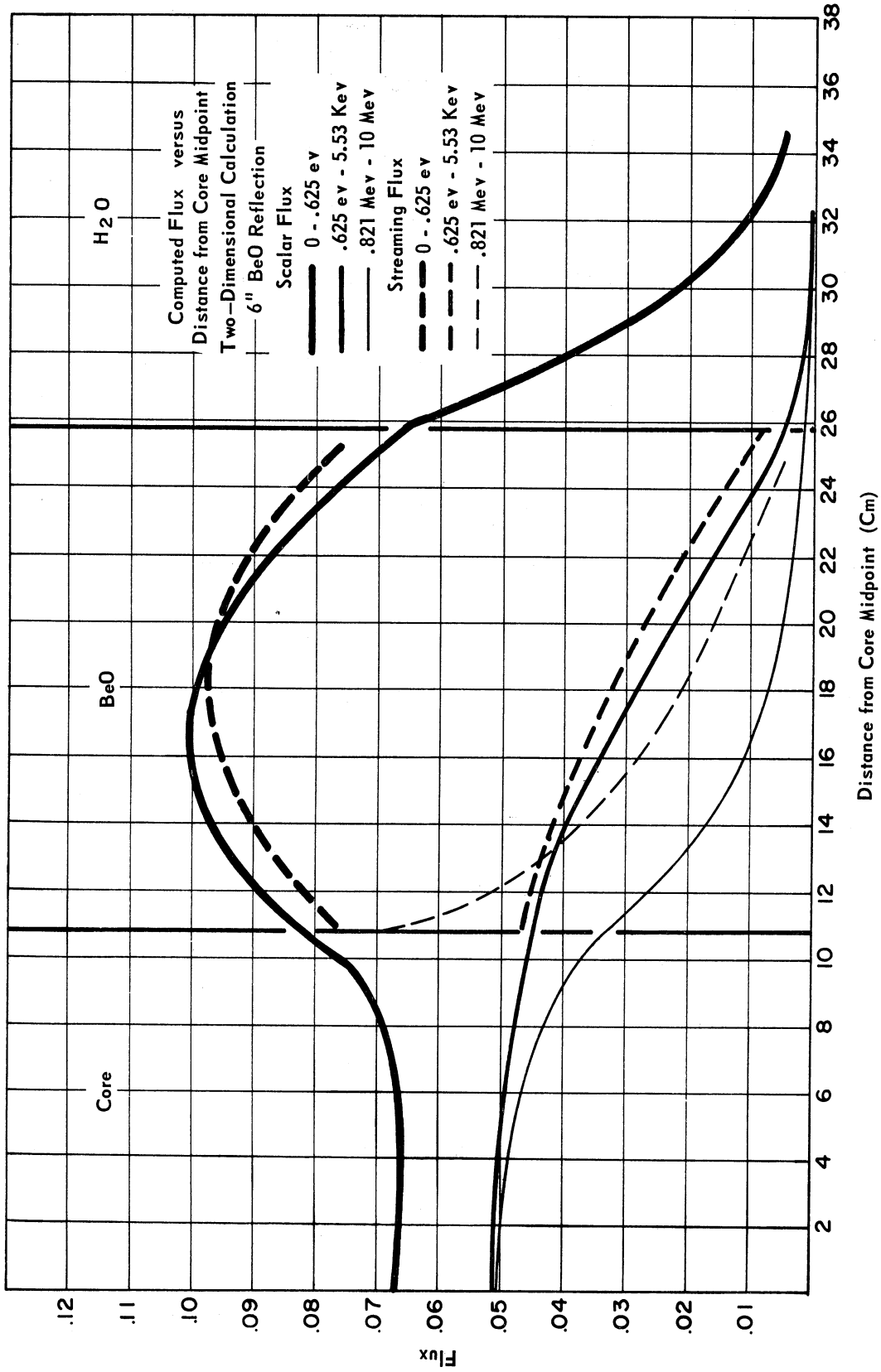


Figure A.19. Two-dimensional computed flux distributions; 6 in. BeO reflector.

of the epithermal content of the spectrum, exemplified by comparison of the quantities  $(\mathcal{L}^3/\mathcal{L}_{\max}^4)$  and  $(\mathcal{L}^4 - \mathcal{L}^3)_{\max}$  for all four materials. Every reflector insert diminishes the ratio,  $(S^1/S_{\max}^4)$ . As before, we attribute this effect to the longer diffusion lengths possessed by the insert materials, extending the high thermal flux region farther into the reflector. The  $D_2O$  insert results are particularly conspicuous. In addition to a 65 percent increase in the quantity  $(\mathcal{L}^4 - \mathcal{L}^1)_{\max}$ , the  $D_2O$  insert brings about a 14 percent enhancement in the thermal flux.

#### REFLECTOR LAYERS IN PARALLELEPIPED GEOMETRY

The final study constitutes a comparison of the streaming flux for 3 in. and 6 in. layers of reflector materials completely covering two faces of a rectangular parallelepiped reactor core. Figure A.20 is an illustration of the geometry. The fundamental water reflected core is sketched in Figure A.20a. Equilibrium Xe, 8.4 percent fuel burnup was chosen for the core composition. Once again,  $H_2O$ , graphite, BeO, and  $D_2O$  were examined. The configurations were simulated with one-dimensional computations. The results are tabulated in Table A.VII. Together with the quantities previously tabulated, an additional dimension,  $d$ , is listed, which is the distance from the core to the reflector location appropriate to the quantity alongside it. Figures A.22 and A.23 present the quantities  $(\mathcal{L}^4 - \mathcal{L}^3)_{\max}$  and  $(\mathcal{L}^4 - \mathcal{L}^1)_{\max}$  plotted versus



the dimension  $a$ .<sup>\*</sup> Dimension  $a$  is an inverse measure of the relative average power density.

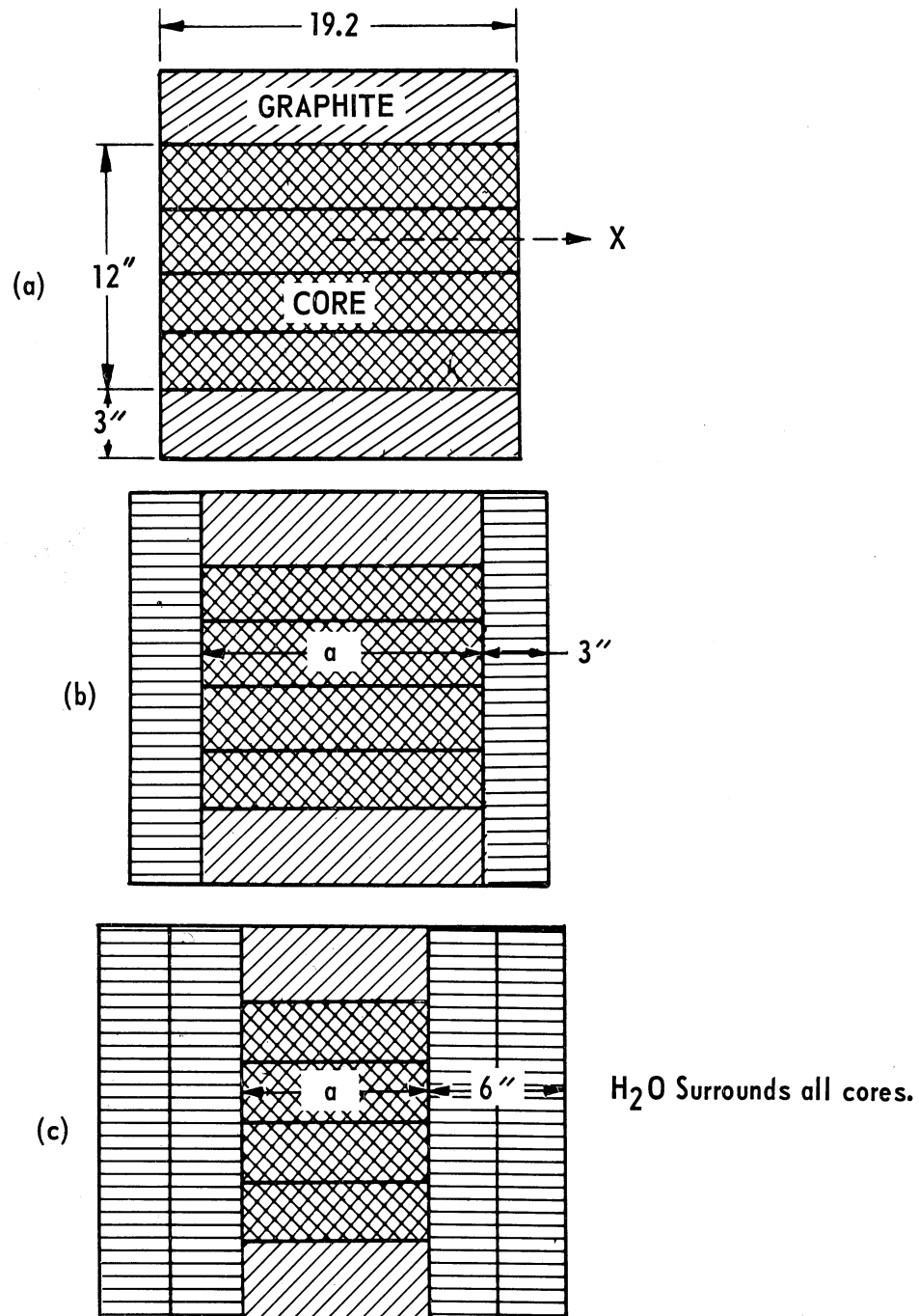


Figure A.20. Core geometries for 3 in. and 6 in. reflectors of various materials.

<sup>\*</sup>Additional points for 4-1/2 in. of the reflector materials were computed to obtain the shapes of the curves.

The consequence of shrinking dimension  $a$  by extension of the transverse dimension, illustrated in Figure A.21, is compared in Table A.VII and Figures A.22 and A.23 with the results of reflection by 3 in. and 6 in. layers of reflector materials. Although this calculation was presented in Section A.4 for the cold-clean core composition, it is of interest to compare this configurational effect with the effect of reflection for the fuel composition presently under consideration.

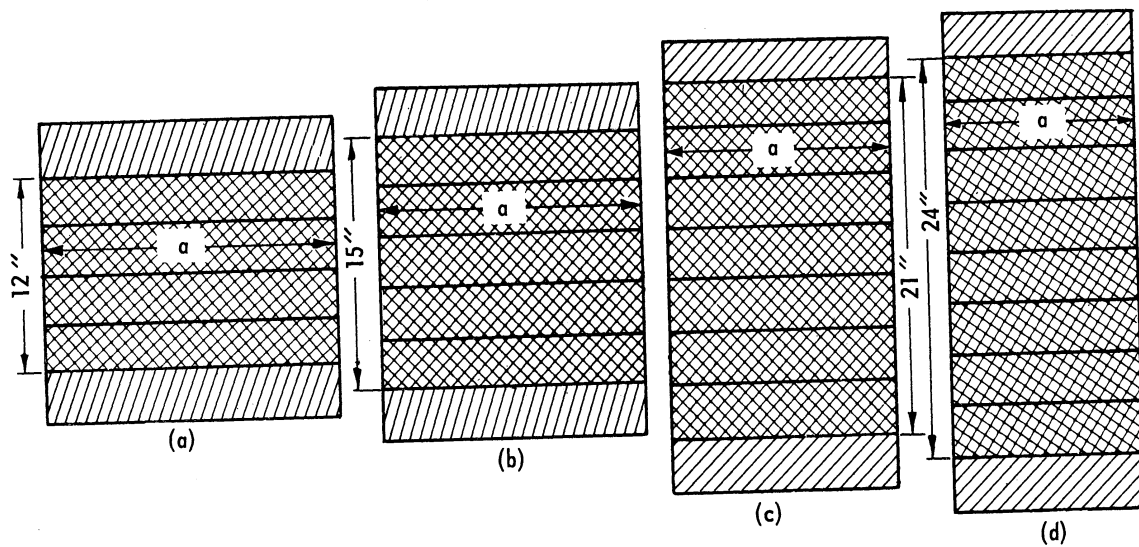


Figure A.21. Core geometries for  $H_2O$  reflected configuration studies (equilibrium Xe-8.4 percent burnup fuel).

The results appearing in Table A. VII are too numerous to discuss in detail. The geometry considered in this portion of the study has practical application for ports located  $180^\circ$  apart. Graphite makes a far better showing here than in the cylindrical geometry study. The maximum thermal streaming flux,  $(S_{max}^4)$ , in this configuration increases more rapidly than the average power density with improved reflection. The results for reflection by 6 in. of  $D_2O$  are striking.\* Figures A.22

\*Due to the calculational simplification of region-independent bucklings (thermal, in particular), the results for the 6 in. reflectors may be highly unrealistic.

TABLE A.VII

## THREE AND SIX INCH REFLECTORS OF VARIOUS MATERIALS

	$S^4_{\max}$	d in.	$(S^3/S^4_{\max})$	$(S^1/S^4_{\max})$	$(S^4-S^3)_{\max}$	d in.	$(S^4-S^1)_{\max}$	d in.	a in.	$1/V$ in. <sup>-3</sup>
3 in. Graph. Refl. 4 Elem. Trans.	.614	3	.254	.324	.474	3	.408	3	15.5	.000223
6 in. Graph. Refl. 4 Elem. Trans.	1.28	4.3	.186	.174	1.08	5.6	1.09	5.6	10.9	.000317
3 in. BeO Refl. 4 Elem. Trans.	.773	2.1	.333	.307	.582	3.0	.600	3.0	12.9	.000268
6 in. BeO Refl. 4 Elem. Trans.	1.65	3.1	.250	.140	1.29	3.9	1.56	3.9	8.5	.000406
3 in. D <sub>2</sub> O Refl. 4 Elem. Trans.	.853	3	.254	.232	.636	3	.656	3	14.4	.00024
6 in. D <sub>2</sub> O Refl. 4 Elem. Trans.	3.45	4.3	.144	.074	2.99	4.9	3.22	4.9	5.45	.000635
H <sub>2</sub> O Refl. 4 Elem. Trans.	.485	.9	.216	.464	.385	1.1	.282	1.3	19.2	.00018
H <sub>2</sub> O Refl. 5 Elem. Trans.	.714	.9	.216	.444	.569	1.1	.428	1.3	15.0	.000185
H <sub>2</sub> O Refl. 7 Elem. Trans.	.965	.9	.216	.422	.770	1.1	.596	1.3	12.2	.000163
H <sub>2</sub> O Refl. 8 Elem. Trans.	1.039	.9	.216	.416	.830	1.1	.648	1.3	11.6	.00015

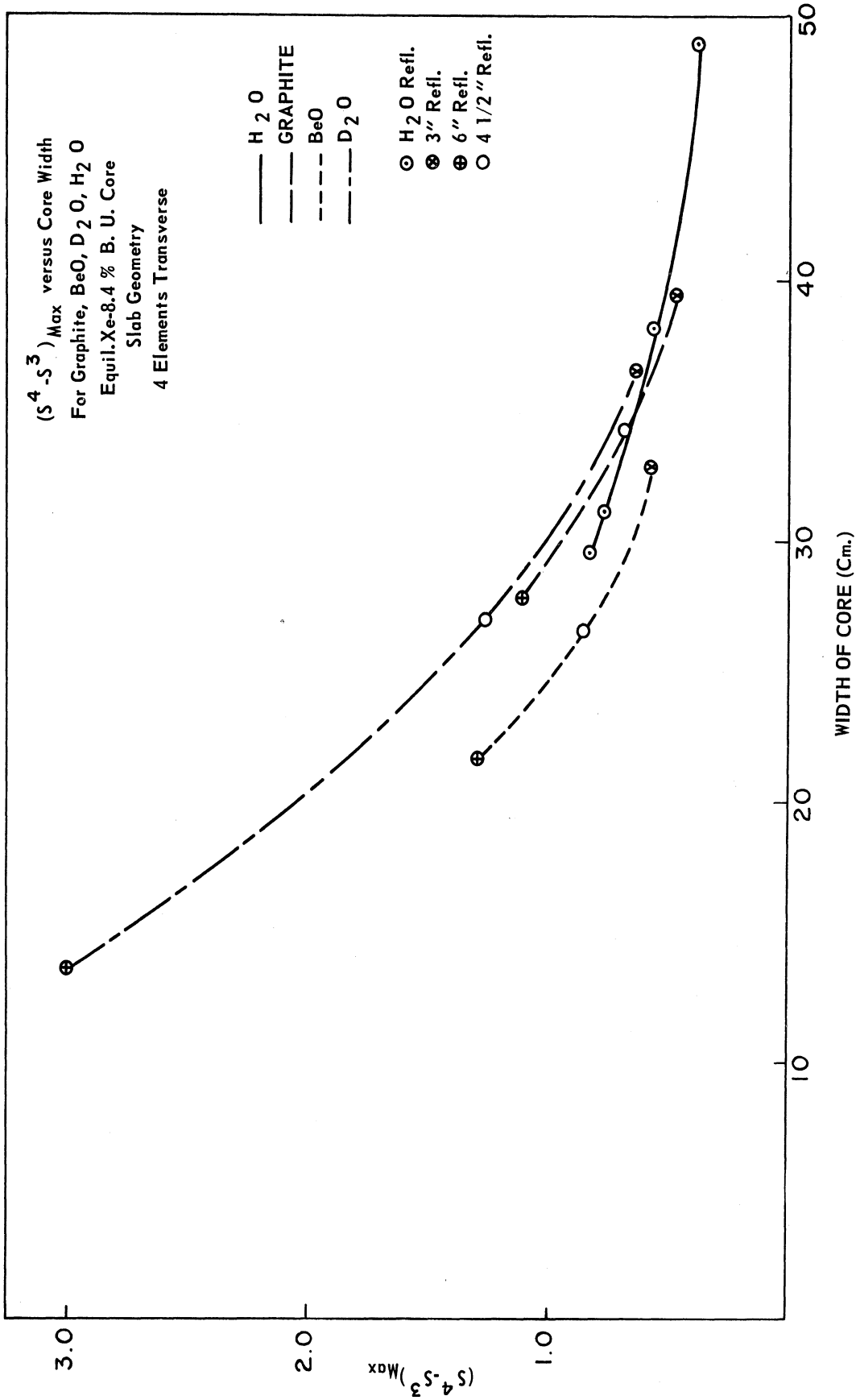


Figure A.22.  $(S^4 - S^3)_{\text{max}}$  for 3- and 6-in. reflection.

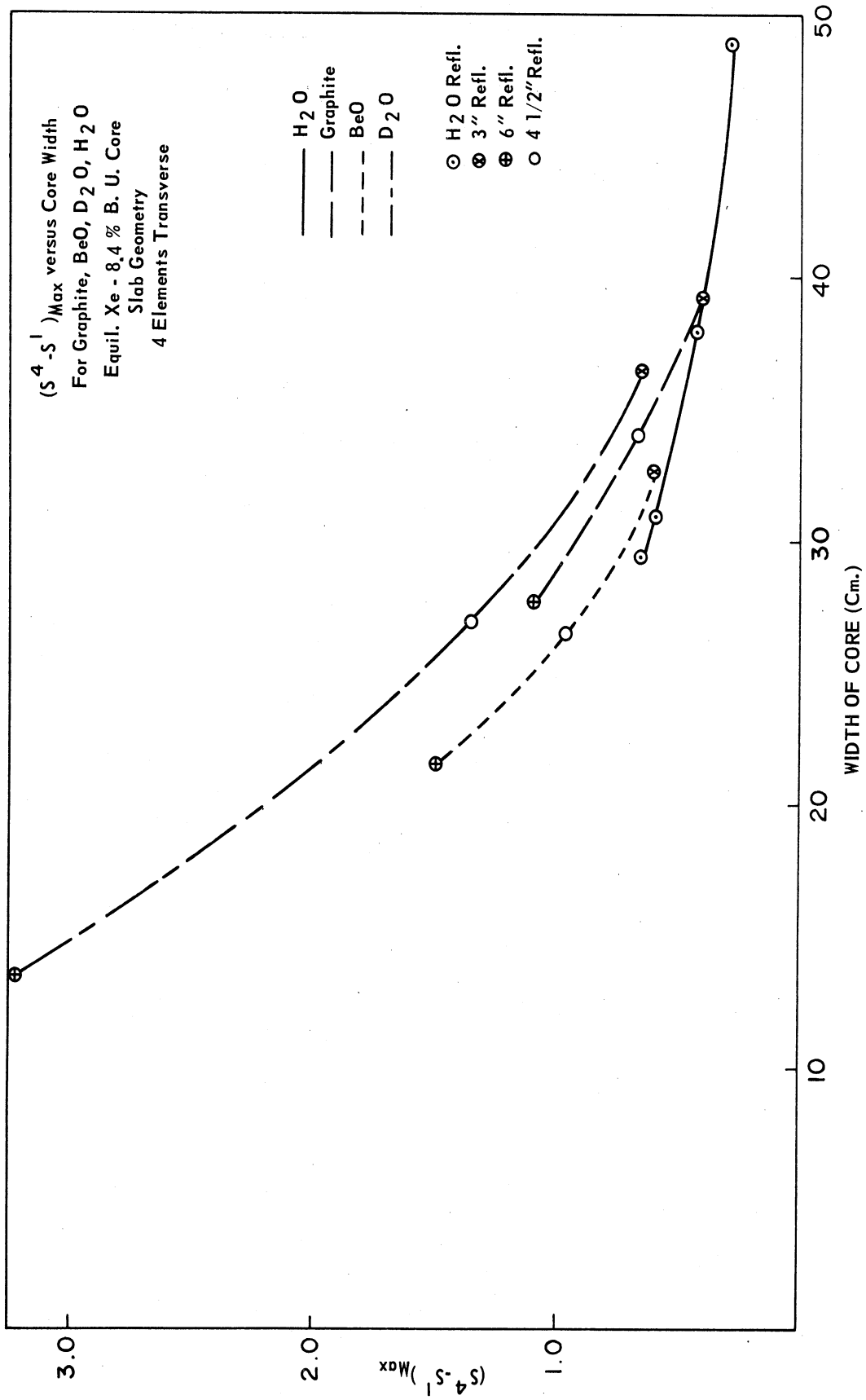


Figure A.23.  $(S^4 - S^1)_{\text{max}}$  for 3- and 6-in. reflection.

and A.23 compare the reflectors on the basis of constant average power density (excluding the curves for H<sub>2</sub>O reflection obtained by altering the ratio of the core dimensions). On this basis, D<sub>2</sub>O excels, followed in order by graphite and BeO.

## 6. Final Remarks

Although the group constants used in the calculations were obtained in a consistent manner, a question may be raised regarding the validity of the cross sections. The source of the cross section library is cited in Appendix C. Much of the analysis reported in the literature<sup>31</sup> is based upon this set of cross sections or slight variations of it. The reasonable agreement between the predicted and measured distributions of the thermal and epithermal fluxes presented in Figures 3.6, 3.8, and 3.19 tends to corroborate the validity of the group constants for H<sub>2</sub>O, graphite, and the core.

In order to examine the validity of the D<sub>2</sub>O group constants, a measurement was made with a limited quantity of D<sub>2</sub>O, and the experimental results were compared with a group-diffusion calculation. A flux traverse was performed in a cylindrical D<sub>2</sub>O insert 5 in. long and 5-1/2 in. in diameter placed against the center of the south face of the FNR.<sup>32</sup> The two-dimensional analysis utilized 4 groups in cylindrical geometry. A comparison of the measured and calculated thermal and epithermal flux distributions along the axis of the insert is presented in Figure A.24.

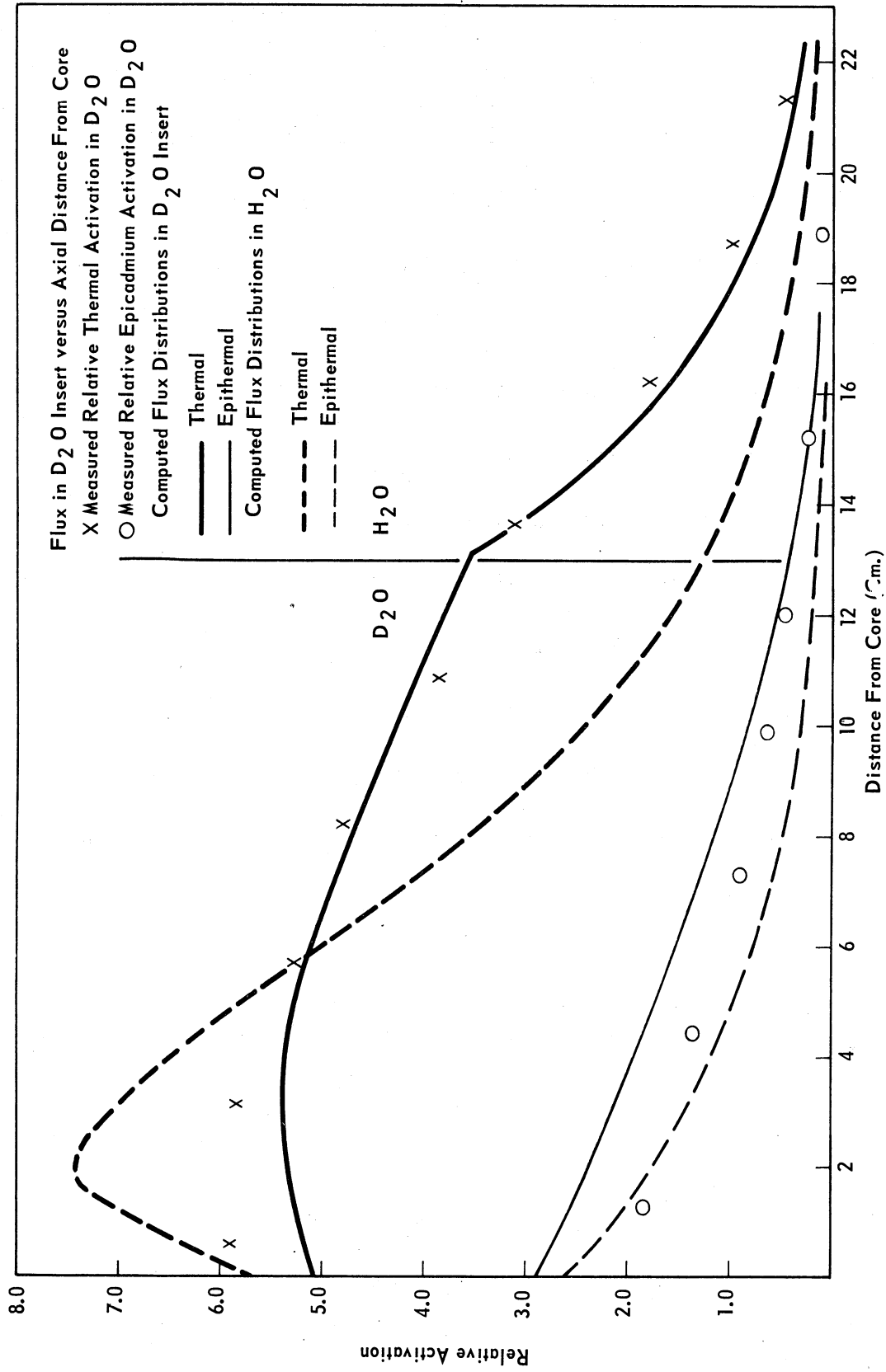


Figure A.24. Measured and computed flux distributions along axis of cylindrical D<sub>2</sub>O insert.

Both the measured and calculated distributions were normalized to distributions obtained along the same axis in the complete light water medium (also plotted in Figure A.24).

Many of the results reported here were based upon the technique described in Section A.2, simulating three-dimensional geometry using one-dimensional computations. An examination of the validity of this method is afforded by comparing the results of actual two-dimensional calculations with the results of one-dimensional simulations. Since four-group, two-dimensional computer studies are extremely time-consuming, few comparisons were made. The first comparison was carried out for the core illustrated in Figure A.14, possessing symmetric 6 in. layers of BeO. The two-dimensional calculation resulted in an eigenvalue (See Eq. B.1) .6 percent lower than that obtained in the one-dimensional simulation. The water reflected core of Figure A.13a was examined next, the two-dimensional calculation yielding an eigenvalue 3 percent lower than the one-dimensional simulation. Finally, the deviation for the cold-clean, water reflected core shown in Figure A.1b was 2 percent. None of the discrepancies are serious, considering the disagreement between the results of group-diffusion calculations and precise criticality determinations for clean, homogeneous assemblies reported by Feiner.<sup>33</sup> It is curious, however, that the smaller cores yield better agreement. It was anticipated that the deviation between the one-dimensional simulation results and the two-dimensional results would be inversely proportional to the core size, owing to corner effects.



Apparently a reflector composition influence exists, as well.

A question may be raised concerning the accuracy of the calculated fast flux magnitudes in the reflector,  $\phi^1$  and  $\phi^2$ . P-1 theory tends to overestimate the attenuation of the forward-peaked, high energy components of the spectrum. Experimental fast flux determinations are scarce. Since the reflector regions of greatest interest lie within 1 to 3 fast neutron mean free paths from the core, P-1 errors in the fast flux are presumed to be small.

Most of the core alterations examined in this appendix involved increases in the reactor power density. Practical considerations call for a remark concerning core heat removal capabilities. A cursory examination of this problem was carried out with an existent computer program,<sup>34</sup> originally written to evaluate the FNR two megawatt performance. The results of the calculation, assuming a constant coolant mass flow rate through the core and an integrated reactor power of one megawatt, indicate that in going from 24 to 4 regular fuel elements a maximum fuel cladding temperature rise of only 7°F is anticipated.

#### 7. Subroutine STREAM

Subroutine STREAM, used in conjunction with the FOG group-diffusion code (control program 3), computes the partial current, defined by:

$$j_i^+(x) = \frac{\phi_0(x)}{4} - \frac{l_{tr}}{6} \frac{d\phi_0(x)}{dx}, \quad (A.21)$$

and the streaming flux, defined by Eq. (A.6), at each mesh point in a designated region. The streaming flux integral is performed over the designated region plus the region before it. Thus for reasonable accuracy the width,  $w$ , of the region immediately before the designated region must be defined sufficiently large so that  $\sum_t^i w \gg 1$  for each energy group. The Fortran program listing of the revised main program of FOG and subroutine STREAM are recorded here.

In order to call the subroutine L63 of the input data must be set different from zero. Then a master card and one card for each energy group is expected at the end of the FOG input deck. The card arrangement is as follows:

Master Card (Format 4I12)

N(1) = 0	Bypass Subroutine
= 1	Utilize Subroutine
N(2) = 0	Do not compute $j^+$
= 1	Compute $j^+$
N(3) = 0	Do not compute $\mathcal{L}$
= 1	Compute $\mathcal{L}$
N(4) = I	I is the FOG region designated for the computation.

Cross Section Card\* (Format 2F12.0)

F(1) = $\sum_S^i$	Scattering cross section in region I
F(2) = $\sum_S^i$	Scattering cross section in region I-1

---

\*One card is required for each energy group.





```

9 IF (N26) 19,19,10
10 I=N27
WRITE OUTPUT TAPE 6,62,I
62 FORMAT (55H1
1I3)
DO 18 J=1,NOG
READ INPUT TAPE 7,64,(AA(K),K=1,2)
64 FORMAT(2F12.0)
SIGMS1=AA(1)
SIGMS2=AA(2)
WRITE OUTPUT TAPE 6,65,SIGMS1,SIGMS2,J
65 FORMAT(23H SIGMS IN REGION I-1 ISE16.8,
121H SIGMS IN REGION I ISE16.8,8H GROUP13)
LOTT = 0
I2=I-2
IF(I2)28,28,27
27 DO 20 N=1,I2
LOTTT = LM(N)
LOTT = LOTTT + LOTT
20 CONTINUE
28 LOT = LOTT + 1
I3=LM(I)
DO 17 K=1,I3
SUMM(K,J)= 0.0
I4=LOT+LM(I-1)
DO 13 L=LOT,I4
FL2=K
FL3=LM(I-1)+LOT-L
IF(((SIGA(I-1,J)+SIGMS1)*DELR(I-1)*FL3+(SIGA(I,J)+SIGMS2)*
1DELR(I)*FL2)-50.0)23,13,13
23 IF(L-I4)25,11,11
25 IF (L-LOT) 11,11,12
11 STR=((SIGMS1*PHI(L,J)+SOUP(L)*CHI(I-1,J))/2.0)*DELR(I-1)*EXP(
1-((SIGA(I-1,J) + SIGMS1) * DELR(I-1) * FL3
2) - ((SIGA(I,J)+SIGMS2) * DELR(I) * FL2))
GO TO 21
12 STR = ((SIGMS1*PHI(L,J)+SOUP(L)*CHI(I-1,J))*DELR(I-1)*EXP(-((
1SIGA(I-1,J) + SIGMS1) * DELR(I-1) * FL3)-((SIGA(I,J)+SIGMS2
2) * DELR(I) * FL2))
21 SUMM(K,J) = SUMM(K,J) + STR
13 CONTINUE
N=LOT+LM(I-1)
N1=N+K
DO 16 L=N,N1
FL4=N+K-L
IF(((SIGA(I,J)+SIGMS2)*DELR(I)*FL4)-50.0)24,16,16
24 IF(L-N)15,15,26
26 IF (L-N-K) 14,15,15
14 STR=((SIGMS2*PHI(L,J)+SOUP(L)*CHI(I,J))*DELR(I))*EXP(-(SIGA(I,J)+S
1IGMS2) * DELR(I) * FL4)
GO TO 22
15 STR = ((SIGMS2*PHI(L,J)+SOUP(L)*CHI(I,J))/2.0) * DELR(I)
1*EXP(-(SIGA(I,J)+SIGMS2)*DELR(I)*FL4)
22 SUMM(K,J) = SUMM(K,J) + STR
16 CONTINUE
17 CONTINUE
18 CONTINUE
IF (NOG-3) 35,35,32
32 WRITE OUTPUT TAPE 6,33
33 FORMAT(69H0 PT. IN REGION GROUP 1 GROUP 2 GROUP 3
1 GROUP 4)
WRITE OUTPUT TAPE 6,34,(K,SUMM(K,1),SUMM(K,2),SUMM(K,3),SUMM(K,4),
1K=1,I3)
34 FORMAT(I7,E22.8,3E14.8)
GO TO 19
35 IF (NOG-2) 39,39,36
36 WRITE OUTPUT TAPE 6,37
37 FORMAT(55H0 PT. IN REGION GROUP 1 GROUP 2 GROUP 3)
WRITE OUTPUT TAPE 6,38,(K,SUMM(K,1),SUMM(K,2),SUMM(K,3),K=1,I3)
38 FORMAT (I7,E22.8,2E14.8)
GO TO 19
39 WRITE OUTPUT TAPE 6,40
40 FORMAT(41H0 PT. IN REGION GROUP 1 GROUP 2)
WRITE OUTPUT TAPE 6,41,(K,SUMM(K,1),SUMM(K,2),K=1,I3)
41 FORMAT(I7,E22.8,E14.8)
19 RETURN
END

```

26

STREAMING FLUX IN REGION

226

326

426

626

28

128

29

30

31

32

33

133

34

135

36

236

336

436

536

636

37

39

40

41

44

46

47

147

48

148

248

348

49

51

52

153

55

56

61

55

56

61

62

63

63

63

63

63

63

63

63

63

63

63

63

63

63

63

63

63

63

## APPENDIX B

### DESCRIPTION OF THE CODES

Computer calculations were performed on the IBM-709, and later on the IBM-7090. Some revision of the Fortran language codes were necessary for compatibility with The University of Michigan executive system.<sup>35</sup> Program revisions involved tape number changes, function name revisions, memory zeroing, and occasional function deletions. In addition, since the executive system monitor occupies several thousand locations of the 32 K memory, it was often essential to shorten or break down programs written for the scope of the entire memory.

Group-diffusion codes solve the following set of coupled equations:

$$\begin{aligned}
 & -D^i \nabla^2 \phi^i + [D^i B_T^2 + \sum_a^i] \phi^i + \sum_{l \neq i} \sum_R^{i \rightarrow l} \phi^l \\
 & = \chi^i \sum_l \frac{(v \sum_F^l) \phi^l}{\alpha} + \sum_{l \neq i} \sum_R^{l \rightarrow i} \phi^l \quad . \quad (B.1)
 \end{aligned}$$

Finite-difference methods along with a variety of convergence accelerators are employed in obtaining solutions. Flexibility is generally built into a code in the form of an assortment of boundary conditions and specific geometrical configurations.

FOG<sup>36</sup> is a one-dimensional few-group diffusion code providing for as many as four energy groups and 239 space points. The code permits a choice of three geometries, nine sets of boundary conditions, and five

types of criticality searches. Downscattering between adjacent groups only is allowed.

TWENTY GRAND<sup>37</sup> is a two-dimensional group-diffusion code based upon the Equipoise convergence technique. Three thousand mesh points are accommodated, and the code was revised to handle as many as four energy groups (the original form accommodated six energy groups). Both XY and RZ geometries are available and neutron transfer between any of the groups is permitted. Zero flux, zero derivative, and logarithmic-derivative boundary conditions are utilizable.

Thermal neutron group constants were computed with TEMPEST<sup>38</sup>, the Fortran version of the SOFOCATE<sup>39</sup> code. Cross sections, supplied in the form of a library deck, can be averaged over a thermal spectrum determined from (i) the Wigner-Wilkins equation for light moderators, (ii) the Wilkins equation for heavy moderators, or (iii) a Maxwellian distribution.

FORM,<sup>40</sup> the Fortran version of MUFT-IV,<sup>41</sup> a Fourier transform slowing-down code, was used to obtain fast group constants. Fast spectra are generated from the spatially Fourier-transformed slowing-down distribution by the P-1 or B-1 approximation, with or without the Selengut-Goertzel approximation. Cross section data are supplied on tape in the form of a 54-group cross section library from .625 ev to 10 Mev. The memory size limitations of The University of Michigan system required alteration of the main program, a listing of which appears at the end of this appendix.

C FORM (FORTRAN MUFT) PROGRAM - WRITTEN AT NORTH AMERICAN AVIATION  
 C REVISED UNIVERSITY OF MICHIGAN , 1962

```

$COMPILE FORTRAN, PRINT OBJECT, PUNCH OBJECT                MAIN1000
  DIMENSION FILE3(7776),PROB(325,18),D3(644), D1(599),D2(1641), 0
  1DUMMY(5215)
  COMMON FILE3,D1,PROB,D2,NSD,IP,A,NED,D3,NADD,DUMMY,NFIRST
  CALL ZERO
  REWIND 3
  NFIRST=1
  CALL DELSET
  CALL SEQPGM
  END

```

80  
90  
100

C SUBROUTINE DELSET

```

$ASSEMBLE,PUNCH OBJECT                ZERO0000
  ENTRY ZERO
  ZERO LXA **4,1
  8STZ 7777,1
  TIX *-1,1,1
  TRA 1,4
  OCT 52661
  END

```

```

$COMPILE FORTRAN, PRINT OBJECT, PUNCH OBJECT                MAIN2000
  DIMENSION FILE3(7776),PROB(325,18),D3(644), D1(599),D2(1641), 0
  1DUMMY(5215)
  COMMON FILE3,D1,PROB,D2,NSD,IP,A,NED,D3,NADD,DUMMY,NFIRST,
  INTIME,NTEST,IP,NSD,NS,NI,NU,L,NALPHA,NIN,NRA
  1 CALL INPUT
  CALL INP1
  IF(NFIRST-1)2,2,4
  2 NTEST=0
  NTIME=1
  CALL READLB(IP,NSD,NTIME,NTEST)
  IF(NTEST)12,3,12
  12 CALL SELPGM(1)
  3 IF(NADD)13,13,11
  11 CALL ADD
  13 WRITE TAPE 3,(FILE3(I),I=1,7776)
  CALL SELPGM(4)
  4 READ TAPE 3,(FILE3(I),I=1,7776)
  CALL SEQPGM
  END

```

110  
120  
130  
140  
150  
160  
170  
180  
190  
200  
220

C SUBROUTINE INPUT  
 C SUBROUTINE INP1  
 C SUBROUTINE READLB  
 C SUBROUTINE ADD

```

$COMPILE FORTRAN, PRINT OBJECT, PUNCH OBJECT                MAIN3000
  DIMENSION FILE3(7776),PROB(325,18),D3(644), D1(599),D2(1641), 0

```



```

1DUMMY(5215)
COMMON FILE3,D1,PROB,D2,NSD,IP,A,NED,D3,NADD,DUMMY,NFIRST,
INTIME,NTEST
CALL GRUCON(NFIRST)
CALL SEQPGM
END

```

C SUBROUTINE GRUCON

```

$COMPILE FORTRAN, PRINT OBJECT, PUNCH OBJECT MAIN4000
DIMENSION FILE3(7776),PROB(325,18),D3(644), D1(599),D2(1641), 0
1DUMMY(5215)
COMMON FILE3,D1,PROB,D2,NSD,IP,A,NED,D3,NADD,DUMMY,NFIRST,
INTIME,NTEST,IP,NSD,NS,NI,NU,L,NALPHA,NIN,NRA
IF(NFIRST-1)6,6,7
6 NTIME=2 240
CALL READLB(IP,NSD,NTIME,NTEST) 250
IF(NADD/10)15,15,14 260
14 CALL ADD 270
15 WRITE TAPE 3,PROB 280
7 CALL SEQPGM 290
END

```

C SUBROUTINE READLB  
C SUBROUTINE ADD

```

$COMPILE FORTRAN, PRINT OBJECT, PUNCH OBJECT MAIN5000
DIMENSION FILE3(7776),PROB(325,18),D3(644), D1(599),D2(1641), 0
1DUMMY(5215)
COMMON FILE3,D1,PROB,D2,NSD,IP,A,NED,D3,NADD,DUMMY,NFIRST
CALL SLODON(NFIRST) 300
REWIND 3 310
CALL EDIT12 320
IF(NED-2)10,10,8 330
8 CALL EDIT3 340
IF(NED-3)10,10,9 350
9 CALL EDIT4 360
10 NFIRST=NFIRST+1 370
CALL SELPGM(3)
12 CALL SELPGM(1) 06000390
END 400

```

C SUBROUTINE SLODON  
C SUBROUTINE EDIT12  
C SUBROUTINE EDIT3  
C SUBROUTINE EDIT4

## APPENDIX C

### COMPOSITIONS AND GROUP CONSTANTS

Table C.I is a listing of all compositions considered for this study. Two classes of core compositions were examined. The first is the cold-clean initial fuel loading of 140 gm/element. The second is appropriate to a core with equilibrium xenon and 8.4% fuel burnup, representative of the FNR operating at one megawatt during the fall of 1962. Core compositions are presented for a homogenized regular fuel element with the water between subassemblies averaged into the composition. The homogenization of the subassembly is valid since the disadvantage factor of the fuel is .988.<sup>22</sup> The existence of partial elements and poison rods was neglected.

Thermal group constants were evaluated by averaging cross section data over spectra computed by the TEMPEST code from 0-.625 ev. The TEMPEST library of cross sections, most recently revised in February, 1961, was used throughout for consistency. A temperature of 300°K and a material buckling of .0130 cm<sup>-2</sup> were used as input data. Core constants were evaluated using the Wigner-Wilkins light moderator approximation. Figure C.1 shows the Wigner-Wilkins spectrum computed for the cold-clean core composition compared to a Maxwellian spectrum at 300°K. Both spectra were normalized in the following manner:

$$\int_0^{.625 \text{ ev}} \phi(E) dE = 1.0 \quad . \quad (C.1)$$

Reflector constants were averaged over a Maxwellian spectrum at 300°K (the buckling was taken to be zero). Table C.II lists the thermal group constants for the compositions in Table C.I.

Fast group constants, evaluated by the FORM code, are entered in Table C.III. The FORM library tape, updated to May, 1962, was obtained directly from the North American Aviation Corporation, and was used as the source of all cross section data. The four-group scheme had the following breakpoints: .625 ev-5.53 Kev; 5.53 Kev-.821 Mev; .821 Mev-10 Mev. Constants were evaluated for a full  $U^{235}$  fission source spectrum using the B1 approximation and the self-consistent age approximation. A buckling of  $.0130 \text{ cm}^{-2}$  was used to obtain core constants and  $.00001 \text{ cm}^{-2}$  for the reflector. Resonance self-shielding factors (L-factors) of unity were used for both  $U^{235}$  and  $U^{238}$ .

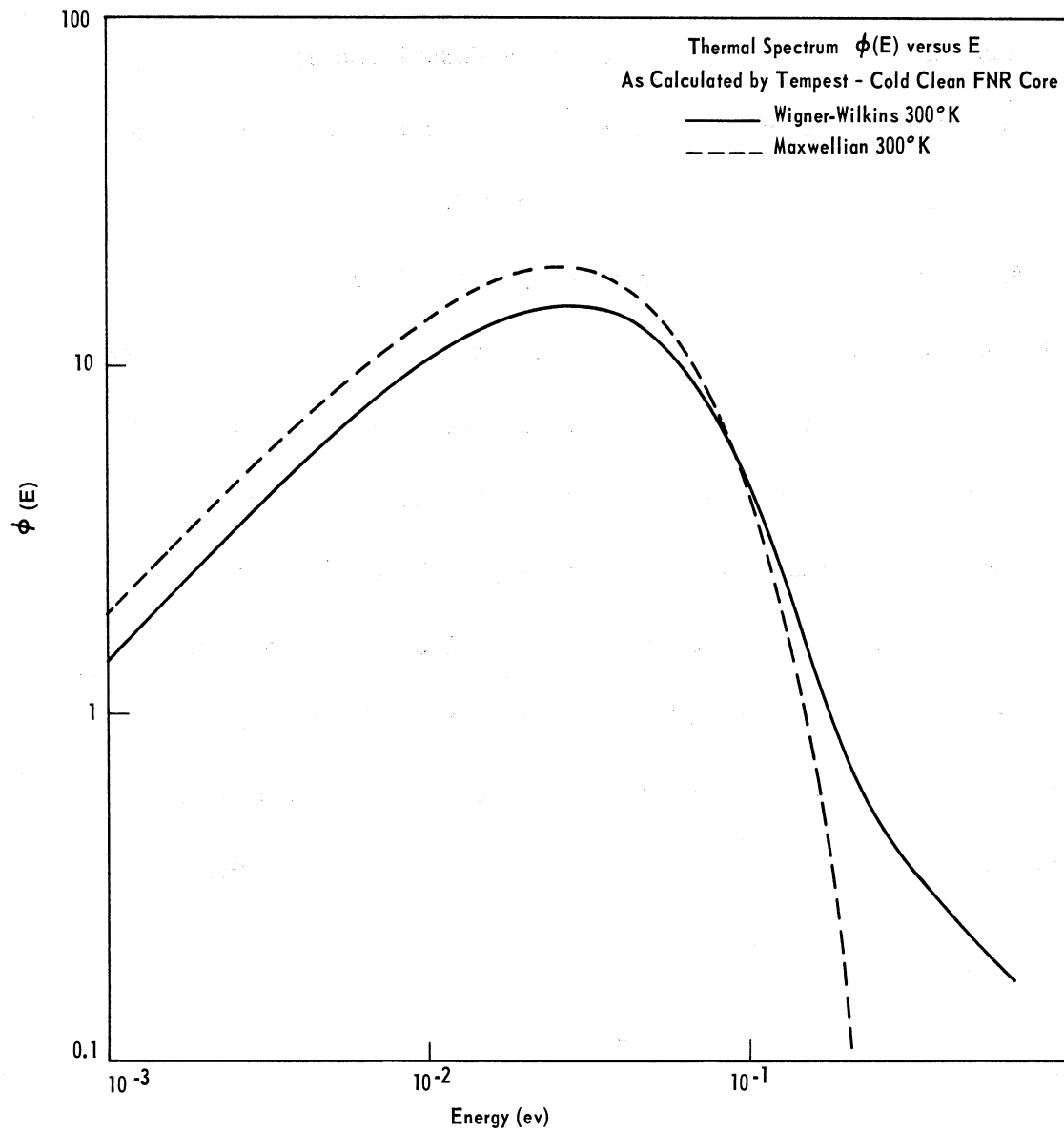


Figure C.1. Wigner-Wilkins and Maxwellian thermal spectra for cold-clean FNR core at 300°K.

TABLE C. I

## COMPOSITIONS

	Cold-Clean Core			Equil. Xe 8.4% BU Core			Homogenized Graph.			Reflector				
	Volume Fraction	Nuc. cm <sup>3</sup>	x 10 <sup>24</sup>	Volume Fraction	Nuc. cm <sup>3</sup>	x 10 <sup>24</sup>	Volume Fraction	Nuc. cm <sup>3</sup>	x 10 <sup>24</sup>	Graph.	H <sub>2</sub> O	D <sub>2</sub> O	BeO	Be
H <sub>2</sub> O	.5845	---	---	.5845	---	---	.0694	---	---	---	---	---	---	---
H	---	.0392	---	---	.0392	---	---	.00464	---	---	.0670	---	---	---
O	---	.0196	---	---	.0196	---	---	.00232	---	---	.0335	.0331	.0728	---
Al	.4133	.0249	---	.4133	.0249	---	.0774	.00466	---	---	---	---	---	---
U <sup>235</sup>	.00197	9.46 x 10 <sup>-5</sup>	---	.00181	8.67 x 10 <sup>-5</sup>	---	---	---	---	---	---	---	---	---
U <sup>238</sup>	2.26 x 10 <sup>-4</sup>	1.08 x 10 <sup>-5</sup>	---	2.26 x 10 <sup>-4</sup>	1.08 x 10 <sup>-5</sup>	---	---	---	---	---	---	---	---	---
B <sup>10</sup> *	---	---	---	.20 x 10 <sup>-5</sup>	.27 x 10 <sup>-6</sup>	---	---	---	---	---	---	---	---	---
Xe <sup>135</sup>	---	---	---	---	.85 x 10 <sup>-9</sup>	---	---	---	---	---	---	---	---	---
C	---	---	---	---	---	---	.854	.0685	.0803	---	---	---	---	---
D <sub>2</sub> O	---	---	---	---	---	---	---	---	---	---	.0331	---	---	---
D	---	---	---	---	---	---	---	---	---	---	.0662	---	---	---
Be	---	---	---	---	---	---	---	---	---	---	---	---	.0725	.1236

\*Equivalents to account for non-Xe<sup>135</sup> fission product poisoning.

TABLE C.II

THERMAL GROUP CONSTANTS

	Cold-Clean Core	Equil. Xe 8.4% BU Core	Reflector					
			Homogenized Graph.	Graph.	H <sub>2</sub> O	D <sub>2</sub> O*	Be	BeO
$\langle \Sigma_a \rangle$ > cm <sup>-1</sup>	.0629	.0622	.00256	.000263	.0195	.000029	.00108	.000651
$\langle D \rangle$ > cm	.2993	.2989	.693	.915	.1546	.831	.4155	.4354
$\langle \nu \Sigma_f \rangle$ > cm <sup>-1</sup>	.0996	.0915	0.0	0.0	0.0	0.0	0.0	0.0
$\langle \Sigma_{tr} \rangle$ > cm <sup>-1</sup>	1.377	1.378	.490	.364	2.485	---	.802	.7655
$\langle \Sigma_s \rangle$ > cm <sup>-1</sup>	1.313	1.313	---	.384	3.06	.375	.741	.720

\*Not available in TEMPEST library; obtained by averaging BNL-325 cross section data over a Maxwellian spectrum.

TABLE C.III  
FAST GROUP CONSTANTS

	Cold-Clean Core	Equil. Xe* BU Core	Reflector					
			Homogenized Graph.	Graph.	H <sub>2</sub> O	D <sub>2</sub> O	Be	BeO
$\langle \Sigma_a \rangle_1 \text{ cm}^{-1}$	.000898	.000885	.000056	.000003	.00138	.00144	.00453	.00449
$\langle \Sigma_a \rangle_2$	.000285	.000267	.000018	0.0	.000013	0.0	.000002	.000001
$\langle \Sigma_a \rangle_3$	.00485	.00454	.000124	0.0	.000954	0.0	.000054	.000031
$\langle \Sigma_a \rangle$	.00190	.00173	.000073	0.0	.000787	.000148	.000729	.000549
$\langle \Sigma_R \rangle_1 \text{ cm}^{-1}$	.07429	.07445	.0321	.0275	.1087	.0835	.0419	.0462
$\langle \Sigma_R \rangle_2$	.08509	.08336	.0199	.0113	.1494	.0372	.0275	.0230
$\langle \Sigma_R \rangle_3$	.08252	.0804	.0161	.00657	.1520	.0196	.0169	.0134
$\langle \Sigma_R \rangle$	.0254	.0236	.00734	.00372	.0495	.0115	.00885	.00746
$\langle \nu \Sigma_f \rangle_1 \text{ cm}^{-1}$	.000306	.000281	0.0	0.0	0.0	0.0	0.0	0.0
$\langle \nu \Sigma_f \rangle_2$	.000380	.000346	0.0	0.0	0.0	0.0	0.0	0.0
$\langle \nu \Sigma_f \rangle_3$	.00593	.00539	0.0	0.0	0.0	0.0	0.0	0.0
$\langle \nu \Sigma_f \rangle$	.00207	.00180	0.0	0.0	0.0	0.0	0.0	0.0
$\langle D \rangle_1 \text{ cm}$	2.017	1.920	2.369	2.410	2.048	2.175	1.908	1.442
$\langle D \rangle_2$	1.156	1.144	1.085	1.049	1.057	1.230	.581	.549
$\langle D \rangle_3$	.905	.907	.950	.934	.595	1.242	.486	.502
$\langle D \rangle$	1.365	1.341	1.245	1.122	1.245	1.334	.7364	.6287
$\langle \Sigma_s \rangle_1 \text{ cm}^{-1}$	.201	.201	---	.163	.261	.178	.209	.285
$\langle \Sigma_s \rangle_2$	.597	.597	---	.342	.761	.248	.636	.641
$\langle \Sigma_s \rangle_3$	.910	.910	---	.377	1.385	.240	.736	.695

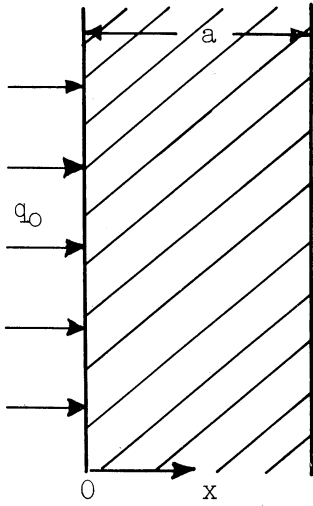
Subscripts: 1—.821 Mev to 10 Mev  
2—5.53 Kev to .821 Mev  
3—.621 ev to 5.53 Kev

Non-subscripted constant denotes .621 ev to 10 Mev.

\*Xe<sup>135</sup> cross sections were not available on the library tape, thus it was neglected here.

APPENDIX D

COMPARISON OF CURRENT BOUNDARY CONDITION AND PSEUDO  
BOUNDARY CONDITION AT VACUUM INTERFACE



We desire to compare solutions to the two-group diffusion equations utilizing (i) the realistic boundary condition on the partial current and (ii) the pseudo boundary condition on the scalar flux. We examine a system which is similar to the one studied in the text but deviates sufficiently to

allow an analytic solution. Consider a slab of width  $a$ , with fast neutrons entering the medium at  $x = 0$ . We write the two-group diffusion equations:

$$D_1 \frac{d^2 \phi_1}{dx^2} - \Sigma_{R1} \phi_1 = 0 \quad (D.1)$$

$$D_2 \frac{d^2 \phi_2}{dx^2} - \Sigma_{a2} \phi_2 + \Sigma_{R1} \phi_1 = 0 \quad (D.2)$$

The solution for the flux in group 1 is:

$$\phi_1(x) = Ae^{-\kappa_1 x} + Be^{\kappa_1 x}, \quad (D.3)$$

and for group 2:

$$\phi_2(x) = Ce^{-\kappa_2 x} + De^{\kappa_2 x} + S_1 \phi_1(x); \quad (D.4)$$



where:

$$\kappa_1^2 = \frac{\sum R_1}{D_1} , \quad (D.5)$$

$$\kappa_2^2 = \frac{\sum a_2}{D_2} , \quad (D.6)$$

and:

$$S_1 = \frac{\sum R_1}{D_2} \left( \frac{1}{\kappa_2^2 - \kappa_1^2} \right) . \quad (D.7)$$

Adopting the approach of Chapter II, we assume that the fast flux decays as it would in the infinite medium unperturbed by the void at a, allowing us to set  $B = 0$ . Then the thermal flux is given by:

$$\phi_2(x) = Ce^{-\kappa_2 x} + De^{\kappa_2 x} + S_1 A e^{-\kappa_1 x} , \quad (D.8)$$

where the constant  $A$  is determined by the source strength,  $q_0$ . Another constant is eliminated by a boundary condition on the thermal flux at  $x = 0$ . For the sake of argument assume that:

$$j_2^+(0) = \frac{\phi_2(0)}{4} - \frac{l_{tr2}}{6} \frac{d\phi_2}{dx} \Big|_0 = 0 , \quad (D.9)$$

which specifies the thermal flux within one arbitrary constant,  $C$ , giving:

$$\phi_2(x) = C \left\{ e^{-\kappa_2 x} - \frac{\left(1 + \frac{2}{3} l_{tr2} \kappa_2\right)}{\left(1 - \frac{2}{3} l_{tr2} \kappa_2\right)} e^{\kappa_2 x} \right\} + S_1 A \left\{ e^{-\kappa_1 x} - \frac{\left(1 + \frac{2}{3} l_{tr2} \kappa_1\right)}{\left(1 - \frac{2}{3} l_{tr2} \kappa_2\right)} e^{\kappa_2 x} \right\} . \quad (D.10)$$

Applying the realistic boundary condition at  $x = a$ :

$$j_2^-(a) = \frac{\phi(a)}{4} - \frac{l_{tr2}}{6} \left. \frac{d\phi}{dx} \right|_a = j_A^- , \quad (D.11)$$

the constant becomes:

$$C_i = \frac{4j_A^- S_{1A} \left\{ \left(1 - \frac{2}{3} l_{tr2} \kappa_1\right) e^{-\kappa_1 a} - \frac{\left(1 + \frac{2}{3} l_{tr2} \kappa_1\right)}{\left(1 - \frac{2}{3} l_{tr2} \kappa_2\right)} \left(1 + \frac{2}{3} l_{tr2} \kappa_2\right) e^{\kappa_2 a} \right\}}{\left(1 - \frac{2}{3} l_{tr2} \kappa_2\right) e^{-\kappa_2 a} - \frac{\left(1 + \frac{2}{3} l_{tr2} \kappa_2\right)}{\left(1 - \frac{2}{3} l_{tr2} \kappa_2\right)} \left(1 + \frac{2}{3} l_{tr2} \kappa_2\right) e^{\kappa_2 a}} . \quad (D.12)$$

Applying the pseudo boundary condition:

$$\phi(a+d) = 4j_A^- , \quad (D.13)$$

the constant becomes:

$$C_{ii} = \frac{4j_A^- S_{1A} \left\{ e^{-\kappa_1(a+d)} - \frac{\left(1 + \frac{2}{3} l_{tr2} \kappa_1\right)}{\left(1 - \frac{2}{3} l_{tr2} \kappa_2\right)} e^{\kappa_2(a+d)} \right\}}{e^{-\kappa_2(a+d)} - \frac{\left(1 + \frac{2}{3} l_{tr2} \kappa_2\right)}{\left(1 - \frac{2}{3} l_{tr2} \kappa_2\right)} e^{\kappa_2(a+d)}} . \quad (D.14)$$

Inasmuch as we have used the uncorrected diffusion theory extrapolation distance in the analysis:

$$e^{\pm \kappa(a+d)} = e^{\pm \kappa \left( a + \frac{2}{3} l_{tr} \right)} = e^{\pm \kappa a} e^{\pm \frac{2}{3} l_{tr} \kappa} . \quad (D.15)$$

Then for  $l_{tr} \kappa \ll 1$ :

$$e^{\pm \kappa(a+d)} \simeq e^{\pm \kappa a} \left( 1 \pm \frac{2}{3} l_{tr} \kappa \right) . \quad (D.16)$$

It follows that:\*

$$C_i \approx C_{ii} \quad . \quad (D.17)$$

---

\*For light water,  $2/3 l_{tr_2}^k = .095$  and  $2/3 l_{tr_2}^k = .052$ .

APPENDIX E

DUCT MOUTH CONTRIBUTION TO THE RADIAL CURRENT AT THE WALL

Consider the contribution to the partial current in the radial direction at  $(R, z_1)$  from the mouth of a cylindrical void. The number of neutrons per second passing through  $dS_1$  emanating from the mouth is given by:

$$j^+(R, z_1) dS_1 = \int_{S_A} dS_A \hat{z} \cdot \bar{\Omega} \bar{\phi}(r, 0, \bar{\Omega}) d\Omega \quad (E.1)$$

The angular flux at the mouth, neglecting source contributions, is expressed by:

$$\bar{\phi}(r, 0, \bar{\Omega}) \approx \frac{1}{4\pi} \left[ \phi_0(r, 0) - \bar{\Omega} \cdot \bar{\nabla} \phi_0 \Big|_0 \right] \quad (E.2)$$

Assuming polar symmetry:

$$\bar{\nabla} \phi_0 \Big|_0 = \hat{r} \frac{\partial \phi_0}{\partial r} \Big|_0 + \hat{z} \frac{\partial \phi_0}{\partial z} \Big|_0 \quad (E.3)$$

Referring to Figure E.1:

$$dS_A = r dr d\beta \quad , \quad (E.4)$$

$$dS_1 = 2R d\theta dz \quad , \quad (E.5)$$

and:

$$\bar{\Omega} = -\frac{h}{\psi} \hat{r} - \frac{p}{\psi} \hat{y} + \frac{z_1}{\psi} \hat{z} \quad (E.6)$$

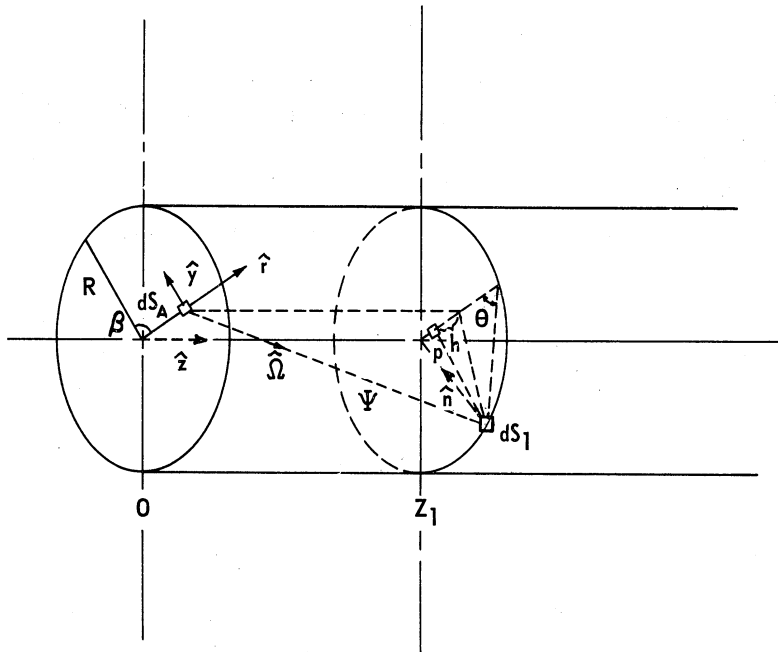


Figure E.1. Duct configuration for calculation of mouth contribution to wall radial current.

From geometrical considerations:

$$\hat{n} = \hat{r} \cos 2\theta + \hat{y} \sin 2\theta, \quad (\text{E.7})$$

$$p = R \sin 2\theta, \quad (\text{E.8})$$

and:

$$h = r + R \cos 2\theta. \quad (\text{E.9})$$

Accordingly:

$$d\Omega = \frac{dS_1}{\psi^2} (-\hat{n} \cdot \bar{\Omega}) = \frac{dS_1}{\psi^3} (R+r \cos 2\theta), \quad (\text{E.10})$$

and;

$$\psi^2 = z_1^2 + p^2 + h^2 = z_1^2 + R^2 + 2rR \cos 2\theta + r^2 \quad . \quad (\text{E.11})$$

Using Eqs. (E.3) and (E.6), the angular flux takes on the form:

$$\phi(r, 0, \bar{\Omega}) = \frac{1}{4\pi} \left\{ \phi_0(r, 0) - \ell \left[ \frac{z_1}{\psi} \frac{\partial \phi_0}{\partial z} \Big|_0 - \frac{h}{\psi} \frac{\partial \phi_0}{\partial r} \Big|_0 \right] \right\}, \quad (\text{E.12})$$

and the current is obtained by substituting the above expressions into Eq. (E.1):

$$\begin{aligned} j^+(R, z_1) &= \frac{1}{2\pi R dz} \int_0^\pi d\theta \int_0^{2\pi} d\beta \int_0^R r dr \frac{1}{4\pi} \left\{ \phi_0(r, 0) \right. \\ &\quad \left. - \ell \left[ \frac{z_1}{\psi} \frac{\partial \phi_0}{\partial z} \Big|_0 - \frac{h}{\psi} \frac{\partial \phi_0}{\partial r} \Big|_0 \right] \right\} \frac{z_1}{\psi} \left( \frac{2R dz}{\psi^3} \right) (R+r \cos 2\theta) \quad (\text{E.13}) \end{aligned}$$

Assume that  $\frac{\partial \phi_0}{\partial r} \Big|_0$  is negligible in comparison with  $\phi_0(r, 0)$  and  $\frac{\partial \phi_0}{\partial z} \Big|_0$ , which are taken to be constant over the entire mouth. Then Eq. (E.13) reduces to:

$$\begin{aligned} j^+(R, z_1) &= \frac{z_1}{\pi} \left\{ \phi_0(0) \int_0^R r dr \int_0^{\pi/2} d\theta \frac{(R+r \cos 2\theta)}{[z_1^2 + R^2 + r^2 + 2rR \cos 2\theta]^2} \right. \\ &\quad \left. - \ell z_1 \frac{\partial \phi_0}{\partial z} \Big|_0 \int_0^R r dr \int_0^{\pi/2} d\theta \frac{(R+r \cos 2\theta)}{[z_1^2 + R^2 + r^2 + 2rR \cos 2\theta]^{5/2}} \right\}. \quad (\text{E.14}) \end{aligned}$$

Or equivalently:

$$j^+(R, z_1) = \frac{z_1}{\pi} \left\{ \phi_0(0) \int_0^R r dr I_1(r, R, z_1) - \ell z_1 \frac{\partial \phi_0}{\partial z} \Big|_0 \int_0^R r dr I_2(r, R, z_1) \right\}. \quad (\text{E.15})$$

The integration to obtain  $I_1$  is easily performed, giving:

$$I_1(r, R, z_1) = \frac{\pi}{2} R \frac{(z_1^2 + R^2 - r^2)}{[(z_1^2 + R^2 + r^2)^2 - 4r^2 R^2]^{3/2}} \quad (E.16)$$

The second integration is considerably more difficult, but finally reduces to:

$$I_2(r, R, z_1) = \frac{q^3}{96(rR)^{5/2}(1-q^2)^2} \left\{ \left[ (R+r)q^4 - (R+3r)q^2 + 2r \right] K(q^2) - \left[ 2(R+r)q^4 - 2(2R+r)q^2 + 2r \right] E(q^2) \right\}, \quad (E.17)$$

where:

$$q^2 = \frac{4rR}{z_1^2 + (r+R)^2}, \quad (E.18)$$

and  $K$  and  $E$  are the complete elliptic integrals of the first and second kinds.<sup>15</sup>

The first integral with respect to  $r$ , giving the isotropic contribution to the current at  $(R, z_1)$ , can be done analytically, yielding:

$$\int_0^R r dr I_1(r, R, z_1) = \frac{\pi}{4z_1} \left\{ \frac{\frac{1}{2} + \frac{z_1^2}{4R^2}}{\left(1 + \frac{z_1^2}{4R^2}\right)^{1/2}} - \frac{z_1}{2R} \right\}. \quad (E.19)$$

The second integral, representing the contribution of the  $z$  component of the gradient to the current, must be done numerically. Combining terms, we write the final form for the contribution to the partial current at  $(R, z_1)$  from the mouth:

$$j^+(R, z_1) = \frac{1}{4} \phi_0(0) \left\{ \frac{\frac{1}{2} + \frac{z_1^2}{4R^2}}{\left(1 + \frac{z_1^2}{4R^2}\right)^{1/2}} - \frac{z_1}{2R} \right\} - l \frac{z_1^2}{\pi} \frac{\partial \phi_0}{\partial z} \Big|_0 \int_0^R r dr I_2(r, R, z_1). \quad (E.20)$$

## APPENDIX F

### NORMALIZATION FOR TIME VARYING FLUX

Consider the normalization of an experiment conducted in a time varying flux,  $\phi(t)$ . For purposes of discussion assume that the appropriate integrations over energy have been performed.

The time rate of change of the concentration of a species  $i$  is expressed as:

$$\frac{dC^i}{dt} = R^i(t) - \lambda C^i \quad , \quad (F.1)$$

where  $R(t)$  is the time dependent reaction rate:

$$R^i(t) = \sum^i \phi(t) \quad . \quad (F.2)$$

The activity at time  $t$ , the termination of an irradiation, is obtained by solving Eq. (F.1), and is given by:

$$A^i(t) = \lambda^i \int_0^t dt' R^i(t') e^{\lambda^i(t'-t)} = \lambda^i \sum^i \int_0^t dt' \phi(t') e^{\lambda^i(t'-t)} \quad . \quad (F.3)$$

We define the time averaged value of the flux:

$$\langle \phi \rangle = \frac{1}{t} \int_0^t \phi(t') dt' \quad . \quad (F.4)$$

Setting the time dependent flux equal to the product of a steady state flux magnitude and a function of time:

$$\phi(t) = \phi F(t) \quad , \quad (F.5)$$



Eq. (F.3) becomes:

$$A^i(t) = \lambda^i \sum^i \phi \int_0^t dt' f(t') e^{\lambda^i(t'-t)} . \quad (\text{F.6})$$

We desire to obtain the average value of the flux measured by a detector of species a normalized to the average flux measured at another position and at the same time by a detector of species b. Then:

$$\langle \phi \rangle_N^a \equiv \frac{\langle \phi \rangle^a}{\langle \phi \rangle^b} = \frac{\frac{1}{t} \phi^a \int_0^t f(t') dt'}{\frac{1}{t} \phi^b \int_0^t f(t') dt'} = \frac{\phi^a}{\phi^b} , \quad (\text{F.7})$$

and substituting from Eq. (F.6):

$$\langle \phi \rangle_N^a = \frac{A^a(t) \lambda^a \sum^a \int_0^t dt' f(t') e^{\lambda^a(t'-t)}}{A^b(t) \lambda^b \sum^b \int_0^t dt' f(t') e^{\lambda^b(t'-t)}} . \quad (\text{F.8})$$

Since we are interested only in relative normalized quantities:

$$\langle \phi \rangle_N^a \sim \frac{A^a(t)}{A^b(t)} e^{-(\lambda^a - \lambda^b)t} \frac{\int_0^t dt' f(t') e^{\lambda^a t'}}{\int_0^t dt' f(t') e^{\lambda^b t'}} . \quad (\text{F.9})$$

For the trivial case of a and b identical Eq. (F.9) reduces to:

$$\langle \phi \rangle_N^a \sim \frac{A^a(t)}{A^b(t)} . \quad (\text{F.10})$$

APPENDIX G

COMPUTER PROGRAM FOR EVALUATION OF  $\left. \frac{\partial \phi / \partial r}{\phi} \right|_R$

The Fortran program for the computation of  $\left. \frac{\partial \phi / \partial r}{\phi} \right|_R$  along the duct wall is listed here. The calculation assumes separation of variables in the current balance relationship and evaluates Eq. (2.50) (revised to include the terms in Expression (2.54) to account for the duct mouth contribution) at discrete points along the duct wall for an unperturbed axial flux distribution of a designated shape. Exponential, cosine, linear, and flat flux shapes are permissible. The input data are of the following form (Format I2, 8F8.4):

N(1) = 1	Linear flux shape
= 2	Flat flux shape
= 3	Cosine flux shape
= 4	Exponential flux shape

F(1)	} Parameters for flux shape
F(2)	
F(3)	
F(4)	

F(5) = $z_0$	Position of duct mouth (cm)
F(6) = R	Duct Radius
F(7) = $l$	Neutron mean free path in medium
F(8) = $\delta$	Interval of computation



```

29 IF(INDIC-3) 30,31,32
30 IF(INDIC-1) 33,33,34
31 PHIZ1=PHI3F(Z1)
DPHIZ1=DPHI3F(Z1)
GO TO 35
32 PHIZ1=PHI4F(Z1)
DPHIZ1=DPHI4F(Z1)
GO TO 35
33 PHIZ1=PHI1F(Z1)
DPHIZ1=A
GO TO 35
34 PHIZ1=1.0
J=2
35 X=PAINF(Z1)
CALL IEF1(1.5707,X,E,F,G)
IF(G-1.0) 102,102,100
100 WRITE OUTPUT TAPE 6,101,Z1
101 FORMAT(47H          ELLIPTIC INT. OUTSIDE OF RANGE ,Z1=F8.4)
E=1.0
F=10.0
102 TEG(1) = PHIZ1*((2.0*(1.0-X*X*X*X)+3.0*(2.0-X*X))*E-(1.0-X*X)
1*(8.0+X*X)*F)/(PHIZ2*X)
TEG(2) = PHIZ1*(2.0-(2.0+X*X)*SQRT(1.0-X*X))/PHIZ2
IF(INDIC-2) 36,37,36
36 TEG(3) = (DPHIZ1*(Z2-Z1)*((2.0+X*X)*F-2.0*(1.0+X*X)*E))/
1*(PHIZ2*SQRT((Z2-Z1)*(Z2-Z1)+4.0*R*R))
37 IF(Z1-Z0) 38,38,40
38 DO 39 I=1,3
TEG(I) = TEG(I)
SUM(I) = 0.50*TEG(I)
39 CONTINUE
GO TO 42
40 DO 41 I=1,3
SUM(I) = SUM(I) + TEG(I)
41 CONTINUE
42 DO 44 I=1,J
IF(ABSF(TEG(I))-ABSF(GET(I))) 43,26,26
43 IF (ABSF(TEG(I))-0.0005*ABSF(GET(I))) 44,26,26
44 CONTINUE
DENOM = 0.6667*(1.0+DECRE*SUM(1)/(6.2832*R))
F1 = (1.0-DECRE*SUM(2)/(4.0*R))/DENOM
F2 = DECRE*SUM(3)/(9.4248*R*DENOM)
C COMPUTE F3 AND F4
F3 = (PHIZ0/(2.0*R*PHIZ2*DENOM))*((Z2-Z0)*(Z2-Z0)+2.0*R*R)/
1SQRT(4.0*R*R+(Z2-Z0)*(Z2-Z0)-(Z2-Z0))
DEL = R/20.0
SUM = 0.0
Y=0.0
TEG=0.0
IF (INDIC-2) 47,45,47
47 Y=Y+DEL
Q=QUEERF(Y)
CALL IEF1(1.5707,Q,E,F,G)
IF (G-1.0) 105,105,103
103 WRITE OUTPUT TAPE 6,104,Y
104 FORMAT(48H          ELLIPTIC INT. OUTSIDE OF RANGE ,RAD=F8.4)
105 TEG = (Q*Q*Q/(96.0*SQRT(Y*Y*Y*Y*R*R*R*R*R*R)*(1.0-Q*Q)*(1.0-Q*Q)))
1*Y*((R+Y)*Q*Q*Q*Q-(R+3.0*Y)*Q*Q+2.0*Y)*F-(2.0*(R+Y)*Q*Q*Q*Q-2.0*
2(2.0*-+Y)*Q*Q+2.0*Y)*E)
IF ((R-Y)-0.0001) 45,45,46
46 SUM = SUM + TEG
GO TO 47
45 SUM = SUM+0.50*TEG
F4 = (4.0*(Z2-Z0)*(Z2-Z0)*DPHIZ0*DEL*SUM)/(3.1416*PHIZ2*DENOM)
C COMPUTE FINAL VALUE AND PRINT
BOUND = F1 + AMBDA*F2 - F3 + AMBDA*F4
GRAD = BOUND/AMBDA
WRITE OUTPUT TAPE 6,48,Z2,DENOM,F1,F2,F3,F4,BOUND,GRAD
48 FORMAT (8F9.4)
IF (INDIC-2) 50,49,50
49 IF ((Z2-Z0)-12.0) 51,52,52
50 IF (PHIZ2-0.25*PHIZ0) 52,51,51
51 Z2 = Z2 + DECRE
GO TO 8
52 GO TO 1
END
$DATA

```

## REFERENCES

1. Egelstaff, P. A. (editor), "Tailored Neutron Beams," Special Issue, J. Nucl. Energy, Parts A & B, 17, Nos. 4/5 (1963).
2. Carter, R. S. and Jablonski, F. E., "A Study of Split Cores for Research Reactors," Nucl. Sci. Eng., 5, 257 (1959).
3. Carter, R. S., Landon, H. H., and Muehlhause, C. O., "The National Bureau of Standards Reactor Facility," Trans. Am. Nucl. Soc., 5, No. 2, 423 (Nov. 1962).
4. Kouts, H., "Beam-Tube Design for the High-Flux Beam Reactor," see Ref. 1.
5. Behrens, D. J., "The Effect of Holes in a Reacting Material on the Range of Neutrons," Proc. Phys. Soc. (London), 62, Part 10, No. 358A, 607 (1949).
6. Reynolds, A. B., et al., "Reactivity Effects of Large Voids in the Reflector of a Light-Water-Moderated and Reflected Reactor," Nucl. Sci. Eng., 7, 1 (1960).
7. Baraff, G. A., Murray, R. L., and Menius, A. C., "Perturbation Integrals for Two-Group Calculations and Application to Reflector Ducts," Nucl. Sci. Eng., 4, 623 (1958).
8. Spinney, K. T., "Radiation Streaming Through Ducts-A Survey of the Present Situation," Trans. Am. Nucl. Soc., 5, No. 2, 390 (Nov. 1962).
9. Simon, A., and Clifford, C. E., "The Attenuation of Neutrons by Air Ducts in Shields," Nucl. Sci. Eng., 1, 156 (1956).
10. Piercey, D. C., "The Transmission of Thermal Neutrons Along Air Filled Ducts in Water," AEEW-R70 (1962).
11. Davison, B., "Neutron Transport Theory," Oxford at the Clarendon Press (1957).
12. Case, K. M., DeHoffman, F., and Placzek, G., "Introduction to the Theory of Neutron Diffusion," Vol. I, Los Alamos Scientific Laboratory (1953).

## REFERENCES (Continued)

13. Glasstone, S., and Edlund, M. C., "The Elements of Nuclear Reactor Theory," D. Van Nostrand Company, Inc. (1952).
14. Zimmerman, E. L., "Boundary Values for the Inner Radius of a Cylindrical Annular Reactor," ORNL-2484 (1958).
15. Jahnke, E. and Emde, F., "Tables of Functions," Dover Publications (1945).
16. "Research Reactors," Chapter 2, U. S. Atomic Energy Commission, McGraw-Hill Book Company, Inc. (1955).
17. Shapiro, J. L., et al., "Initial Calibration of the Ford Nuclear Reactor," MMPP-110-1 (1958).
18. Hughes, D. J., and Schwartz, R. B., "Neutron Cross Sections," BNL-325, Second Edition (1958).
19. Macklin, R. L., and Pomerance, H. S., "Resonance Capture Integrals," First Intern. Conf. Peaceful Uses of Atomic Energy, Geneva, 1955P/833.
20. Dayton, I. E., and Pettus, W. G., "Effective Cadmium Cutoff Energy," Nucleonics, 15, No. 12, 86 (1957).
21. Dalton, G. R., private communication (1963).
22. Reynolds, A. B., "Reactivity Effects of Large Voids in the Reflector of a Light-Water-Moderated and Reflected Reactor," thesis, AECU-4391 (1959).
23. Dalton, G. R., and Osborn, R. K., "Flux Perturbations by Thermal Neutron Detectors," Nucl. Sci. Eng., 9, 198 (1961).
24. Fastrup, B., "On Cadmium Ratio Measurements and Their Interpretation in Relation to Reactor Spectra," Risø Report No. 11 (1959).
25. Walton, R. B., et al., "Measurements of Neutron Spectra in Water, Polyethylene, and Zirconium Hydride," Proc. Symp. on Inelastic Scattering of Neutrons, IAEA (1960).
26. Schmid, L. C., and Stinson, W. P., "Calibration of Lutetium for Measurements of Effective Neutron Temperatures," Nucl. Sci. Eng. Letters, 7, 477 (1960).

## REFERENCES (Continued)

27. Klahr, C., "Limitations of Multigroup Calculations," Nucl. Sci. Eng., 1, 253 (1956).
28. Cantwell, M., and Goldsmith, M., "The Effect on Calculated Clean Critical Activation Shapes of the Use of Transport Approximations in the Fast Groups," Nucl. Sci. Eng., 12, 490 (1962).
29. Donovan, J. L., King, J. S., and Zweifel, P. F., "A Thermal Neutron Spectrum Measured by a Crystal Spectrometer," Univ. of Mich., ORA Report O3671-3-T, Ann Arbor, January, 1963.
30. Brown, H. D., "Neutron Energy Spectra in Water," DP-64 (1956).
31. Goldsmith, M., et al., "Theoretical Analysis of Highly Enriched Light Water Moderated Critical Assemblies," Second Intern. Conf. Peaceful Uses of Atomic Energy, Geneva, 1958 P/2376.
32. Daniels, E., forthcoming master's thesis, The University of Michigan (1963).
33. Feiner, F., et al., "Precise Criticality Determinations in the Solid Homogeneous Assembly," Trans. Am. Nucl. Soc., 5, No. 2, 344 (Nov. 1962).
34. Bullock, J. B., "Calculation of the Maximum Fuel Cladding Temperatures for Two Megawatt Operation of the Ford Nuclear Reactor," unpublished, Phoenix Memorial Laboratory Memo Report No. 1, The University of Michigan (1962).
35. "University of Michigan Executive System for the IBM-7090 Computer," unpublished, The University of Michigan (1963).
36. Flatt, H. P., "The Fog One-Dimensional Neutron Diffusion Equation Codes," unpublished, North American Aviation Corp. (1961).
37. Tobias, M. L., and Fowler, T. B., "The Twenty Grand Program for the Numerical Solution of Few-Group Neutron Diffusion Equations in Two Dimensions," ORNL-3200 (1962).
38. Shudde, R. H., "Tempest II," unpublished, North American Aviation Corp. (1960).
39. Amster, H., and Suarez, R., "The Calculation of Thermal Constants Averaged Over a Wigner-Wilkins Flux Spectrum; Description of the Sofocate Code," WAPD-TM-39 (1957).

## REFERENCES (Concluded)

40. McGoff, D. J., "Form, A Fourier Transform Fast Spectrum Code for the IBM-709," NAA-SR-Memo-5766 (1960).
41. Bohl, H., Gelbard, E. M., and Ryan, G. H., "Muft-4; Fast Neutron Spectrum Code for the IBM-704," WAPD-TM-72 (1957).



UNIVERSITY OF MICHIGAN



3 9015 02827 4705

**THE UNIVERSITY OF MICHIGAN**

**DATE DUE**

12/1	1pm
------	-----